공학박사 학위논문

리튬 이차전지용 층상구조 산화물계 양극 소재의 전이금속 이동과 전기화학 특성간 관계에 관한 연구

Effect of transition metal migration in layered oxide cathode materials for lithium secondary batteries

2019 년 2 월

서울대학교 대학원

재료공학부

구 교 진

Abstract

Effect of transition metal migration in layered oxide cathode materials for lithium secondary batteries

Kyojin Ku

Department of Materials Science and Engineering

College of Engineering

The Graduate School

Seoul National University

Highly advanced portable devices and development of electric vehicles enlarge the demand on the Li-ion battery (LIB) with improved energy density. Generally, since the specific capacity of cathode is lower than anode material in LIB, about twice more amount of cathode should be loaded in practical battery cells. Accordingly, the development of cathode material with high specific capacity is one of the main strategies in enhancing the energy density of LIB. The most commonly used cathode materials at the moment are layered materials, which have high energy density with 2-dimensional ionic path, such as $LiCoO_2$ and $LiNi_xCo_yMn_zO_2$ (NCM). However, to meet the recent surging needs for the LIB with higher energy densities, development on the cathode materials with higher

capacity are necessary.

Among the various factors that affect electrochemical properties of layered materials, structure of layered materials is known to be one of the most closely related factors. According to the classical understandings, the lithium de/intercalation has been believed to take place topotactically without altering the layered frame work. Although it was demonstrated that the presence of transition metal (TM) in the lithium layer reduces the lithium slab space, thus increases the repulsion between the migrating lithium and the TM in the transition metal layer, resulting in higher activation barriers for lithium diffusion, the defective TMs were regarded as stationary. In this rigid structure model, lithium is the sole mobile ion in the intercalation host, hence, the pristine structure of the materials was considered to be the most critical factor for electrochemical performances. However, recent works have confirmed that various structural evolutions such as TM migration and oxygen evolution occur during the electrochemical reactions. Therefore, it is important to understand the structural evolution occurring on electrochemical cycling and how such structural changes affect the electrochemical properties of the layered materials.

Here, I investigate the structural evolution of layered materials with various electrochemical conditions, from several cycles to the simple storage, and its effects on electrochemical properties. I unambiguously show that the layered-to-spinel-like structural transformation is strongly coupled with the activation of Mn redox couple in lithium-rich layered oxides, which leads to the voltage decay with

electrochemical cycling. Therefore, the voltage decay problem could be resolved by simple substitution with Ni redox buffer. In addition, I demonstrate that just one cycle of the lithium-rich layered oxides results in the asymmetric TM migration in the structure affecting the lithium mobility and propose a new lithium diffusion model correlated with TM migration. Furthermore, I show that structural evolution occurs even just storage at high temperature without any electrochemical cycle for high nickel NCM materials, leading to the unique memory effect behavior of the electrode material. These findings on the close relationships between structural evolution and electrochemical properties suggest that better understanding on the structural evolution upon various electrochemical conditions would provide the opportunity to further improve layered materials for LIB.

Keywords: Batteries, Cathodes, Layered oxides, Lithium-excess materials, Positive electrode, Lithium rechargeable batteries.

Student Number: 2013-20580

Contents

List of Tables

List of Figures

cycles at 1C rate.

Figure 2.10. **Transition from surface-controlled to bulk-diffusion-controlled reaction.** XPS Mn 2p spectra of a) LL226 and b) LL244. The black, red, and blue spectra (from top to bottom) represent the observed spectra of pristine LLNMO, the surface of cycled LLNMO, and an etched plane (surface + bulk properties) of LLNMO electrodes, respectively. The Mn 2p spectra of the etched planes show the reduction of Mn ions to the trivalent state after cycling. The activation of Mn dominantly occurred in LL226 rather than in LL244.

Figure 2.11. Ni K-edge XANES spectra of a) LL226, b) LL235, and c) LL244 electrodes at pristine (black), charged to 4.8 V (red), and discharged to 2.0 V (blue). Nickel divalent/tetravalent redox reactions occur in all compounds regardless of initial oxidation states of nickel ions.

Figure 2.12. **Structural variations in LLNMO after electrochemical cycling.** SAED pattern of LL226 a) before and b) after five cycles and that of LL244 c) before and d) after five cycles along the $[-441]_R$ direction, which is parallel to the $[10-1]_M$ direction of monoclinic C2/m and $[001]_C$ direction of cubic Fd-3m (spinel phase). HR-TEM images and the intensity histograms of the red boxed regions are presented in the insets of the SAED patterns. e) Raman spectra of LLNMOs after five cycles. The orange and green peaks are attributed the A1g mode of the spinel and layered phases, respectively, whereas the blue peaks are attributed both to the E_g mode of the layered phase and F_{2g} mode of the spinel phase.

Figure 2.13. Structural differences between the layered $(110)_R//(020)_M$ planes and spinel $(220)_C$ plane. The formation of spinel-like phases in LLNMO after cycling takes place by the interlayer migration of the transition metal ions between the transition metal slabs.

Figure 2.14. HR-TEM images and corresponding Fast Fourier transform (FFT) images of cycled LL226. Red circles in the FFT images denotes the {220} planes of the cubic spinel phase.

Figure 2.15. **Structural variations in LLNMO after electrochemical cycling.** a) XRD patterns of LL226 (black), LL235 (red), and LL244 (blue) after five electrochemical cycles. b) Peak ratio of (104)/(101) (black) and (104)/(003) (red) of LLNMOs before and after cycling. c) Simulated XRD patterns of LLNMO with no transition-metal ions in Li layers (black) and with 6% Ni (blue) or Mn (red) migration into Li layers.

Figure 2.16. **Structural variations in LLNMO after electrochemical cycling.** Raman spectra of LLNMOs before (black) and after five cycles (red) compared with spinel $Li_{1+x}Mn_2O_4$ (blue). Red dotted line and blue dotted line indicate A_{1g} mode of layered and spinel phases, respectively. The two peaks near 595 and 474 cm^{-1} correspond to the A_{1g} (symmetrical stretching of M–O) and E_g (symmetrical deformation) vibrational modes in layered lithium transition metal oxides with $R\bar{3}m$ symmetry, and the small peak at 425 cm^{-1} originates from the Li_2MnO_3-like structure with the lower C2/m symmetry. The intensity of the peak at 425 cm^{-1} increased with increasing Mn content in the samples, implying a higher degree of

ordering, which is consistent with the observation of the superstructure patterns in the XRD results (Figure 2.2a). The single A^{1g} mode for the pristine compounds indicates that the layered $LiMO_2$ and Li_2MnO_3 phases share a common layered lattice framework. The peak shift of A_{1g} mode of the pristine layered structure after cycling reflects the increase in the average mass of the atoms in the transition metal layers, which might be induced by the lattice densification. The densification is also consistent with the disappearance of the peak at 425 cm^{-1}, corresponding to the honeycomb-like ordering in the transition metal layers in our Raman study as well as the XRD results (Figure 2.15).

Figure 3.1. **Electrochemical profiles using various protocols.** (a) Electrochemical profiles of discharge and charge at 25 °C from various C-rates (1C, C/5, C/10, C/15, C/20) after respective pre-cycle at 60 °C. (b) Comparison of 60 °C (blue) and 25 °C discharge (orange) after 60 °C charge (dotted line). (c) Comparison of 60 °C (blue) and 25 °C (orange) charge after 60 °C 1 cycle (dotted line). (d) 25 °C discharge until 250 mAh g^{-1} and charge. (e) GITT on 25 °C discharge (orange). It is compared with 60 °C discharge profile (blue).

Figure 3.2. The first charge/discharge profile of LNM244 operated at 25 °C and 60 °C are compared. While 1.13 Li is extracted on 60 °C charge, only 0.79 Li is extracted on 25 °C charge. During the first

charge of LNM244, Ni is oxidized from 3+ to 4+ and oxygen oxidation accompanies with the rest of Li extraction. However, when I compare Ni XANES peak change during the first charge, Ni is fully oxidized in both temperatures (figure 3.3a,b), which indicates the difference in the first charge capacity originates from the different amount of oxygen oxidation. Therefore, LNM244 is pre-cycled at 60 °C and tested at 25 °C.

Figure 3.3. **Ni XANES spectra of LNM244.** (a) LNM244 cycled at 60 °C. (b) LNM244 cycled at 25 °C. Whereas Ni peak shifts at full charged states are almost identical, there is large difference in discharged state between two temperatures. When 2.0 V discharged states are compared, the cell operated at 60 °C is more reduced. (c) 60 °C charged and 25 °C 2.0 V discharged state (pink) is plotted together with the figure 3.3a. It is fitted well with 3.5 V 60 °C discharged state, which indicates that it is not fully discharged yet as shown in figure 3.1a. (d) 60 °C 1 cycled and 25 °C charged state (green) is plotted together with the figure 3.3a. It is fitted well with 60 °C full charged state, which indicates that charge reaction at 25 °C is not inhibited as shown in figure 3.1b.

Figure 3.4. Electrochemical profile of LNM244 one cycled at 60 °C, followed by 25 °C charge and discharge.

Figure 3.5. Electrochemical profile of LNM244 when it starts with discharge until 1.2 V from the pristine state.

Figure 3.6. 25 °C discharge to 2.0 V (red), followed by transferring to 60 °C oven, rested and discharged (blue). It is compared with normal

60 °C discharge profile (black).

Figure 3.7. GITT on 25 °C charge after 60 °C charge and 25 °C discharge with 250 mAh g^{-1} cutoff.

Figure 3.8. **Structural characterization of LNM244 discharged at different conditions.** STEM-HAADF image and the intensity line profile of boxed region immediately after (a) 60 °C charge, (b) 60 °C discharge, (c) 25 °C charge, (d) 25 °C discharge until 2 V and (e) 25 °C discharge until 250 mAh g^{-1}. Pink spheres denote TMs in C2/m unit cell of Li_2TMO_3. (f) XRD pattern of electrodes with 60 °C discharge (blue), 25 °C discharge to 2 V (green) and 25 °C discharge to 250 mAh g^{-1} (orange). Before discharging, all the electrodes were charged up to 4.8 V at 60 °C. (003) peaks around 18.5° are plotted together in the inset, which shows the hump at the 2 V discharged sample. (g) Raman spectra of pristine (black), 60 °C charge (brown), 60 °C discharge (blue), 25 °C discharge to 2 V (green) and 25 °C discharge to 250 mAh g^{-1} (orange). Before discharging, all the electrodes were charged up to 4.8 V at 60 °C.

Figure 3.9. **Temperature dependent electrochemical profile of LNM244.** (a) After 60 °C charge, the cell is discharged and charged at different temperatures from 10 °C to 60 °C. The cell is discharged by capacity cut until 250 mAh g^{-1} and charged by capacity cut until 250 mAh g^{-1} and voltage cut until 5.0 V. (b) Discharge capacity appearing at low voltage plateau calculated from Figure 3.9a. (c) Charge capacity delivered until 4.8 V from Figure 3.9a.

Figure 3.10. **Schematic illustration of local environment on TM migration.**

After full discharge (memory release), the cell is set to SOC 50% and stored in high temperature again for one month. The same memory effect behavior reappears after second one month storage (b), demonstrating that the thermal driven memory effect is repeatable phenomenon. c, After high temperature storage at SOC 50%, the cell is cycled until SOC 50% for 10 cycles (green), and then, full discharged at the rest of cycles. While the voltage drop does not appear during the initial 10 cycles discharging until SOC 50%, it appears during the full discharge cycle. d, e, After high temperature storage at SOC 50%, the cell is cycled by increasing discharge capacity from 100 mAh g^{-1} to 180 mAh g^{-1} by 20 mAh g^{-1}. The voltage drop appears only after discharging more capacity than previous discharge capacity.

Figure 4.4. Increasing polarization at the voltage dropped region. a, GITT (charge and discharge) data after high temperature storage at SOC 50%. b, GITT (discharge – charge – discharge) data starting from the discharge reaction, indicating that the polarization appears only during the first discharge reaction. c,d, EIS data after high temperature storage. Additional impedance arises from the SOC 50% region.

Figure 4.5. **Capacity retention recovery process for the high temperature stored cell.** a, Electrochemical profiles before recovery (blue), recover (green) and after recovery (orange) cycle. b, Enlarged profile of a. c, Capacity retention of recovery (orange) and undamaged (blue) cell. d, Capacity retention of recovery cell

(orange) normalized by capacity retention of undamaged cell (blue). e, Normalized capacity retention of repeated (every 3 cycles) recovery cell.

Figure 4.6. a, STEM-HAADF image before storage at SOC 50%. b, Enlarged image of a. Inset shows the intensity line profile of the box in b. c, FFT image of a.

Figure 4.7. **Structural evolution and local environment variation after high temperature storage.** a, STEM-HAADF image of stored cell at SOC 50% along [100] direction. b, Enlarged image of A region in a and its intensity line profile. c, Enlarged image of B region in a and its intensity line profile. d, Enlarged image of orange box region in a, demonstrating the formation of stacking faulted domain. e,f, Ptychography image before storage (e) and after storage (f) obtained from Ni L_3 absorption edge. The red and blue colors denote relatively oxidized and reduced oxidation state of Ni. g, Line profile of nickel oxidation state along AB line from e and f. h, ^{7}Li NMR spectra of the NCM811 samples at SOC 50% before storage (blue) and after storage (orange).

Figure 4.8. STEM-HAADF image after high temperature storage. Inset shows FFT image with clear streaks. Red region denotes stacking faulted region.

Figure 4.9. a, STEM-HAADF image of stored cell for EELS observation. b-d, Comparison of the Ni L3-edge EELS spectra between stacking faulted region (orange) and non-faulted region (blue) obtained from a.

Chapter 1. Introduction

1.1. Motivation and outlines

With growing concerns on the environmental problems, the development on the renewable energy and environmental friendly applications becomes a critical issue. Accordingly, energy storage system (ESS) and electric vehicles (EV) are considered as some of crucial technologies to solve the problems. Since lithium ion battery (LIB) is regarded as a key part of ESS or EV, which has high energy and power densities, the required electrochemical performances of LIB are also rapidly increasing.[1, 2] To satisfy these requirements, the developments on the cathode electrode materials with higher energy densities are necessary.

Among various cathode materials, layered materials have been most widely used conventionally due to their high energy density and two-dimensional lithium ionic path.[3, 4] The layered structures with $LiTMO_2$ (TM denotes transition metal) formula are composed of lithium layer located between TMO_2 slabs along c-axis. It has been understood that the structure of layered framework and electrochemical properties are closely related. From the classical point of view, layered structures were thought to be as a rigid structure, which is not affected by lithium de/intercalation. Therefore, the strategies for synthesizing layered materials with better electrochemical performances are focused to minimize TMs in lithium layer at the pristine state, which reduces the lithium slab space and repulses with migrating lithium, leading to the decrease in the lithium diffusion.[5-7] However,

recent studies have revealed that structure evolution such as TM migration and oxygen evolution occurs during cycles in layered materials.[8-10] Therefore, it is important to understand what kind of structural evolution can appear and how such evolutions influence the electrochemical properties of layered materials. In this study, I excavate structural evolutions that occur during various electrochemical protocols and reveal the effect of structural evolution onto the electrochemical performances of layered materials.

Chapter 2 demonstrates that the voltage decay with electrochemical cycling of the electrode is correlated to Mn^{4+}/Mn^{3+} redox activation and subsequent cation disordering, which can be remarkably suppressed *via* simple compositional tuning to induce the formation of Ni^{3+} in the pristine material. By implementing this new strategy, the Mn^{4+}/Mn^{3+} reduction is subdued by an alternative redox reaction involving the use of this pristine Ni^{3+} as a redox buffer, which has been designed to be widened from Ni^{3+}/Ni^{4+} to Ni^{2+}/Ni^{4+}, without compensation for the capacity in principle. Negligible change in the voltage profile of the modified lithium-rich nickel manganese oxide electrode is observed upon extended cycling, and manganese migration into the lithium layer is significantly suppressed. Based on these findings, I propose a general strategy to suppress the voltage decay of Mn-containing lithium-rich oxides to achieve long-lasting high energy density from this class of materials.

Chapter 3 shows that the unique TM migrations accompanied during a single charge/discharge significantly alter the lithium diffusion mechanism/kinetics

for lithium-rich layered oxide cathodes. I present clear evidences that the lithium diffusion is much more sluggish during the discharge (lithiation) than the charge (de-lithiation), which contrasts to the traditional lithium diffusion model based on the simple topotactic lithium intercalation/deintercalation in the layered framework. It is demonstrated that it is due to the reversible but asymmetric TM migration in the structure affecting the lithium mobility, which originates from the non-equivalent local environments around TM during respective charge and discharge process. This finding on the correlative behavior between TM migration and lithium mobility proposes a new lithium diffusion model in the layered structure and suggest the importance of considering TM migration in designing new lithium-rich layered oxide cathode materials.

Chapter 4 shows the unusual behavior of thermal driven memory effect on high Ni $LiNi_xCo_yMn_zO_2$ (NCM) material, attributed to the structural evolution after high temperature storage. I find out that when high Ni NCM cell is stored in 60 °C for several weeks at certain SOC, the cell memorizes the SOC and the voltage drop is generated as much as the charged capacity during the storage. It is demonstrated that the voltage drop is attributed to the delithiated domain formation by the agglomeration of delithiated region to reduce the strain, produced during the delithiation, and the lithiation into the delithiated domain results in the additional polarization. Based on our findings, I propose the model for thermal driven memory effect and suggest the necessity for considering the possibility that a memory effect could be generated at certain conditions in LIBs.

1.2. References

[1] J. M. Tarascon, M. Armand, *Nature* **2001**, 414, 359.

[2] M. S. Whittingham, *Chem. Rev.* **2004**, 104, 4271.

[3] J. Hong, H. Gwon, S.-K. Jung, K. Ku, K. Kang, *J. Electrochem. Soc.* **2015**, 162, A2447.

[4] L. Wen, O. Pilgun, L. Xien, L. Min-Joon, C. Woongrae, C. Sujong, K. Youngsik, C. Jaephil, *Angew. Chem. Int. Ed.* **2015**, 54, 4440.

[5] K. Kang, Y. S. Meng, J. Bréger, C. P. Grey, G. Ceder, *Science* **2006**, 311, 977.

[6] K. Kang, G. Ceder, *Phys. Rev. B* **2006**, 74, 094105.

[7] C. Delmas, J. P. Pérès, A. Rougier, A. Demourgues, F. Weill, A. Chadwick, M. Broussely, F. Perton, P. Biensan, P. Willmann, *J. Power Sources* **1997**, 68, 120.

[8] W. E. Gent, K. Lim, Y. Liang, Q. Li, T. Barnes, S.-J. Ahn, K. H. Stone, M. McIntire, J. Hong, J. H. Song, Y. Li, A. Mehta, S. Ermon, T. Tyliszczak, D. Kilcoyne, D. Vine, J.-H. Park, S.-K. Doo, M. F. Toney, W. Yang, D. Prendergast, W. C. Chueh, *Nat. Commun.* **2017**, 8, 2091.

[9] M. Sathiya, A. M. Abakumov, D. Foix, G. Rousse, K. Ramesha, M. Saubanère, M. L. Doublet, H. Vezin, C. P. Laisa, A. S. Prakash, D. Gonbeau, G. VanTendeloo, J. M. Tarascon, *Nat. Mater.* **2015**, 14, 230.

[10] C. R. Fell, D. Qian, K. J. Carroll, M. Chi, J. L. Jones, Y. S. Meng, *Chem. Mater.* **2013**, 25, 1621.

Chapter 2. Suppression of voltage decay through manganese deactivation and nickel redox buffering in high-energy layered lithium-rich electrodes

(The essence of this chapter has been published in Advanced Energy Materials. Reprinted with permission from [Kyojin Ku *et al*., *Adv. Energy Mater*. **2018,** 8, 1800606 DOI: 10.1002/aenm.201800606] Copyright (2018) WILEY-VCH, Verlag GmbH & Co. KGaA.)

2.1. Research background

One of the grand challenges facing green energy technologies such as electric vehicles and large-scale power backups is the need to achieve a breakthrough enhancement of the energy density in current lithium-ion batteries.[1] As a key step forward, great efforts have been made to develop electrode materials with higher reversible capacities. Among the various cathode materials investigated to date, layered lithium-rich nickel manganese oxides ($Li[Li_xNi_yMn_{(1-x-y)}]O_2$, $0 < x < 0.33$, $0 < y < 0.5$; hereafter called LLNMOs) are of particular interest because of their extraordinarily high reversible capacities (> 250 mAh g^{-1}) and relatively high operating voltage (~3.6 V vs. Li/Li^+).[2] Nevertheless, one of the critical issues encountered with the use of LLNMOs is the inevitable voltage decay, or the progressive decrease of the operating voltage with electrochemical cycling, which

leads to a gradual loss of the energy density. This voltage decay was proposed to originate from a structural transformation involving a spinel-like disordered phase via cation migration during cycling and the activation of the Mn^{4+}/Mn^{3+} redox reaction in the lower-potential region, which reduces the overall voltage.[3, 4] This claim was supported by Bo *et al*.[5], who identified lithium ions in tetrahedral sites and the migration of transition metal ions in a high-resolution electron microscopy study, suggesting the formation of a spinel-like domain. Yabuuchi *et al*.[6] also observed a bulk structural rearrangement, which included cation migration from the transition metal layer to the lithium layer, in lithium-rich layered 3d metal oxides in an X-ray diffraction (XRD) study. Recently, Gent *et al*.[7] used XRD and various spectroscopies to show that the cation migration in lithium-rich manganese-based metal oxides is coupled with the anion redox.

Sathiya *et al*.[8, 9] further elucidated the issue of cation migration in lithium-rich layered oxides using the simpler $Li_2Ru_{1-x}M_xO_3$ (M=Mn, Ti, Sn) system; these authors demonstrated that the voltage decay can be suppressed by substitution with Sn^{4+} ions, which inhibit the cation migration because of their large size. As the authors hypothesized that the ion size was a critical factor in the cation migration, they speculated that it would be difficult to mitigate the voltage fade for LLNMOs or 3d metal oxides because of the intrinsically small ionic size of 3d metal cations and their relatively high stability in tetrahedral sites.[10, 11] In this regard, more focus has recently shifted to the discovery of new lithium-rich materials based on 4d and 5d metals beyond 3d-metal-based oxides and LLNMOs,

with the identification of a few important lithium-rich electrode materials.[7, 11-17] Although these fundamental scientific studies on this series of new materials provide essential steps toward the development of high-energy-density cathodes capable of exploiting both the cation and anion redox reactions[18], these materials are still far from being considered for practical application because of the use of rare and heavy metals. In addition, the high raw material cost and relatively low energy density significantly dilute the potential merits of this class of lithium-rich layered materials.

In this respect, I highlight the importance of a careful revisit of the suppression of the voltage decay of practically viable lithium-rich materials composed of nickel and manganese. I note that the oxygen anion redox has never been reported to be a completely reversible process; there is always a partial permanent loss of oxygen from the material during the charge process via the oxygen gas evolution.[19-21] The partial loss of the oxygen redox capability requires an additional redox couple to compensate for the capacity, which typically induces the reduction of Mn^{4+} to Mn^{3+} during the following discharge of the LLNMO electrode. For example, in the representative LLNMO, $Li_{1.2}Ni^{2+}_{0.2}Mn^{4+}_{0.6}O_2$ (or $Li_2Mn^{4+}O_3$–$LiNi^{2+}_{0.5}Mn^{4+}_{0.5}O_2$), the initial oxidation state of manganese is +4, which is maintained even during charging, accompanying the oxidation of oxygen over 4.5 V vs. Li/Li^+; however, during the discharge, Mn^{4+} needs to be partially reduced to Mn^{3+} in the re-lithiation process because of the partial loss of the anionic redox activity, as schematically illustrated in Figure 2.1a and c.

Unfortunately, Mn^{3+} is known to be vulnerable to migration, which results in the layered-to-spinel phase transformation.[22, 23] The relatively small crystal field stabilization energy difference in octahedral and tetrahedral coordinations and the disproportionation into Mn^{2+} and Mn^{4+} generally facilitate the migration of Mn^{3+} into the lithium layer.

Herein, I demonstrate that the introduction of Ni^{3+} as a redox buffer through a simple substitution of Mn with Ni in $Li_{1.2}Ni^{2+}_{0.2}Mn^{4+}_{0.6}O_2$ (or $Li_2Mn^{4+}O_3$–$LiNi^{2+}_{0.5}Mn^{4+}_{0.5}O_2$) effectively suppresses the Mn reduction and voltage decay of this LLNMO without the use of 4d transition metals or doping with third heavy elements. To inhibit the reduction of Mn^{4+} to Mn^{3+} during the re-lithiation after the partial loss of the oxygen redox couple, I activate the Ni^{3+}/Ni^{2+} reduction process alternatively in the modified LLNMO electrode. It is demonstrated that the substitution of nickel increases the nickel oxidation state in the pristine compounds from 2+ ($Li_{1.2}Ni^{2+}_{0.2}Mn^{4+}_{0.6}O_2$) to 3+ ($Li_{1.2}Ni^{3+}_{0.4}Mn^{4+}_{0.4}O_2$ or $Li_2Mn^{4+}O_3$–$LiNi^{3+}O_2$) and that the electrochemical reduction of the increased quantity of Ni^{3+} replaces the Mn^{4+} reduction during the discharge process because of its higher redox potential in layered materials. Moreover, it is revealed that after the activation of the nickel redox buffer, it undergoes a full Ni^{2+}/Ni^{4+} redox reaction to compensate for the partial loss of the oxygen redox in the subsequent cycles. Although various LLNMO compositions have been previously explored in extensive studies[24, 25], I believe that this strategy of activating the widened nickel redox reaction and mitigating the unfavorable manganese redox will provide clearer guidance in the

design and compositional tailoring of LLNMO electrodes with practically high energy densities.

2.2. Experimental Methods

2.2.1. Sample preparation

$0.5Li_2MnO_3$–$0.5LiNi_xMn_{1-x}O_2$ (x = 0.5, 0.75, 1), *i.e.*, $Li_{1.2}Ni_yMn_{0.8-y}O_2$ (y = 0.2, 0.3, 0.4), were prepared using a solid-state reaction from lithium carbonate and nickel manganese carbonate ($Ni_yMn_{1-y}CO_3$, y = 0.25, 0.375, 0.5). The mixed nickel manganese carbonate was prepared via a co-precipitation method. A 0.2 M mixed nickel sulfate and manganese sulfate aqueous solution (Ni:Mn = 2:6, 3:5, 4:4) was added dropwise to an equal volume of a 1 M $NaHCO_3$ aqueous solution under constant stirring (250 rpm) at 50 °C. The pH was maintained at pH 9 by adding an appropriate amount of NH_4OH. The $(NiMn)CO_3$ precipitate was filtered, rinsed with deionized water several times, and dried overnight at 120 °C. The obtained powder was mixed with lithium carbonate; 3 wt% excess lithium carbonate compared with the stoichiometric amount was added to compensate for the possible lithium evaporation at high temperature. The mixture was heated at 900 °C for 6 h in air and then quenched by soaking the powder in liquid nitrogen.

2.2.2. Characterization of compound

The chemical formulas of the synthesized compounds were determined using ICP-AES (Thermo Jarrel Ash, Polyscan 60E, USA). The crystal structures of the layered Li-excess nickel manganese oxides were characterized using a D/MAX-2500 X-ray diffractometer (Rigaku, Japan) equipped with Cu-Kα radiation (λ = 1.54178 Å) in the 2θ range of 10–75°. ND data were collected over

the 2θ range of 15–155° with a step size of 0.05°, and λ = 1.8348 Å was supplied by a Ge (331) single-crystal monochromator on a high-resolution powder diffractometer (HRPD) at the HANARO facility at the Korea Atomic Energy Research Institute. The amount of residual lithium was measured by titration method (888 Titrando, Metrohm).

2.2.3. Electrochemical measurements

The electrodes were fabricated by casting a slurry paste consisting of 80 wt% active materials, 10 wt% carbon black (Super P), and 10 wt % polyvinylidene fluoride onto aluminum foil, which was used as the current collector. Coin-type cells (CR2016, Hohsen, Japan) were assembled using the electrodes, a Li metal counter electrode, a separating membrane (Celgard 2400), and a 1 M solution of $LiPF_6$ in a mixture of ethyl carbonate and dimethyl carbonate (EC/DMC, 1:1 v/v) as the electrolyte in an Ar-filled glove box. The galvanostatic charging/discharging process was performed at 60 °C at 20 mA g^{-1} in the voltage range of 2.0−4.8 V using a potentio-galvanostat (WonA Tech, WBCS 3000, Korea).

2.2.4. Ex situ characterization

For the ex situ experiments, the electrodes were retrieved by disassembling the tested cells and rinsing with DMC. The procedures were performed in an Ar-filled glove box. XPS spectra were obtained using an X-ray photoelectron spectrometer (Sigma Probe, Thermo VG Scientific, England) with an

Al-Kα (1487 eV) X-ray source. Ni and Mn K-edge XAS spectra were collected at the BL10C beamline at the Pohang Light Source (PLS) at the Pohang Accelerator Laboratory, Korea. A Si(1 1 1) double crystal was employed to monochromatize the X-ray photon energy. The monochromator was detuned to 35–45% of its original intensity to eliminate the high-order harmonics. Mn and Ni K-edge spectra were collected in transmission mode. Energy calibration was performed using the first inflection point of the spectra of Mn and Ni metal foils as a reference (i.e., Mn K-edge = 6539 eV and Ni K-edge = 8333 eV). Reference spectra were simultaneously collected for each in situ spectrum using Mn or Ni metal foils. The electrode samples were prepared by disassembling the coin cells after the electrochemical cycling and sealing them in a water-resistant polymer film in the Ar-filled glove box. Analysis of the XAS spectra was performed using the IFEFFIT software package.[26]

2.3. Results and Discussions

2.3.1. Redox mechanisms of LLNMOs

The proposed redox mechanisms of LLNMOs with two representatively different compositions and the potential role of Ni^{3+} as a redox buffer are schematically illustrated in Figure 2.1. Notably, even with the substitution and increased oxidation state of nickel, the initial charging capacity contributed by the nickel cationic redox reaction remains the same, with the redox mechanism relying on 0.4 of the Ni^{3+}/Ni^{4+} single redox (0.4 e^-) in $Li_{1.2}Ni^{3+}_{0.4}Mn^{4+}_{0.4}O_2$ (Figure 2.1b) or 0.2 of the Ni^{2+}/Ni^{4+} double redox (0.4 e^-) in $Li_{1.2}Ni^{2+}_{0.2}Mn^{4+}_{0.6}O_2$ (Figure 2.1a). After the partial loss associated with the anionic redox reaction, Mn^{4+} must be reduced to Mn^{3+} during the full re-lithiation in $Li_{1.2}Ni^{2+}_{0.2}Mn^{4+}_{0.6}O_2$ (Figure 2.1c). However, Ni^{3+} reduces to Ni^{2+} in $Li_{1.2}Ni^{3+}_{0.4}Mn^{4+}_{0.4}O_2$ because of the empty Ni^{2+}/Ni^{3+} state in the density of states (DOS) below the Mn^{3+}/Mn^{4+} state during the re-lithiation process, and therefore, the Ni^{2+}/Ni^{3+} state potentially plays the role of a redox buffer, as illustrated in Figure 2.1d. The subsequent cycles of the $Li_{1.2}Ni^{3+}_{0.4}Mn^{4+}_{0.4}O_2$ electrodes would then be available, utilizing both the Ni^{2+}/Ni^{3+} and Ni^{3+}/Ni^{4+} redox reactions instead of the single-electron Ni^{3+}/Ni^{4+} reaction in the pristine electrode. The additional activation of the nickel redox reaction fully compensates for the capacity loss from the subdued manganese redox reaction, which is also beneficial because of the higher redox potential of Ni^{2+}/Ni^{3+} than Mn^{3+}/Mn^{4+}.

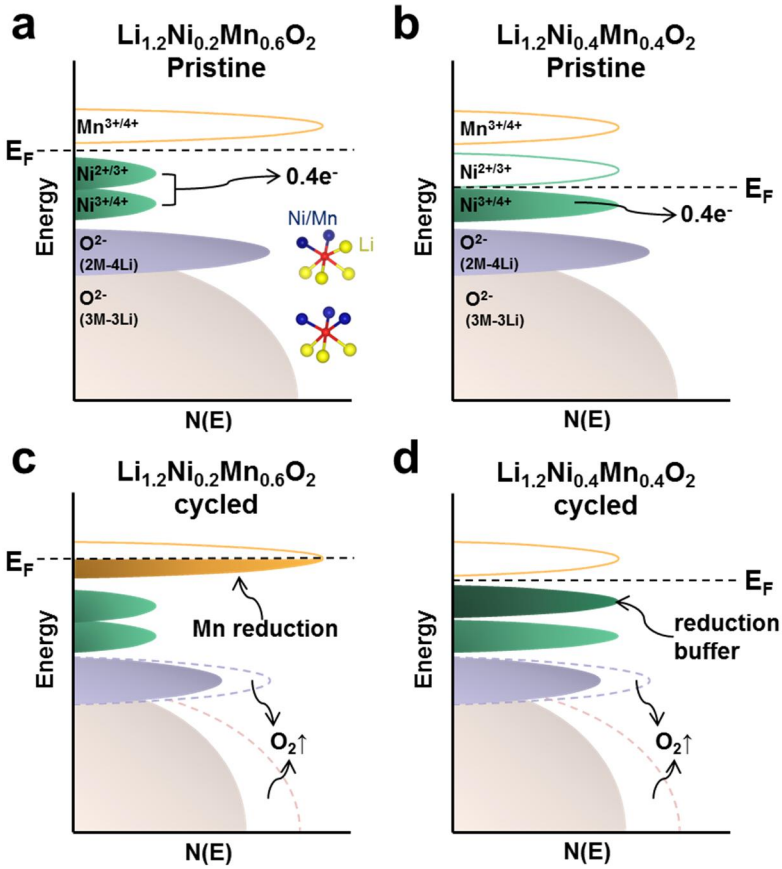

Figure 2.1. Schematic illustration of electronic structures in LLNMOs. Electronic density of states (DOS) of a) pristine $Li_{1.2}Ni_{0.2}Mn_{0.6}O_2$ (LL226), b) pristine $Li_{1.2}Ni_{0.4}Mn_{0.4}O_2$ (LL244), c) cycled LL226, and d) cycled LL244. The $Ni^{2+/3+}$ states in LL244 act as a reduction buffer, whereas manganese reduction occurs in the cycled LL226.

2.3.2. Synthesis and electrochemical properties of LLNMOs

I performed proof-of-concept experiments using a series of LLNMO compounds (zLi_2MnO_3–$(1-z)LiMO_2$) with a fixed amount of Li_2MnO_3 (z = 0.5) and systematic adjustment of the nickel to manganese ratio in $LiMO_2$ (M = $Ni_{0.5}Mn_{0.5}$, $Ni_{0.75}Mn_{0.25}$, and Ni). The chemical compositions of the target compounds were thus $Li_{1.2}Ni_yMn_{0.8-y}O_2$ (y = 0.2, 0.3, and 0.4; hereafter called LL226, LL235, and LL244, respectively). Relative ratio between lithium, nickel and manganese of the synthesized compounds were determined to be 1.20: 0.22: 0.67 (LL226), 1.20: 0.32: 0.56 (LL235) and 1.20: 0.43: 0.44 (LL244), respectively, using inductively coupled plasma-atomic emission spectroscopy (ICP-AES), in consistent with the target compositions. For the clarity, the amount of residual lithium impurities was quantified by titration technique, where it was found they were all comparable with the value obtained from the stoichiometric $LiNi_{0.6}Co_{0.2}Mn_{0.2}O_2$ which has been known to have little issue with residual lithium.[27] Both X-ray diffraction (XRD) and neutron diffraction (ND) patterns of the three compounds confirmed that they were O3-type layered structures; the diffraction patterns were indexed to the $R\bar{3}m$ symmetry with the superstructure patterns of the C2/m symmetry without impurities (Figure 2.2a and 2.2b).[2] The superstructure patterns in the 2θ range of 20–25° for the XRD analysis originated from the honeycomb-like transition-metal–lithium ordering (e.g. $LiMn_6$) in the transition metal layers.[28, 29] The weaker superstructure pattern in LL244 compared with that in LL226 suggests the more random atomic configuration in the transition

metal layers of LL244 with less manganese content, which has a strong tendency to form LiMn6 domains.[30, 31] The ND patterns of the LLNMO compounds varied more appreciably with the compositional changes than the XRD patterns because of the larger difference in the neutron scattering lengths of nickel (10.3 fm) and manganese (−3.73 fm),[32] as shown in Figure 2.2b. The intensities of the (003) peak at 22.4° and (104) peak at 53.6° gradually increased with increasing nickel content. This observation is consistent with the ND simulation results presented in Figure 2.3 and is attributed to the stronger scattering of neutrons by nickel than manganese. The lattice parameters and atomic occupancies of the LLNMO compounds were determined using Rietveld refinement of the XRD and ND patterns, and the results are summarized in Tables 2.1–2.5 and Figure 2.4 and 2.5. Systematic changes in the lattice parameters following Vegard's law were observed[33], which are indicative of the gradual changes in the Ni/Mn ratio within the lithium-rich layered framework. The X-ray absorption near-edge structure (XANES) of the Ni K-edge revealed that with increasing nickel content, the nickel ions of the pristine materials displayed higher oxidation states (Figure 2.6 and Figure 2.7d). This finding agrees with the targeted oxidation states of +2, +2.67, and +3 for LL226, LL235, and LL244, respectively. In contrast, as observed in the Mn K-edge spectra, the oxidation states of manganese remained unchanged at +4 for all of the compounds regardless of the Ni/Mn ratio (Figure 2.6 and Figure 2.7a).

I comparatively measured the electrochemical activities of the series of LLNMO electrodes to monitor the intrinsic behaviors of the voltage fade as a

function of cycling. To accelerate the potential structural evolution and voltage decay, I employed relatively harsh cycling conditions: a low current density of 20 mA g^{-1} at 60 °C in the voltage range of 2.0–4.8 V (Figure 2.2c–i and 2.8). During the initial charging process, all the LL226, LL235, and LL244 electrodes exhibited the characteristic plateau of lithium-rich layered oxide electrodes at 4.4–4.5 V, indicating that the oxidation of oxygen commonly occurred, as shown in Figure 2.8.[19, 34, 35] The initial charging capacities were 357, 352, and 343 mAh g^{-1}, respectively, corresponding to almost all the lithium being extracted from the materials (> ~1.1 Li^+ per formula unit). However, unlike the similar first charge profiles, the discharge profiles already began to show suppressed voltages, particularly for LL226. The distinct voltage decay behaviors for the samples are apparent in Figure 2.2c, which compares the charge/discharge profiles of the electrodes after five cycles. The voltage decay progressed most significantly in the LL226 electrode, with the appearance of a pseudo plateau at 2.2 V in the charge profile, consistent with previous reports[24, 36]. This finding suggests that the Mn^{4+}/Mn^{3+} redox reaction was active, which was most likely accompanied by a significant structural transformation followed by partial oxygen loss. In contrast, the voltage profiles of the electrodes with higher Ni^{3+} contents were stably maintained. LL244 exhibited the highest discharge voltage with an average value of 3.57 V, comparable to the initial discharge voltage, and LL235 exhibited an average discharge voltage of 3.54 V without the presence of the 3.2-V activity typically observed in manganese-containing lithium-rich layered oxide electrodes.

For more quantitative analysis of the voltage fade with cycling, the electrochemical profiles of each electrode for 40 cycles are presented in Figure 2.2d, f, and h along with the differential capacity vs. voltage plots in Figure 2.2e, g, and i. Figure 2.2d, f, and h clearly show that the voltage decay was substantially reduced for LL244 and LL235 in sharp contrast to clear voltage fade of LL226 with cycling. Even though the voltage profiles of LL244 appear to be similar to those of LL235 in terms of the voltage decay, the differential capacity plots (Figure 2.2g and 2.2i) clearly reveal that LL244 was more effective for suppression, as indicated by the dotted line, which shows the least shift to lower voltage. It is also possible to find same trend at the 80 cycle test at 1C rate, where LL244 shows much less voltage decay than LL226 (Figure 2.2c inset and 2.9). This finding confirms that the voltage decay was significantly subdued with increasing Ni^{3+} content; the role of Ni^{3+} will be discussed in more detail in the following sections. I note that these trends were also observed in previous reports on the electrochemical properties of various lithium-rich nickel manganese oxides, although their origin remained elusive.[24, 25, 37]

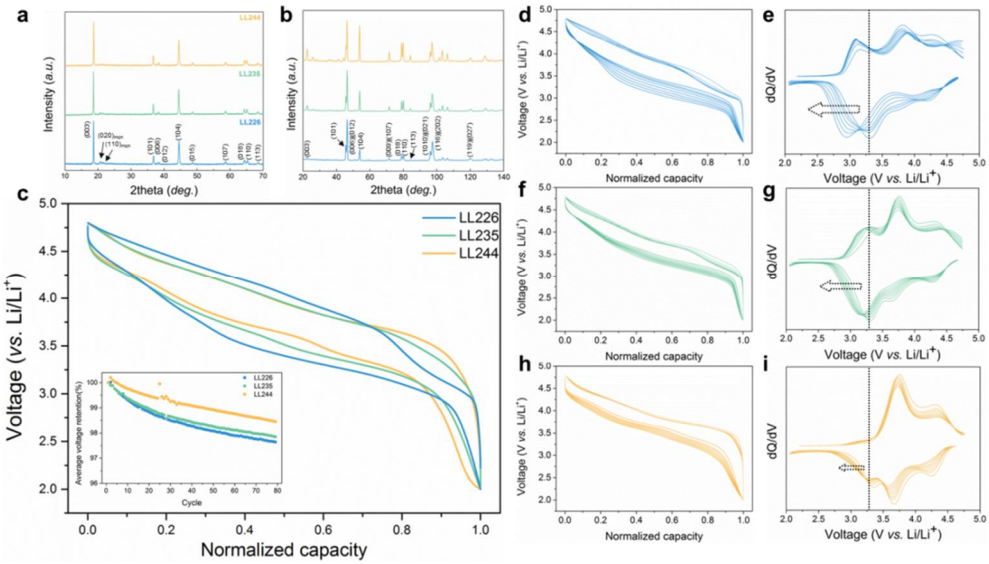

Figure 2.2. Structures and electrochemical curves of LLNMOs. a) XRD and b) ND patterns of pristine LL226 (blue), LL235 (green), and LL244 (orange). c) Fifth normalized charge/discharge profile of LLNMOs. Inset shows average voltage retention (%) of LLNMOs over cycles at 1C rate. The normalized charge/discharge profile from the 5th to 40th cycles and their dQ/dV plots of d), e) LL226, f), g) LL235 and h), i) LL244. The results are plotted every 5 cycles. The dotted lines in e), g) and i) represent the initial discharge redox potentials of the LLNMOs.

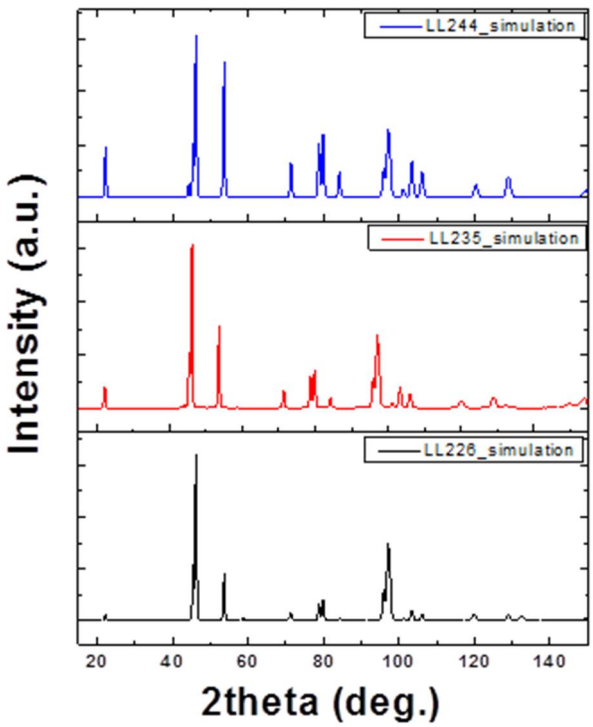

Figure 2.3. Simulated neutron diffraction patterns of 226, LL235, LL244.

Table 2.1. The detailed data for the structural refinement of LLNMO using XRD patterns

Source	X-ray		
Formula	$Li_{1.2}Ni_{0.2}Mn_{0.6}O_2$	$Li_{1.2}Ni_{0.3}Mn_{0.5}O_2$	$Li_{1.2}Ni_{0.4}Mn_{0.4}O_2$
Crystal system	Rhombohedral	Rhombohedral	Rhombohedral
Space group	$R\bar{3}m$	$R\bar{3}m$	$R\bar{3}m$
Lattice parameters			
a (Å)	2.8586 (2)	2.8616 (2)	2.8662 (2)
c (Å)	14.2611 (24)	14.2519 (17)	14.2477 (15)
Unitcell volume ($Å^3$)	100.922 (22)	101.067 (18)	101.365 (16)
Formula weight	85.03	85.41	85.78
Temperature (K)	300	300	300
Wave length (Å)	1.54059	1.54059	1.54059
2θ range	10 - 80°	10 - 80°	10 - 80°
Number of data points	7000	7000	7000
Step size	0.01°	0.01°	0.01°
R_p (%)	2.55	2.38	2.60
R_I (%)	8.65	6.50	4.90
R_F (%)	7.61	6.55	4.35
χ^2	1.77	1.36	1.93

Table 2.2. The detailed data for the structural refinement of LLNMO using ND patterns

Source	Neutron		
Formula	$Li_{1.2}Ni_{0.2}Mn_{0.6}O_2$	$Li_{1.2}Ni_{0.3}Mn_{0.5}O_2$	$Li_{1.2}Ni_{0.4}Mn_{0.4}O_2$
Crystal system	Rhombohedral	Rhombohedral	Rhombohedral
Space group	$R\bar{3}m$	$R\bar{3}m$	$R\bar{3}m$
Lattice parameters			
a (Å)	2.8575 (2)	2.8600 (1)	2.8656 (1)
c (Å)	14.2499 (8)	14.2430 (5)	14.2427 (4)
Unitcell volume ($Å^3$)	100.767 (10)	100.892 (5)	101.285 (5)
Formula weight	85.03	85.41	85.78
Temperature (K)	300	300	300
Wave length (Å)	1.834333	1.834333	1.834333
2θ range	0 - 160°	0 - 160°	0 - 160°
Number of data points	3200	3200	3200
Step size	0.05	0.05	0.05
R_p (%)	4.08	3.55	3.23
R_I (%)	4.66	3.28	2.96
R_F (%)	3.84	2.57	2.25
χ^2	7.24	6.71	5.24

Table 2.3. The atomic positions and occupancies in LL226 using ND patterns

Atom	x	y	z	B_{iso}	Occupancy
Li1	0	0	0.5	1.35 (9)	0.96 (1)
Ni1	0	0	0.5	1.35 (9)	0.03 (1)
Li2	0	0	0	0.40 (1)	0.21 (1)
Ni2	0	0	0	0.40 (1)	0.16 (1)
Mn2	0	0	0	0.40 (1)	0.61
O1	0	0	0.2585 (1)	1.48 (3)	1.0

Table 2.4. The atomic positions and occupancies in LL235 using ND patterns

Atom	x	y	z	B_{iso}	Occupancy
Li1	0	0	0.5	1.08 (9)	0.97 (1)
Ni1	0	0	0.5	1.08 (9)	0.03 (1)
Li2	0	0	0	0.70 (3)	0.22 (1)
Ni2	0	0	0	0.70 (3)	0.27 (1)
Mn2	0	0	0	0.70 (3)	0.50
O1	0	0	0.2586 (1)	0.92 (2)	1.0

Table 2.5. The atomic positions and occupancies in LL244 using ND patterns

Atom	x	y	Z	B_{iso}	Occupancy
Li1	0	0	0.5	1.3 (1)	0.96 (1)
Ni1	0	0	0.5	1.3 (1)	0.02 (1)
Li2	0	0	0	0.36 (7)	0.21 (1)
Ni2	0	0	0	0.36 (7)	0.38 (1)
Mn2	0	0	0	0.36 (7)	0.4
O1	0	0	0.2583 (1)	0.49 (2)	1.0

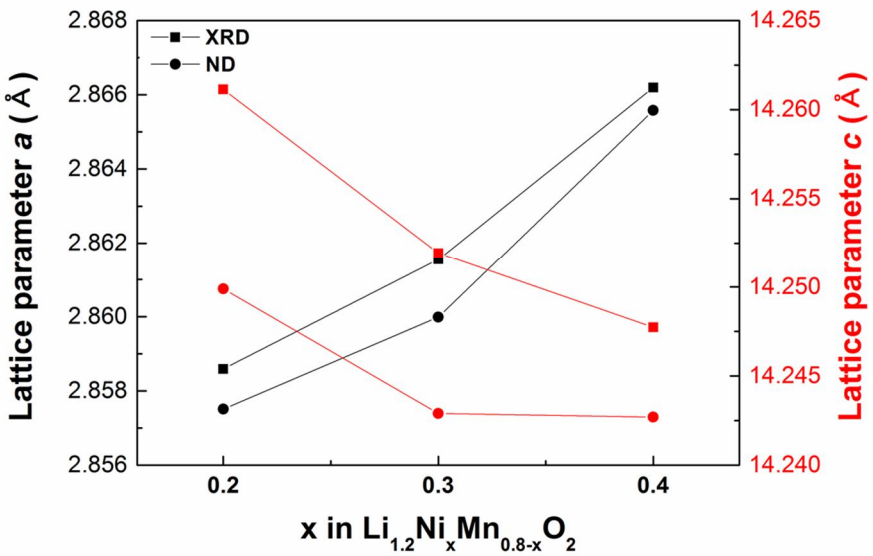

Figure 2.4. Lattice parameters of LL226, LL235, and LL244 observed by XRD and ND analyses. When only ionic size is considered, lattice parameters a and c should be larger in LL226. However, lattice parameter a is larger in LL244, while lattice parameter c is larger in LL226 as expected. Anisotropic changes of a and c lattice parameters are attributed to the Jahn-Teller distortion of Ni^{3+} ion. The Jahn-Teller effect distorts the octahedral Ni of LiNiO2 and splits Ni-O bonds into four 1.91 Å bonds and two 2.09 Å bonds,[38] which makes the lattice expand in a and b axes and contract in c axis.

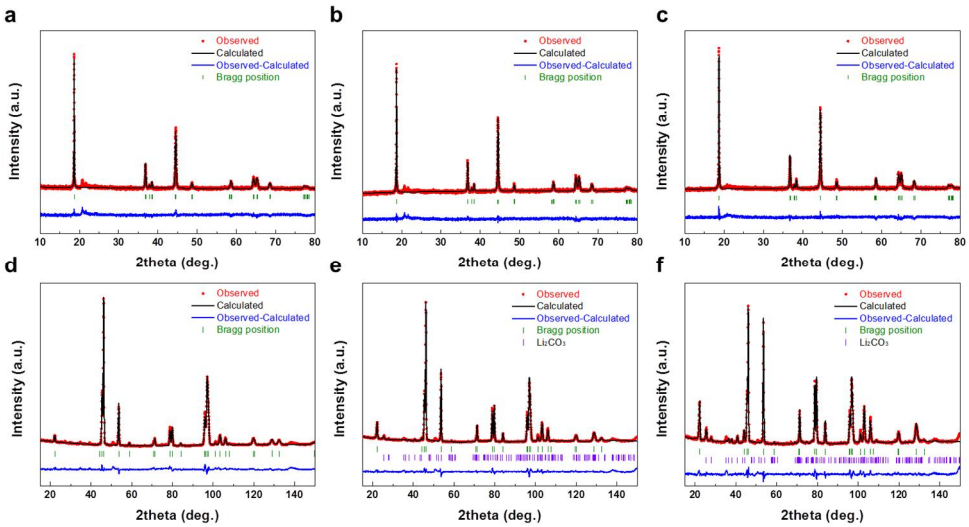

Figure 2.5. Rietveld refinements of the a, b, c) XRD patterns and d, e, f) ND patterns of LL226, LL235, and LL244 (left to right). R-factors for XRD and ND patterns are represented in Table 2.1 and 2.2.

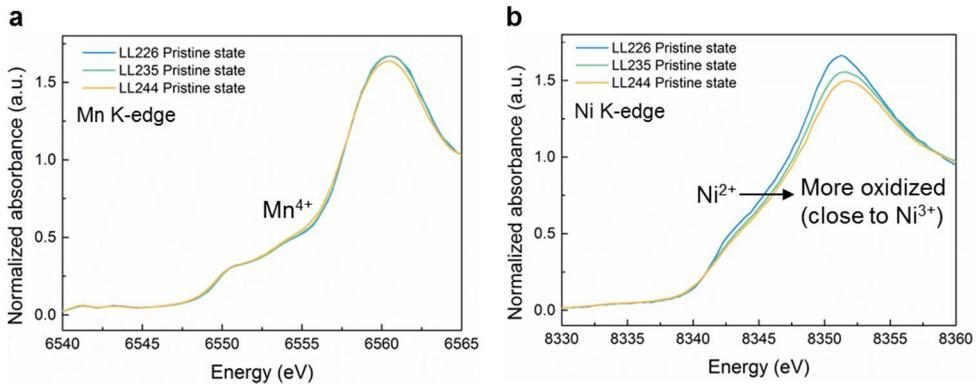

Figure 2.6. a) XANES Mn K-edge spectra, and b) XANES Ni K-edge spectra of pristine LL226 (blue), LL235 (green), and LL244 (orange). Mn and Ni K-edge spectra were collected in transmission mode with employing a Si(1 1 1) double crystal to monochromatize the X-ray photon energy. The monochromator was detuned to 35–45% of its original intensity to eliminate the high-order harmonics. Energy calibration was performed using the first inflection point of the spectra of Mn and Ni metal foils as a reference (i.e., Mn K-edge = 6539 eV and Ni K-edge = 8333 eV). Reference spectra were simultaneously collected for each in situ spectrum using Mn or Ni metal foils.

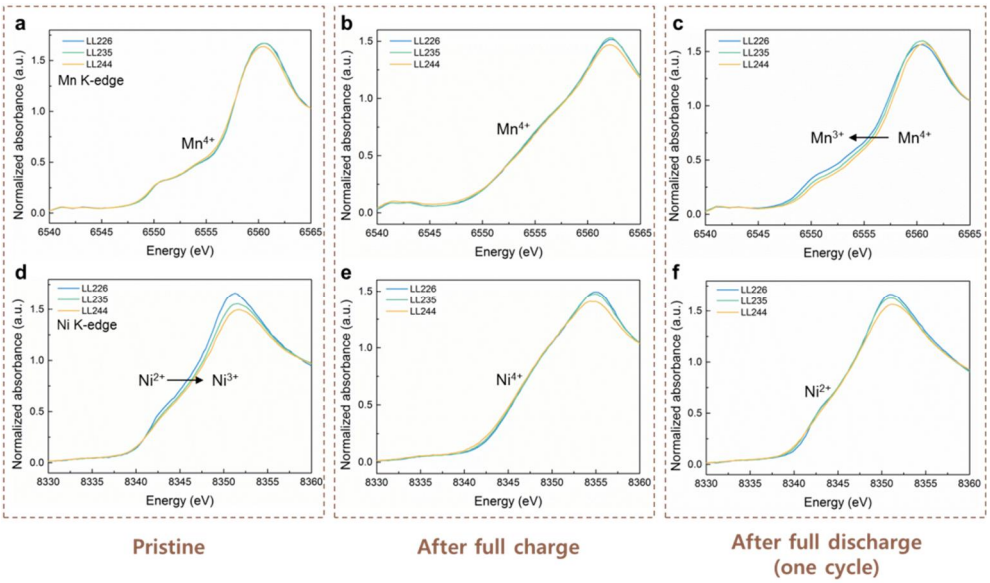

Figure 2.7. Oxidation state changes of nickel and manganese during the first cycle. Mn K-edge XANES spectra of LL226 (blue), LL235 (green), and LL244 (orange) in a) pristine state, b) charged state (4.8 V), and c) discharged state (2.0 V). Ni K-edge XANES spectra of LL226, LL235, and LL244 in d) pristine state e) charged state, and f) discharged state.

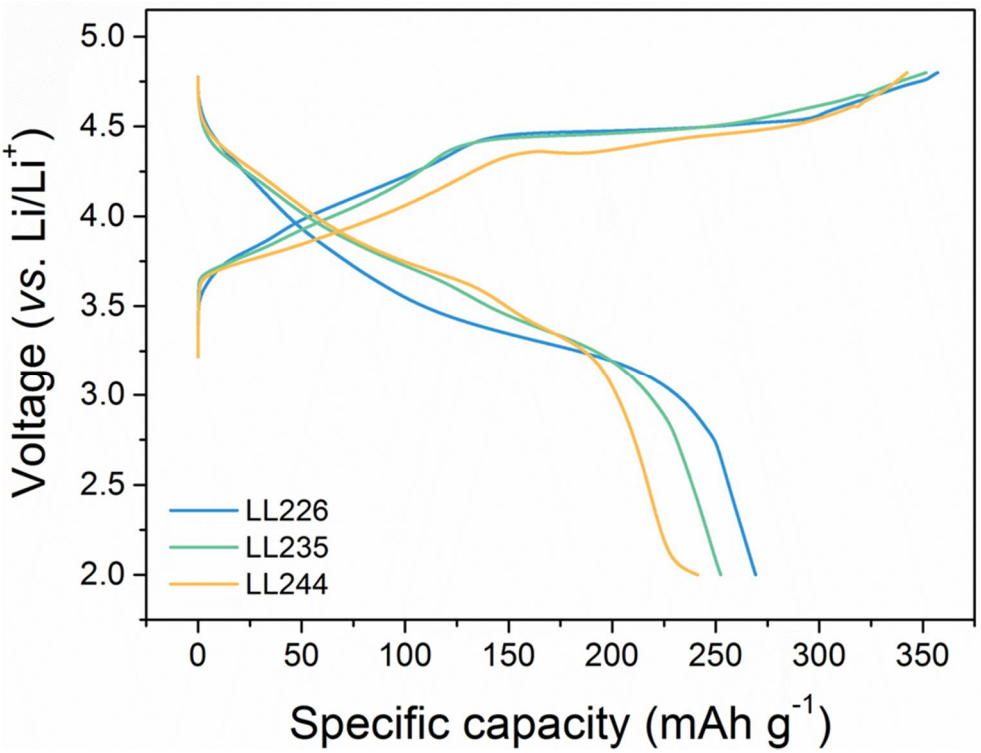

Figure 2.8. First charge/ discharge profile of LLNMOs. Blue, green, orange denote LL226, LL235 and LL244 respectively.

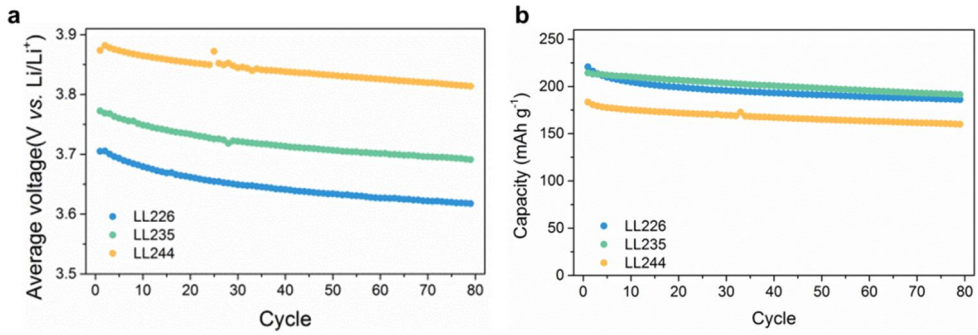

Figure 2.9. a) Average voltage and b) capacity retention of LLNMOs during 80 cycles at 1C rate.

2.3.3. Role of nickel as a redox buffer

To clarify the redox mechanisms and understand the distinctive behaviors of the LLNMO electrodes, ex situ X-ray absorption spectroscopy (XAS) was performed for each sample during cycling. Figure 2.7a–f present the XANES spectra of the Mn K-edge and Ni K-edge for the three electrodes in pristine, charged, and discharged states. The Mn K-edge spectra in Figure 2.7a indicate that the oxidation states of Mn were identical as +4 for the pristine LL226, LL235, and LL244 electrodes and remained unchanged during the charging process, as illustrated in Figure 2.7b. These findings support the claim that the manganese redox reaction does not occur during the first charge process. However, the discharge process apparently induced different manganese redox activity for the samples, as shown in Figure 2.7c. The reduction of Mn^{4+} to Mn^{3+} was clearly observed for LL226, which is consistent with previous findings.[6, 36, 39] However, the Mn^{4+} reduction was substantially suppressed in LL235 and LL244, and the most effective suppression was observed for LL244, which nearly maintained the initial Mn^{4+} state. These findings were further confirmed by X-ray photoelectron spectroscopy (XPS) experiments, which supported the claim that more extensive manganese reduction occurred in LL226 than in LL244 after electrochemical cycling (Figure 2.10).

The spectra at the Ni K-edge in Figure 2.7e–f further highlight the different redox behaviors of the three samples. Figure 3d shows that the nickel oxidation states were initially +2, +2.67, and +3 for the pristine LL226, LL235, and

LL244 electrodes, respectively, in accordance with expectations based on their nominal compositions. Upon charging to 4.8 V, all of the Ni K-edge spectra shifted to the same edge energy corresponding to the Ni^{4+} state (Figure 2.7e), confirming the double redox reaction of Ni^{2+}/Ni^{4+} in the LL226 electrode and the single redox of Ni^{3+}/Ni^{4+} in the LL244 electrode. During discharge, the spectra shifted back to lower energy, indicative of the reduction of Ni4+ ions; however, all the samples were identically reduced to the Ni^{2+} state at the end of discharge (Figure 2.7f), in clear contrast with the initially different nickel oxidation states. This finding strongly suggests that the redox reaction of nickel ions in LL244 (or LL235) was extended from Ni^{3+}/Ni^{4+} (or $Ni^{2.67+}/Ni^{4+}$) to Ni^{2+}/Ni^{4+} after the first cycle (more clear comparisons are presented in Figure 2.11). The widened electrochemical redox activity of nickel coincides with the suppressed manganese redox reaction in LL244 (or LL235), supporting the claim that a subdued Mn^{3+}/Mn^{4+} reaction in LLNMO electrodes can be achieved by tailoring the nickel redox activity, which serves as a redox buffer after the partial loss of the oxygen anionic redox. The universal observation of the activation of redox couples originally inactive in LLNMOs, which necessitates loss of the reversible oxygen redox couple, indicates the minimal change in the stability of the oxygen anion redox with the substitution of nickel while further work is required for better understanding. The activation of the additional Ni^{2+}/Ni^{3+} redox reaction in LL244 and LL235 after the first cycle also accounts for the high electrochemical activities at 3.7 V of the samples without loss of the capacity in the absence of manganese redox activity. It is noteworthy

that the redox reaction of Ni^{3+}/Ni^{2+} instead of Mn^{4+}/Mn^{3+} could occur during the discharge because of its higher redox potential, as illustrated in Figure 2.1.

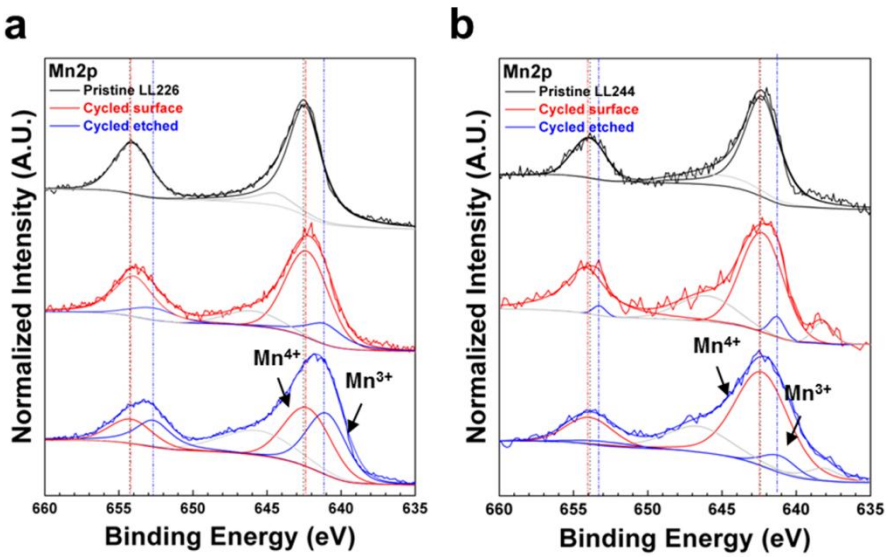

Figure 2.10. Transition from surface-controlled to bulk-diffusion-controlled reaction. XPS Mn 2p spectra of a) LL226 and b) LL244. The black, red, and blue spectra (from top to bottom) represent the observed spectra of pristine LLNMO, the surface of cycled LLNMO, and an etched plane (surface + bulk properties) of LLNMO electrodes, respectively. The Mn 2p spectra of the etched planes show the reduction of Mn ions to the trivalent state after cycling. The activation of Mn dominantly occurred in LL226 rather than in LL244.

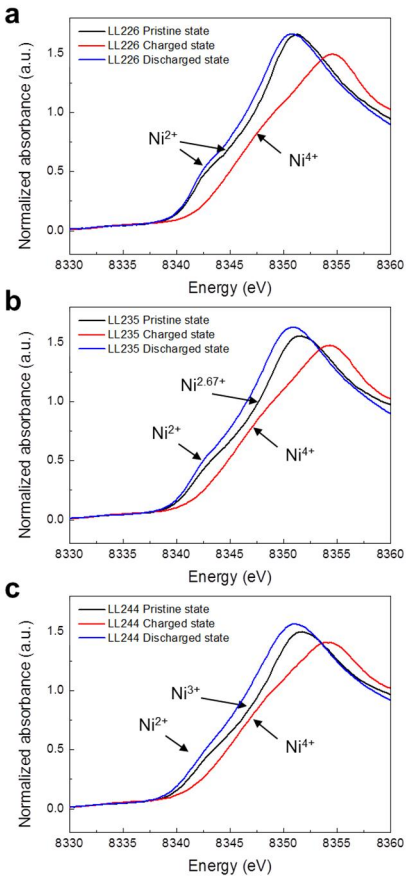

Figure 2.11. Ni K-edge XANES spectra of a) LL226, b) LL235, and c) LL244 electrodes at pristine (black), charged to 4.8 V (red), and discharged to 2.0 V (blue). Nickel divalent/tetravalent redox reactions occur in all compounds regardless of initial oxidation states of nickel ions.

2.3.4. Structural evolution with cycling

To elucidate the observed difference in the voltage decay and the effect of the nickel redox buffer, structural analyses were performed for each LLNMO sample after cycling using high-resolution transmission electron microscopy (HR-TEM) and XRD. Figure 2.12a and b compare the local atomic structure of the LL226 electrode before and after cycling in the zone axis along the $[-441]_R//[10-1]_M$ (R and M represent the rhombohedral $R\bar{3}m$ and monoclinic C2/m structures, respectively) direction, which is also parallel to the [001] direction of cubic Fd-3m. Although the pristine LL226 electrode exhibited the structure of typical lithium-rich layered oxides with domains of $R\bar{3}m$ and C2/m structures, as shown in Figure 2.12a, additional diffraction spots (highlighted with red circles) are clearly observed after cycling, as shown in Figure 2.12b. These additional diffraction spots can be better visualized in the intensity histogram of the red boxed region shown in the inset; they cannot be assigned to any planes of the layered phase but can be indexed as the {220} planes of the cubic spinel phase.[40] The (220)C plane is distinguished from the parallel planes of the layered phase by the presence of transition metals in the lithium layers (Figure 2.13), thereby indicating the formation of disordered domains, which is indicative of significant interlayer migration of transition metal ions in LL226 after cycling. Similar observations were made in other regions of particles, as shown in Figure 2.14; these findings are consistent with those presented in previous reports on LLNMOs, implying the correlation between the activated manganese redox activity and the transition

migration.[4, 5, 40, 41] In contrast, the cycled LL244 electrode did not exhibit a notable signature of the local phase transformation involving transition metal migration, preserving the pristine layered framework, as observed in Figure 2.12c and d. The additional $(220)_c$ spots that were easily detected in the cycled LL226 electrode were not detectable along the same zone axis in the HR-TEM analysis of the cycled LL244 electrodes. This apparently different behavior in the local structure change was also confirmed in XRD patterns, as shown in Figure 2.15, which indicated that the cycled LL244 electrode exhibited a much lower degree of cation disordering than the cycled LL226 and LL235 electrodes, suggesting the structural integrity of LL244 as a layered structure after cycling.

I further examined the changes in the atomic arrangements of the samples after cycling using Raman spectroscopy, which has been demonstrated to be particularly sensitive to changes in metal–oxygen bonds in layered and disordered layered (or spinel) structures.[4, 21, 42, 43] Figure 2.12e compares the Raman spectra of the LL226, LL235, and LL244 electrodes after electrochemical cycling. Initially, all three samples exhibited similar patterns characteristic of layered structures with a trace of Li_2MnO_3-like domains (Figure 2.16). However, after cycling, notable differences were observed in the spectra. Most importantly, the symmetrical M–O stretching peak of the pristine structure split into two peaks near 627 and 572 cm^{-1}, which were attributed to symmetrical stretching (A_{1g}) in the spinel-like $Li_{1+x}M_2O_4$ structure and the A_{1g} mode of the pristine layered structure that appears at relatively lower frequency, respectively[44] (see Figure 2.16 in the

supporting information for further details). This finding suggests the coexistence of two different bonding environments (*i.e.*, phases) after electrochemical cycling, which is consistent with previous studies on LL226.[4, 5] Moreover, the ratio between the A_{1g} peaks of the spinel-like and layered phases sensitively depended on the composition of the LLNMO compounds. The LL244 compound contained the lowest fraction of the spinel-like phase, which is consistent with the previously presented TEM and XRD results. The calculated portions of the spinel A_{1g} peak area to the total peak area were 57%, 48%, and 22% for LL226, LL235, and LL244, respectively, which confirms that the structure remained intact as a layered structure for the LL244 electrode even after electrochemical cycling in contrast to the cycled LL226 electrode.

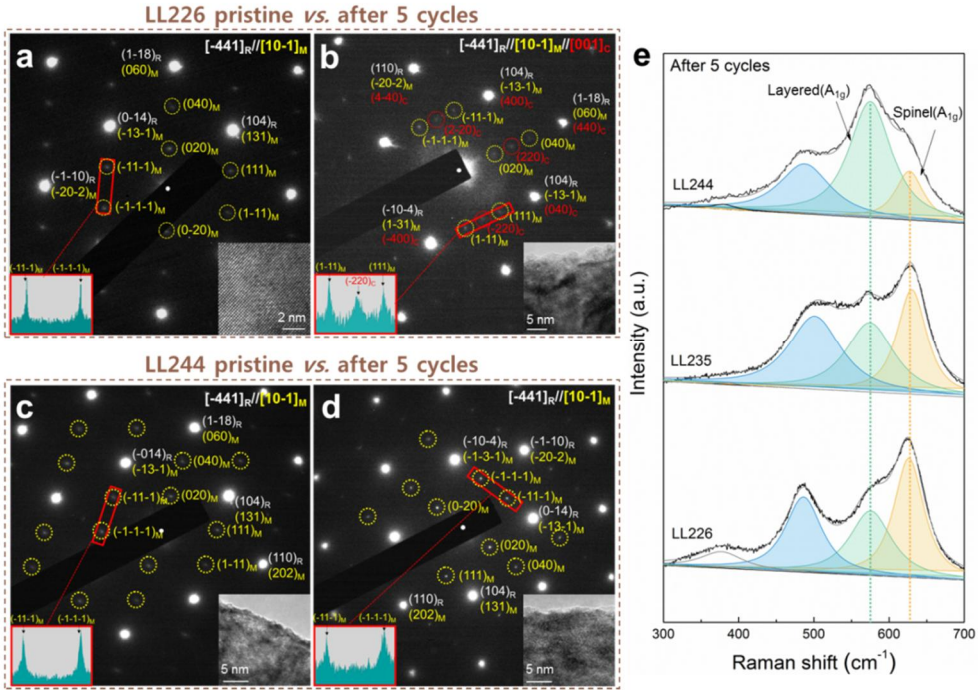

Figure 2.12. Structural variations in LLNMO after electrochemical cycling. SAED pattern of LL226 a) before and b) after five cycles and that of LL244 c) before and d) after five cycles along the $[-441]_R$ direction, which is parallel to the $[10\text{-}1]_M$ direction of monoclinic C2/m and $[001]_C$ direction of cubic Fd-3m (spinel phase). HR-TEM images and the intensity histograms of the red boxed regions are presented in the insets of the SAED patterns. e) Raman spectra of LLNMOs after five cycles. The orange and green peaks are attributed the A1g mode of the spinel and layered phases, respectively, whereas the blue peaks are attributed both to the E_g mode of the layered phase and F_{2g} mode of the spinel phase.

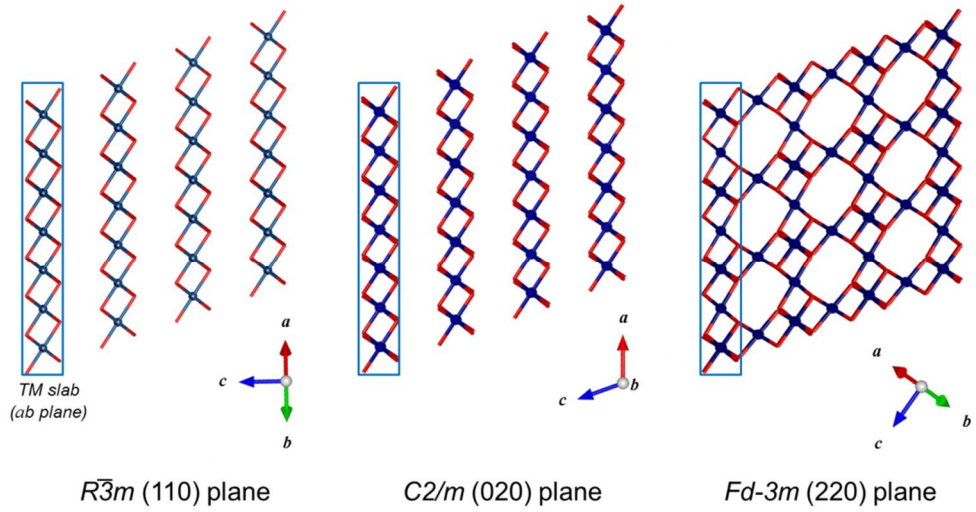

Figure 2.13. Structural differences between the layered $(110)_R//(020)_M$ planes and spinel $(220)_C$ plane. The formation of spinel-like phases in LLNMO after cycling takes place by the interlayer migration of the transition metal ions between the transition metal slabs.

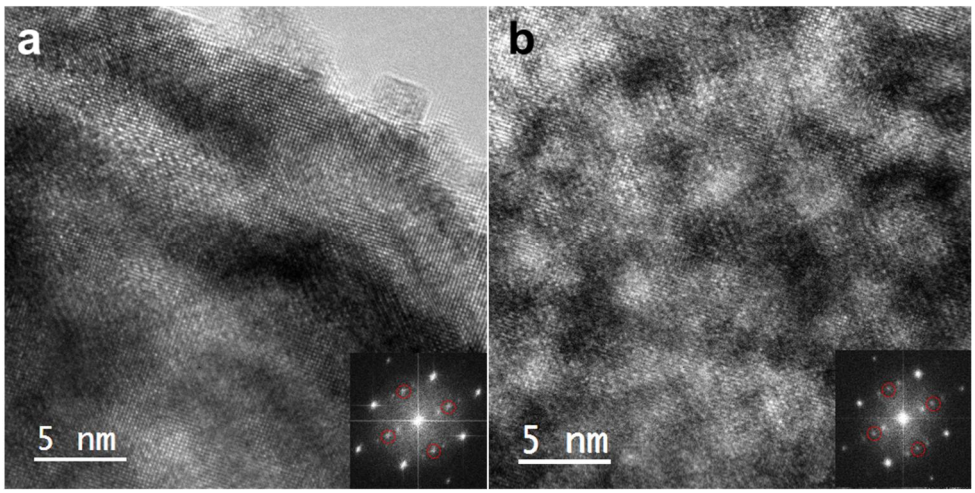

Figure 2.14. HR-TEM images and corresponding Fast Fourier transform (FFT) images of cycled LL226. Red circles in the FFT images denotes the {220} planes of the cubic spinel phase.

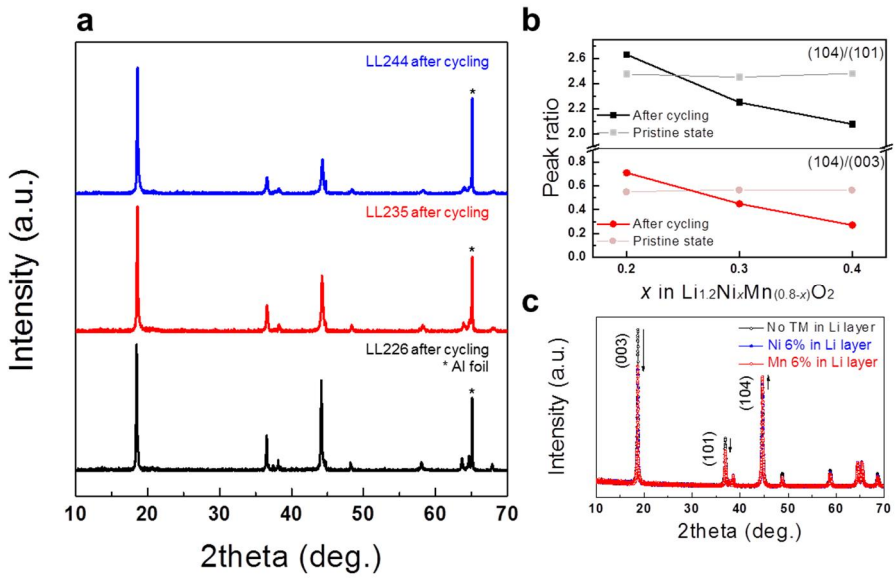

Figure 2.15. Structural variations in LLNMO after electrochemical cycling. a) XRD patterns of LL226 (black), LL235 (red), and LL244 (blue) after five electrochemical cycles. b) Peak ratio of (104)/(101) (black) and (104)/(003) (red) of LLNMOs before and after cycling. c) Simulated XRD patterns of LLNMO with no transition-metal ions in Li layers (black) and with 6% Ni (blue) or Mn (red) migration into Li layers.

The overall structural evolution was examined using XRD, and the results are presented in Figure 2.15. The most obvious difference in the XRD patterns of the LLNMOs after cycling is the ratio among several important Bragg peaks, which indicates the degree of transition-metal ordering.[45, 46] In the XRD patterns of LL226 after cycling, the intensity ratio of the (003)/(104) peak became notably smaller compared with those of LL235 and LL244, as observed in Figure 2.15a.

For a clear comparison, I plotted the ratio of the (104) peaks at 44.1° to the (101) peaks at 36.5° and to the (003) peaks at 18.5° for LLNMOs in pristine states and after electrochemical cycling (Figure 2.15b). In the pristine states, the ratios of the (104) peak to the (101) and (003) peaks were almost identical for the three compounds in the ranges of 2.455–2.480 and 0.545–0.565, respectively. However, after five cycles, the peak intensities dramatically changed, which resulted in differences between the ratios for the LLNMOs with varying compositions. For LL226 with low Ni content, the ratios of the (104) peak to both the (101) and (003) peaks increased to 2.63 and 0.71, respectively, whereas the values significantly decreased to 2.08 and 0.27, respectively, for LL244 with high Ni content. The increase of the ratios of LL226 is consistent with our simulated XRD patterns (Figure 2.15c), which qualitatively showed that the (104) peak grows whereas the (003) and (101) peaks diminish as some portion (~6%) of the transition-metal ions migrate into the Li layer, reducing the contrast between the transition-metal and lithium layers. In contrast, the decrease of the ratios of LL244 indicates the increased contrast between the transition-metal and lithium layers, which might originate from the lattice densification of the transition-metal layers. Previous NMR and XRD studies have revealed the substitution of vacancies (the original Li sites in transition-metal layers) with migrated transition-metal species.[47, 48]

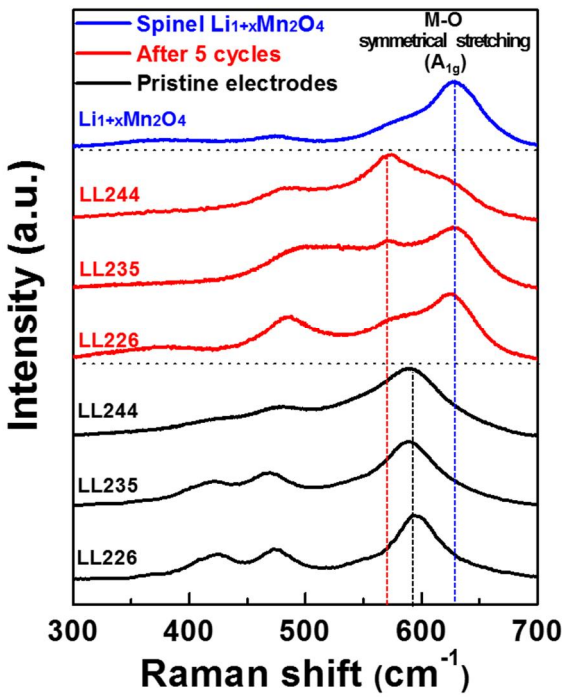

Figure 2.16. Structural variations in LLNMO after electrochemical cycling.

Raman spectra of LLNMOs before (black) and after five cycles (red) compared with spinel $Li_{1+x}Mn_2O_4$ (blue). Red dotted line and blue dotted line indicate A_{1g} mode of layered and spinel phases, respectively. The two peaks near 595 and 474 cm^{-1} correspond to the A_{1g} (symmetrical stretching of M–O) and E_g (symmetrical deformation) vibrational modes in layered lithium transition metal oxides with $R\bar{3}m$ symmetry, and the small peak at 425 cm^{-1} originates from the Li_2MnO_3-like structure with the lower C2/m symmetry. The intensity of the peak at 425 cm^{-1} increased with increasing Mn content in the samples, implying a higher degree of

ordering, which is consistent with the observation of the superstructure patterns in the XRD results (Figure 2.2a). The single A^{1g} mode for the pristine compounds indicates that the layered $LiMO_2$ and Li_2MnO_3 phases share a common layered lattice framework. The peak shift of A_{1g} mode of the pristine layered structure after cycling reflects the increase in the average mass of the atoms in the transition metal layers, which might be induced by the lattice densification. The densification is also consistent with the disappearance of the peak at 425 cm^{-1}, corresponding to the honeycomb-like ordering in the transition metal layers in our Raman study as well as the XRD results (Figure 2.15).

2.3.5. Discussion

Based on the observations above, I propose the following mechanism for the electrochemical redox reactions occurring in the LLNMO electrodes with and without the Ni^{3+} redox buffer. During the first charge, the initial delithiation (> ~ 4.4 V) occurs via the oxidation of Ni^{2+} (LL226), $Ni^{2.67+}$ (LL235), or Ni^{3+} (LL244) to Ni^{4+}, accounting for the 0.4 Li^{+} ion extraction from each electrode. The remaining 0.8 Li^{+} ions are further delithiated with the concurrent oxidation of the oxygen, corresponding to the observed plateau at ~4.4–4.5 V (vs. Li/Li+) for all the electrodes. At the end of charge, the valence states of both nickel and manganese are +4 regardless of the Ni/Mn ratios in the LLNMO electrodes. Upon discharge, the re-lithiation involves the cationic reduction of nickel along with possible oxygen anionic reduction. However, when the loss of the oxygen anionic redox activity occurs due to irreversible oxygen gas evolution or other possible mechanisms that remain elusive,[6, 19-21, 47, 49, 50] the subsequent re-lithiation occurs at different cationic redox centers in each LLNMO electrode. For the LL226 electrode containing the least amount of nickel, Mn4+ serves as an additional redox center to compensate for the loss of the oxygen anionic redox. However, for the LL244 electrode, the extra redox contribution can originate from the Ni^{3+}/Ni^{2+} redox because of the presence of the Ni^{3+} redox buffer, which is sufficiently rich to compensate for the loss of the partial oxygen anionic redox. Because the redox potential of Ni^{2+}/Ni^{3+} lies above that of Mn^{3+}/Mn^{4+}, it is possible to suppress the contribution of the manganese redox activity in the LLNMO with the Ni^{3+} redox

buffer. For the LL235 electrode, some portion of the Mn^{4+} reduction to Mn^{3+} may occur simultaneously for the full re-lithiation. As the Mn^{3+} ions are subsequently prone to inducing the layered to disordered spinel-like phase transformation,[22, 23] the additional Mn^{3+} in the cycled electrode facilitates the formation of the disordered spinel-like phase and induces a stronger voltage fade such as in the LL226 electrode. In contrast, the cycled LL244 electrode, which does not require the manganese reduction, can better maintain the layered phase, thereby avoiding the voltage depression. Presently, it is unclear whether the manganese reduction leads to the transition migration or whether the transition migration gives rise to the partial manganese redox activity; this issue should be addressed in a future study.[7] In this regard, a recent study on sodium lithium manganese layered oxides, $Na_{0.6}[Li_{0.2}Mn_{0.8}]O_2$, with P3-type structure where the oxygen is proposed to be the only redox couple, is noted in that no voltage decay and reversible voltage plateaus are observed.[51] Nevertheless, the results of our study indicate that the suppression of the manganese reduction by the introduction of the nickel redox buffer could significantly suppress the structural disordering and voltage decay, offering clearer guidance in the design and compositional tailoring of Li-rich layered oxides.

2.4. Concluding Remarks

In summary, I proposed a new strategy to suppress the voltage decay in LLNMO electrodes by introducing a Ni^{3+} redox buffer that can subdue the redox activity of manganese and its migration in the layered structure. Investigations of a series of LLNMO electrodes confirmed that introduction of the Ni^{3+} redox buffer led to significant reduction of the voltage decay during cycling, successfully preserving the pristine layered structure. The suppression of the voltage decay was correlated to a decrease in the Mn^{3+} content resulting from the Mn^{4+} reduction during the discharge reaction, which could be systematically tailored by the presence of the Ni^{3+} redox buffer, enabling extended nickel redox activity from Ni^{3+}/Ni^{4+} to Ni^{2+}/Ni^{4+} after the partial loss of the oxygen anionic redox. The findings of this study suggest that to suppress the voltage decay of layered lithium-rich transition metal oxides, it is critical to deal with the cation migration that induces the formation of the disordered spinel-like domain. In addition, tailoring of the oxidation states of nickel and manganese not only in the pristine states but also during electrochemical cycling can offer an effective way to prevent the voltage decay in LLNMOs without the use of 4d or 5d elements.

2.5. References

[1] K. Kang, Y. S. Meng, J. Bréger, C. P. Grey, G. Ceder, *Science* **2006**, 311, 977.

[2] Z. Lu, D. D. MacNeil, J. R. Dahn, *Electrochem. Solid-State Lett.* **2001**, 4, A191.

[3] J. Hong, H. Gwon, S.-K. Jung, K. Ku, K. Kang, *J. Electrochem. Soc.* **2015**, 162, A2447.

[4] J. Hong, D.-H. Seo, S.-W. Kim, H. Gwon, S.-T. Oh, K. Kang, *J. Mater. Chem.* **2010**, 20, 10179.

[5] B. Xu, C. R. Fell, M. Chi, Y. S. Meng, *Energy Environ. Sci.* **2011**, 4, 2223.

[6] N. Yabuuchi, K. Yoshii, S.-T. Myung, I. Nakai, S. Komaba, *J. Am. Chem. Soc.* **2011**, 133, 4404.

[7] W. E. Gent, K. Lim, Y. Liang, Q. Li, T. Barnes, S.-J. Ahn, K. H. Stone, M. McIntire, J. Hong, J. H. Song, Y. Li, A. Mehta, S. Ermon, T. Tyliszczak, D. Kilcoyne, D. Vine, J.-H. Park, S.-K. Doo, M. F. Toney, W. Yang, D. Prendergast, W. C. Chueh, *Nat. Commun.* **2017**, 8, 2091.

[8] M. Sathiya, K. Ramesha, G. Rousse, D. Foix, D. Gonbeau, A. S. Prakash, M. L. Doublet, K. Hemalatha, J. M. Tarascon, *Chem. Mater.* **2013**, 25, 1121.

[9] M. Sathiya, A. M. Abakumov, D. Foix, G. Rousse, K. Ramesha, M. Saubanère, M. L. Doublet, H. Vezin, C. P. Laisa, A. S. Prakash, D. Gonbeau, G. VanTendeloo, J. M. Tarascon, *Nat. Mater.* **2015**, 14, 230.

[10] A. Grimaud, A. Demortière, M. Saubanère, W. Dachraoui, M. Duchamp,

M.-L. Doublet, J.-M. Tarascon, *Nat. Energy* **2016**, 2, 16189.

[11] A. J. Perez, Q. Jacquet, D. Batuk, A. Iadecola, M. Saubanère, G. Rousse, D. Larcher, H. Vezin, M.-L. Doublet, J.-M. Tarascon, *Nat. Energy* **2017**, 2, 954.

[12] N. Yabuuchi, M. Takeuchi, M. Nakayama, H. Shiiba, M. Ogawa, K. Nakayama, T. Ohta, D. Endo, T. Ozaki, T. Inamasu, K. Sato, S. Komaba, *Proceedings of the National Academy of Sciences* **2015**, 112, 7650.

[13] J. Lee, D.-H. Seo, M. Balasubramanian, N. Twu, X. Li, G. Ceder, *Energy Environ. Sci.* **2015**, 8, 3255.

[14] P. E. Pearce, A. J. Perez, G. Rousse, M. Saubanère, D. Batuk, D. Foix, E. McCalla, A. M. Abakumov, G. Van Tendeloo, M.-L. Doublet, J.-M. Tarascon, *Nat. Mater.* **2017**, 16, 580.

[15] S.-K. Jung, K. Kang, *Nat. Energy* **2017**, 2, 912.

[16] C. Zhan, Z. Yao, J. Lu, L. Ma, V. A. Maroni, L. Li, E. Lee, E. E. Alp, T. Wu, J. Wen, Y. Ren, C. Johnson, M. M. Thackeray, M. K. Y. Chan, C. Wolverton, K. Amine, *Nat. Energy* **2017**, 2, 963.

[17] S. Kim, M. Aykol, V. I. Hegde, Z. Lu, S. Kirklin, J. R. Croy, M. M. Thackeray, C. Wolverton, *Energy Environ. Sci.* **2017**, 10, 2201.

[18] E. McCalla, A. M. Abakumov, M. Saubanère, D. Foix, E. J. Berg, G. Rousse, M.-L. Doublet, D. Gonbeau, P. Novák, G. Van Tendeloo, R. Dominko, J.-M. Tarascon, *Science* **2015**, 350, 1516.

[19] J. Hong, H.-D. Lim, M. Lee, S.-W. Kim, H. Kim, S.-T. Oh, G.-C. Chung, K. Kang, *Chem. Mater.* **2012**, 24, 2692.

[20] K. Luo, M. R. Roberts, N. Guerrini, N. Tapia-Ruiz, R. Hao, F. Massel, D. M. Pickup, S. Ramos, Y.-S. Liu, J. Guo, A. V. Chadwick, L. C. Duda, P. G. Bruce, *J. Am. Chem. Soc.* **2016**, 138, 11211.

[21] S. Hy, F. Felix, J. Rick, W. N. Su, B. J. Hwang, *J. Am. Chem. Soc.* **2014**, 136, 999.

[22] J. Reed, G. Ceder, A. Van Der Ven *Electrochem. Solid-State Lett.* **2001**, 4, A78.

[23] S. Choi, A. Manthiram, *J. Electrochem. Soc.* **2002**, 149, A1157.

[24] J. C. Knight, A. Manthiram, *J. Mater. Chem. A* **2015**, 3, 22199.

[25] S. Chong, Y. Liu, W. Yan, Y. Chen, *RSC Advances* **2016**, 6, 53662.

[26] B. Ravel, M. Newville, *Journal of synchrotron radiation* **2005**, 12, 537.

[27] H.-J. Noh, S. Youn, C. S. Yoon, Y.-K. Sun, *J. Power Sources* **2013**, 233, 121.

[28] A. Van der Ven, G. Ceder, *Electrochem. Commun.* **2004**, 6, 1045.

[29] Y. S. Meng, G. Ceder, C. P. Grey, W. S. Yoon, M. Jiang, J. Bréger, Y. Shao-Horn, *Chem. Mater.* **2005**, 17, 2386.

[30] H. Kobayashi, M. Tabuchi, M. Shikano, H. Kageyama, R. Kanno, *J. Mater. Chem.* **2003**, 13, 957.

[31] J. Bréger, M. Jiang, N. Dupré, Y. S. Meng, Y. Shao-Horn, G. Ceder, C. P. Grey, *J. Solid State Chem.* **2005**, 178, 2575.

[32] V. F. Sears, *Neutron News* **1992**, 3, 26.

[33] L. Vegard, *Zeitschrift für Physik* **1921**, 5, 17.

[34] A. R. Armstrong, M. Holzapfel, P. Novák, C. S. Johnson, S.-H. Kang, M. M. Thackeray, P. G. Bruce, *J. Am. Chem. Soc.* **2006**, 128, 8694.

[35] K. Luo, M. R. Roberts, R. Hao, N. Guerrini, D. M. Pickup, Y.-S. Liu, K. Edström, J. Guo, A. V. Chadwick, L. C. Duda, P. G. Bruce, *Nat Chem* **2016**, 8, 684.

[36] G. Assat, D. Foix, C. Delacourt, A. Iadecola, R. Dedryvère, J.-M. Tarascon, *Nat. Commun.* **2017**, 8, 2219.

[37] J.-L. Shi, J.-N. Zhang, M. He, X.-D. Zhang, Y.-X. Yin, H. Li, Y.-G. Guo, L. Gu, L.-J. Wan, *ACS Appl. Mater. Interfaces* **2016**, 8, 20138.

[38] A. Rougier, C. Delmas, A. V. Chadwick, *Solid State Commun.* **1995**, 94, 123.

[39] A. Ito, Y. Sato, T. Sanada, M. Hatano, H. Horie, Y. Ohsawa, *J. Power Sources* **2011**, 196, 6828.

[40] M. Gu, I. Belharouak, J. Zheng, H. Wu, J. Xiao, A. Genc, K. Amine, S. Thevuthasan, D. R. Baer, J.-G. Zhang, N. D. Browning, J. Liu, C. Wang, *ACS Nano* **2012**, 7, 760.

[41] P. Oh, M. Ko, S. Myeong, Y. Kim, J. Cho, *Adv. Energy Mater.* **2014**, 4, 1400631.

[42] S.-J. Hwang, H.-S. Park, J.-H. Choy, G. Campet, J. Portier, C.-W. Kwon, J. Etourneau, *Electrochem. Solid-State Lett.* **2001**, 4, A213.

[43] S. Loridant, L. Abello, E. Siebert, G. Lucazeau, *Solid State Ionics* **1995**, 78, 249.

[44] S.-J. Hwang, H.-S. Park, J.-H. Choy, G. Campet, *Chem. Mater.* **2000**, 12,

1818.

[45] T. Ohzuku, A. Ueda, M. Nagayama, Y. Iwakoshi, H. Komori, *Electrochim. Acta* **1993**, 38, 1159.

[46] O. Tsutomu, M. Yoshinari, *Chem. Lett.* **2001**, 30, 744.

[47] N. Tran, L. Croguennec, M. Ménétrier, F. Weill, P. Biensan, C. Jordy, C. Delmas, *Chem. Mater.* **2008**, 20, 4815.

[48] M. Jiang, B. Key, Y. S. Meng, C. P. Grey, *Chem. Mater.* **2009**, 21, 2733.

[49] F. La Mantia, F. Rosciano, N. Tran, P. Novák, *J. Electrochem. Soc.* **2009**, 156, A823.

[50] Y. Xie, M. Saubanere, M. L. Doublet, *Energy Environ. Sci.* **2017**, 10, 266.

[51] X. Rong, J. Liu, E. Hu, Y. Liu, Y. Wang, J. Wu, X. Yu, K. Page, Y.-S. Hu, W. Yang, H. Li, X.-Q. Yang, L. Chen, X. Huang, *Joule* **2018**, 2, 125.

Chapter 3. A new lithium diffusion model in layered oxides based on asymmetric but reversible transition metal migration

3.1. Research background

The development of high-energy-density cathode is pivotal in the progress of lithium-ion batteries (LIBs) and meeting the recent surging needs on advanced LIBs for electric vehicles.[1, 2] Recent discovery of anionic redox reaction in lithium-rich layered oxides ($Li[Li_xTM_{1-x}]O_2$, hereafter called LLO) opens up a new possible route toward the high-energy-density cathode. While conventional cathode materials, such as $LiCoO_2$ and $LiNi_xCo_yMn_zO_2$, exploit mainly cationic redox reactions from transition metals (TM), LLO can potentially exhibit higher capacities cumulating both the cationic and additional anionic redox processes.[3-8] Early works on the LLO, mainly regarding the $Li(Li_xNi_yMn_{1-x-y})O_2$, showed that the extra capacity could be achieved utilizing the oxygen redox reaction boosting the energy density. However, serious voltage decay accompanying the substantial loss of the energy density over cycles has been chronical issues, which was attributed to the irreversible TM migrations destabilizing the structure.[6, 9-11] Other lithium-rich phases based on 4*d* or 5*d* TM such as Li_2RuO_3 and Li_2IrO_3 were subsequently explored with a better integrity of the structure involving less

irreversible TM migrations and voltage decay. Yet, the use of scarce 4*d* or 5*d* TM makes them practically unaffordable.[10, 12]

While the origin of the anionic redox is still under debate,[13-21] it is commonly accepted that the local environment of oxygen in the crystal is important in activating the anionic redox reaction. Seo *et al.* demonstrated that the presence of non-bonding oxygen due to the absence of TM in the transition metal layer is the origin of the extra capacity in the lithium-rich layered oxides.[13] Accordingly, Perez *et al.* further proposed that the oxygen redox activity is also sensitively affected by the oxygen coordination with TMs and oxygen/TM ratio in the materials.[21] In the meantime, Gent *et al.* suggested that the TM migration/redistribution in LLOs is closely correlated with the triggering of the anionic redox.[18] It was claimed that reversible TM migration to the lithium layer is intrinsically coupled to the oxygen redox potential, and the oxygen redox mechanism is a dynamic process involving substantial redistributions in the oxygen/TM coordinations.

Recent experimental and computational results have confirmed that TM migration can occur reversibly, to some extent, during charge and discharge in LLOs.[10, 18, 22-24] While its effect on the oxygen redox in LLOs is under intense scrutiny, the consequences of reversible TM migrations on the general lithiation/de-lithiation model in layered electrodes have been rarely elucidated. Indeed, it is noteworthy that the misplacement of TM in the layered oxides has been simply supposed to be undesirable for the lithium mobility. According to the early works,

it was demonstrated that the presence of TM in the lithium layer reduces the lithium slab space, thus increases the repulsion between the migrating lithium and the TM in the transition metal layer, resulting in higher activation barriers for lithium diffusion.[3, 25, 26] It has been also experimentally verified that, in $LiNiO_2$ or $LiNi_{0.5}Mn_{0.5}O_2$ system, as the amount of TM in lithium sites (cation mixing) increases in the pristine materials, the lithium diffusion gets sluggish, significantly losing the capacity.[3, 25, 27-29] Whereas these early studies revealed the effect of the defective TMs on the lithium mobility, the defects were regarded as stationary irrespective of the lithium motion, and the lithium de/intercalation has been believed to take place still topotactically without altering the layered framework. In this rigid structure model, the lithium diffusion mechanism/kinetics is unaffected regardless of whether it is a lithiation process or a de-lithiation process due to the invariance of the framework involving TM. Since the evidences of reversible TM migration are found as the structural part of the redox process in the LLOs electrode, more clear understanding on the TM migration during charge/discharge and its correlation with lithium diffusion behavior is required.

Herein, I report that the TM migrations and the lithium diffusion are sensitively correlated in the LLO materials, influencing the overall lithium diffusion mechanism and the kinetics. Importantly, it is demonstrated that TM migration occurs asymmetrically during de-lithiation and lithiation, and thus the diffusion kinetics in the two processes become substantially distinguished. It is shown that, due to the asymmetric and reversible TM migration, the discharge

(lithiation) process is more kinetically inhibited compared with the charge (de-lithiation) from the careful investigations on $Li(Li_{0.2}Ni_{0.4}Mn_{0.4})O_2$ (LNM244), which has been recently reported as a LLO material with suppressed voltage decay.[30] I propose that an asymmetric TM migration is caused by the distinct local environments created by TM in the lithium layer during charge, which are difficult to be reversed following the previous paths during discharge. This study suggests that a new lithium diffusion model should be considered encompassing the dynamic TM migration and correlative lithium motion in the layered lithium transition meal oxides.

3.2. Experimental Methods

3.2.1. Synthesis of $Li_{1.2}Ni_{0.4}Mn_{0.4}O_2$

Stoichiometric amounts of Li_2CO_3, NiO and $MnCO_3$ (all precursors were purchased from Sigma-Aldrich, USA) were ball milled in planetary ball miller (Fritsch, Germany) for 6 hours at 400 rpm. And the resultant powders were heated at 900 °C (5 °C min^{-1}) for 8 hours in air then furnace cooled. Phase of the obtained powder samples were characterized using D2 PHASER (Bruker, Bremen, Germany) equipped with Cu Kα radiation source (λ = 1.54178 Å).

3.2.2. Electrochemical tests

A slurry of 80 wt % active materials, 10 wt % of carbon black (super P, Timcal, Switzerland), and 10 wt % polyvinylidene fluoride (PVDF, Sigma Aldrich) binder, dissolved in N-methyl-1,2-pyrrolidone (NMP; Sigma-Aldrich, USA), was cast onto Al foil. NMP was evaporated overnight at 70 °C in a vacuum oven. Electrode sheets were calendared before using. Coin cells (CR2032, Hohsen, Japan) were assembled with the working electrode, Li counter electrode, separator (GF/F, Whatman, UK), and a 1M solution of LiPF6 in ethyl carbonate/dimethyl carbonate (EC/DMC, 1:1 v/v) in an argon-filled glove box. The galvanostatic cycling was performed over the voltage ranges of 2.0-4.8 V by a potentiogalvanostat (WBCS 3000, WonA Tech, Korea) under 12.5 mA g^{-1} at 298 and 358 K in temperature controlled chamber. The cell is fully rested after cell is transferred to the chamber

with different temperature.

3.2.3. Characterization of materials

Aberration corrected transmission electron microscope JEOL-ARM200F was used to perform high-angle annular-dark-field (HAADF) imaging. Raman spectra were taken using a Horiba Jobin Yvon LabRam Aramis with an Ar-ion laser beam at an exciting radiation wavelength of 514.5nm. XANES spectra were obtained from beamline 7D at the Pohang Accelerator Laboratory (PAL), Republic of Korea. The Mn and Ni k-edge spectra were collected in transmission mode with an electron energy of 2.5 GeV and a current of 300 mA.

3.3. Results and Discussions

3.3.1. Kinetic limitations during lithiation process

I begin with the consistent observations from the series of electrochemical tests that the discharge process is more kinetically inhibited than the charge process for LNM244 electrodes after the activation pre-cycles as shown in Figure 3.1. (Details on the pre-cycle are provided in 3.2.) For a comparison, first, I fully charged the electrode at elevated temperature and discharged at various current rates at room temperature, and, equivalent tests were also carried out to examine the rate capability during charge process in Figure 3.1a. The figures present that the retention of the discharge capacity is notably inferior to the case of the charge. The increase in the C-rate from C/20 to 1C reduces the capacity by 64 % in the discharge, which is much lower than 88 % in the same conditions of the charge. To support this result, I also performed temperature-controlled experiments for each charge and discharge process, where the electrodes were comparatively discharged (or charged) at two different temperatures (25 °C and 60 °C) and its temperature-dependent capacity retentions were investigated. Figure 1b illustrates that the discharge capacity at 60 °C (245 mAh g^{-1}) is substantially larger than that at 25 °C (187 mAh g^{-1}), and the difference is as much as ~ 60 mAh g^{-1}, which indicates the significant kinetical loss of the capacity during discharge at room temperature. On the other hand, when the fully discharged cells are charged at 25 °C and 60 °C, respectively, the difference in the charging capacities is much smaller than the case of the discharge, and almost 90% of the capacity is obtainable at 25 °C compared

with that of 60 °C. It supports our unexpected observation that the charging (*i.e.* de-lithiation) kinetics is faster than the discharging (*i.e.* lithiation) process in this material. Additionally, I found that when the charged cell at 25 °C in Figure 3.1c is subsequently discharged at 25 °C, the following discharge capacity significantly reduces again in consistent with the results in Figure 3.1b, as presented in Figure 3.4. It implies that only limited amount of lithium could be re-intercalated during 25 °C discharge, even though the charge at 25 °C could create sufficient number of vacant lithium sites.

The insufficient intercalation during room-temperature (25 °C) discharge and the presence of substantial amount of unoccupied lithium sites could be confirmed from the following additional experiments. First, I attempted to discharge the electrode with a cutoff capacity of 250 mAh g^{-1}, considering the discharging capacity at 60 °C that could be delivered for the same charged electrode (Figure 3.1d). In consistent with the results of 25 °C in Figure 3.1b, the discharge capacity of only ~180 mAh g^{-1} could be delivered following the normal discharge profile to ~2 V. The further discharge was found to occur exhibiting a low voltage plateau region as indicated with a black arrow, which will be discussed in detail later. However, to our surprise, it was observed that, upon the following subsequent charging at room temperature, the low voltage plateau did not appear anymore and the charge capacity of near 250 mAh g^{-1} could be fully presented. It strongly implies that the discharge capacity delivered at the voltage of ~ 2 V does not originate from irreversible side reactions but corresponds to the actual lithium

intercalation. It is well known that such voltage plateau lower than 2 V generally appears when layered oxides are over-lithiated, where additional lithium ions are intercalated into the tetrahedral sites other than octahedral sites in the structure.[31-33] This was also confirmed from our own experiments (Figure 3.5) that the same low-voltage plateau is observed when the pristine layered material is initially discharged without charge due to the fully filled lithium octahedral sites. Nevertheless, it is puzzling that (i) the tetrahedral lithium occupancy occurs for the electrode even with a sufficient amount of vacant octahedral sites available in the structure, and (ii), upon the following charging process, all the lithium ions are extracted from the octahedral sites, as indicated from the normal charge profile above 3 V.

I found that the lithium intercalation into tetrahedral sites results from a kinetically retarded lithiation process, and the proper relaxations lead to spontaneous migrations of tetrahedral lithium to the vacant octahedral sites, thus all the de-lithiation process can take place solely from the octahedral lithium ions. Figure 3.1e displays the GITT (galvanostatic intermittent titration technique) discharge profile taken at 25 °C plotted together with the galvanostatic discharge profile obtained at 60 °C. It is obviously shown that the observed low-voltage plateau has undergone the large polarizations (as indicated with green shadow), and the quasi open circuit voltage (QOCV) and the corresponding capacity in the green region coincide with the discharge profile of 60 °C. It indicates that, a large kinetic barrier inhibited the octahedral site occupancies in the green shadow region, thus

forced lithium ions to occupy the tetrahedral sites at 25 °C; on the other hand, the short relaxation periods could allow the tetrahedral lithium ions to move to octahedral sites, exhibiting the QOCV of ~ 3V. Figure 3.6 presents additional evidences of kinetically-driven tetrahedral lithium occupancy even with the presence of the vacant octahedral sites. It demonstrates that the loss of the capacity with the cutoff of 2 V at 25 °C can be simply recovered with additional discharge at 60 °C displaying a typical discharge profile > 3V. These observations consistently illustrate the substantial kinetic limitations in the lithium intercalation process.

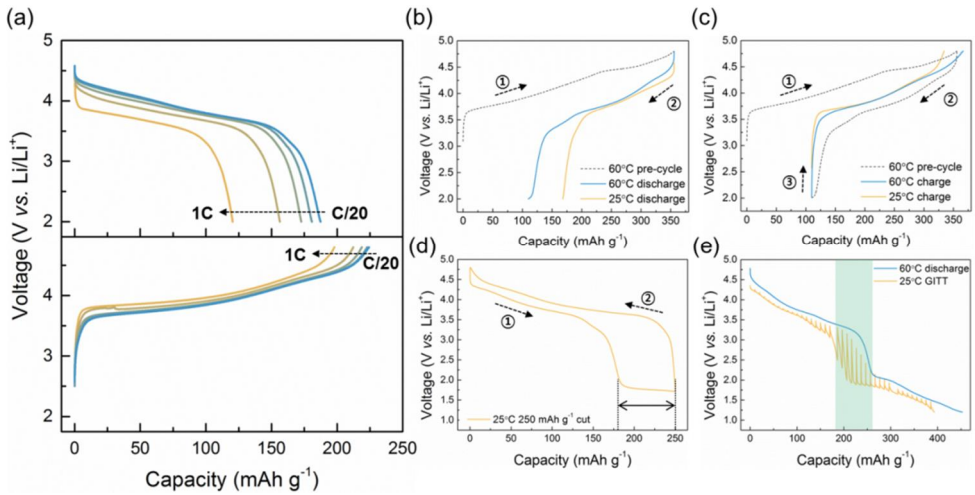

Figure 3.1. Electrochemical profiles using various protocols. (a) Electrochemical profiles of discharge and charge at 25 °C from various C-rates (1C, C/5, C/10, C/15, C/20) after respective pre-cycle at 60 °C. (b) Comparison of 60 °C (blue) and 25 °C discharge (orange) after 60 °C charge (dotted line). (c) Comparison of 60 °C (blue) and 25 °C (orange) charge after 60 °C 1 cycle (dotted line). (d) 25 °C discharge until 250 mAh g^{-1} and charge. (e) GITT on 25 °C discharge (orange). It is compared with 60 °C discharge profile (blue).

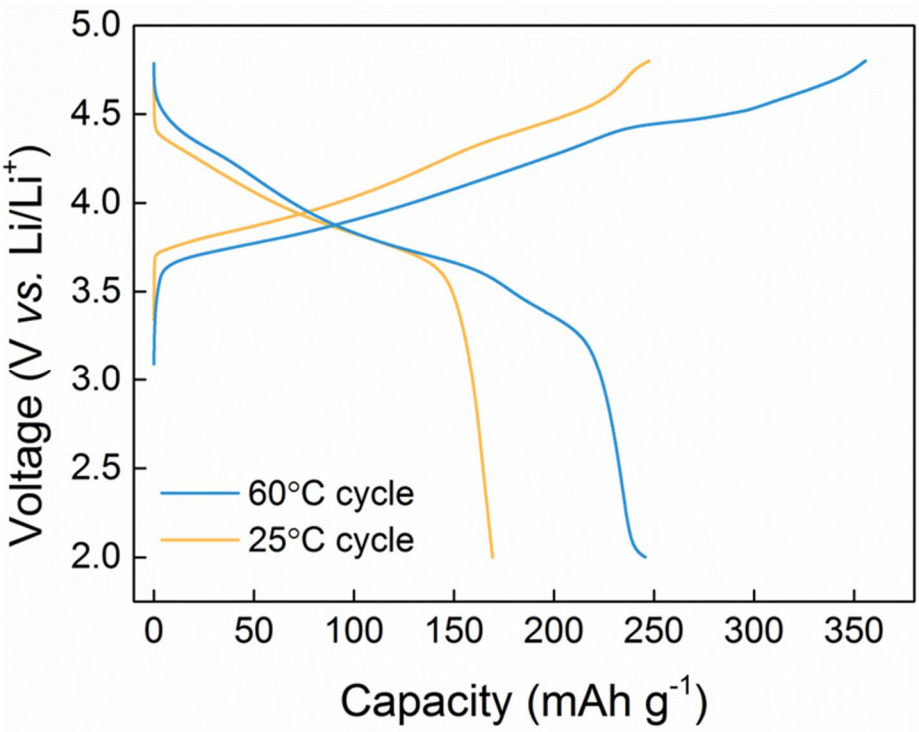

Figure 3.2. The first charge/discharge profile of LNM244 operated at 25 °C and 60 °C are compared. While 1.13 Li is extracted on 60 °C charge, only 0.79 Li is extracted on 25 °C charge. During the first charge of LNM244, Ni is oxidized from 3+ to 4+ and oxygen oxidation accompanies with the rest of Li extraction. However, when I compare Ni XANES peak change during the first charge, Ni is fully oxidized in both temperatures (figure 3.3a,b), which indicates the difference in the first charge capacity originates from the different amount of oxygen oxidation. Therefore, LNM244 is pre-cycled at 60 °C and tested at 25 °C.

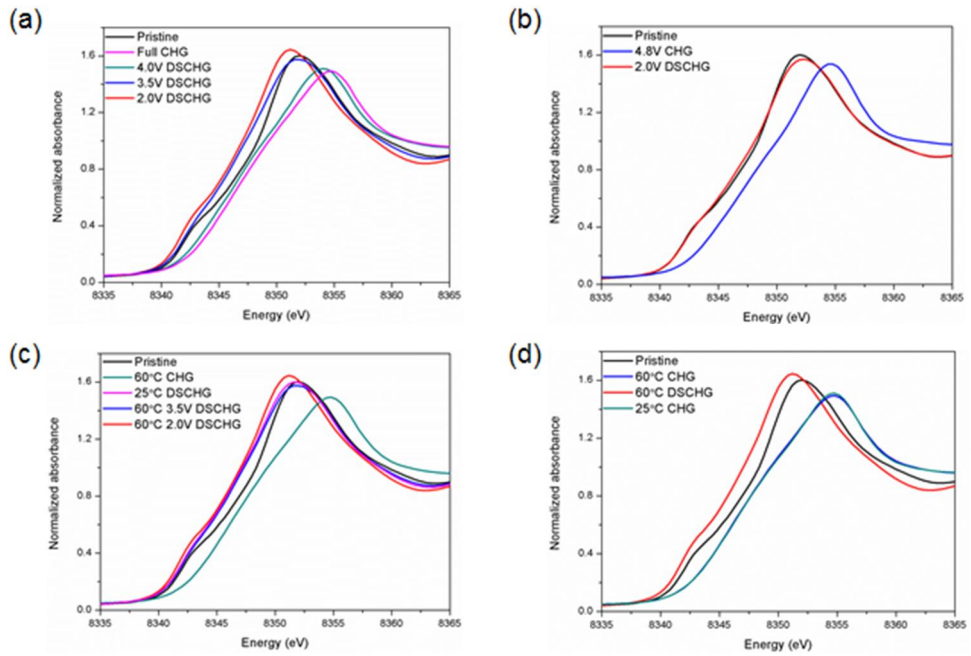

Figure 3.3. Ni XANES spectra of LNM244 (a) LNM244 cycled at 60 °C. (b) LNM244 cycled at 25 °C. Whereas Ni peak shifts at full charged states are almost identical, there is large difference in discharged state between two temperatures. When 2.0 V discharged states are compared, the cell operated at 60 °C is more reduced. (c) 60 °C charged and 25 °C 2.0 V discharged state (pink) is plotted together with the figure 3.3a. It is fitted well with 3.5 V 60 °C discharged state, which indicates that it is not fully discharged yet as shown in figure 3.1a. (d) 60 °C 1 cycled and 25 °C charged state (green) is plotted together with the figure 3.3a. It is fitted well with 60 °C full charged state, which indicates that charge reaction at 25 °C is not inhibited as shown in figure 3.1b.

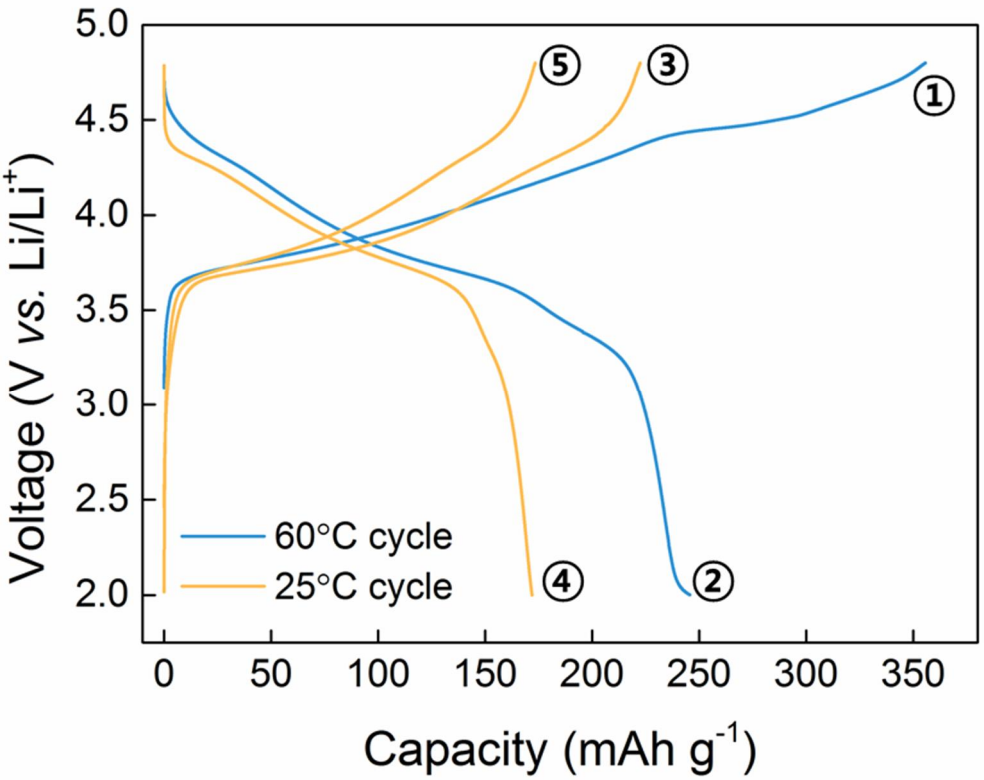

Figure 3.4. Electrochemical profile of LNM244 one cycled at 60 °C, followed by 25 °C charge and discharge.

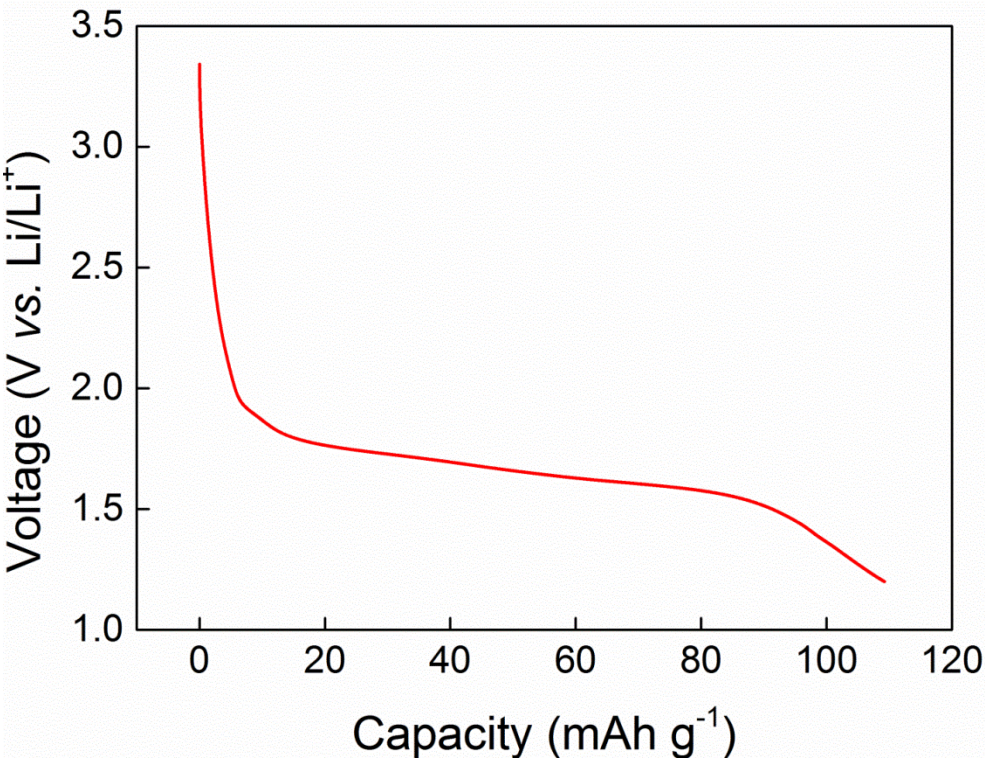

Figure 3.5. Electrochemical profile of LNM244 when it starts with discharge until 1.2 V from the pristine state.

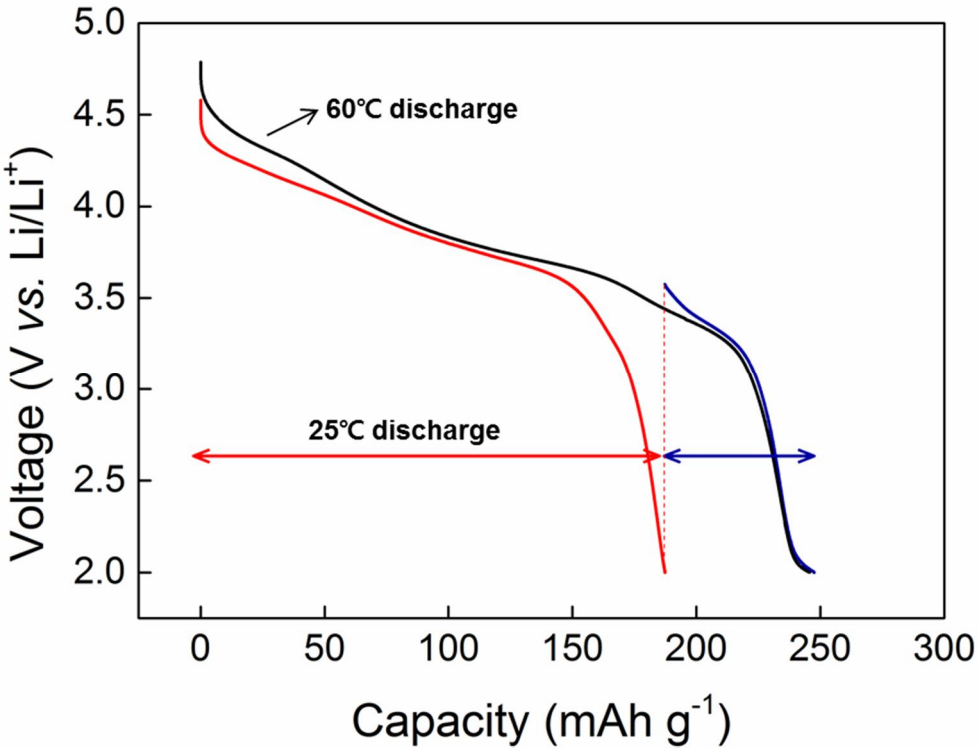

Figure 3.6. 25 °C discharge to 2.0 V (red), followed by transferring to 60 °C oven, rested and discharged (blue). It is compared with normal 60 °C discharge profile (black).

3.3.2. TM migration during cycling

Noteworthy is that the de-intercalation of lithium is moderately faster and almost all the lithium in the structure can be extracted without significant kinetic hindrance at room temperature as demonstrated in Figure 3.1c. The GITT charge profile taken at 25 °C in Figure 3.7 further confirms the absence of the large polarization region in contrast to the GITT discharge profile, and shows that the measured QOCVs basically correspond to the lithium extraction from the octahedral sites. In order to elucidate the apparent difference in the charge and discharge, the structural evolution was probed using scanning transmission electron microscopy-high angle annular dark field (STEM-HAADF) for each charge/discharge protocols in Figure 3.8a-e.[34, 35] The figures illustrate the typical layered frameworks of the LNM244 in general, however the close inspection reveals that the reversible TM migration takes place between TM layer and lithium layer, consistent with the previous observations in other LLOs [10, 18, 22], while detailed TM migration behaviors are distinctively different depending on the charge/discharge protocols. At 60 °C, a significant amount of TM is present in the lithium layer after the charge process, indicative of the TM migrations during de-lithiation as shown in Figure 3.8a; however, the TM migrates back to its initial TM layer during discharge as evidenced from the absence of TM in the lithium layer (Figure 3.8b). Similar trend was also observed in the electrode charged at room temperature with the significant TM migration into lithium layer in Figure 3.8c. Nevertheless, the electrode discharged (~ 2 V) at room temperature in Figure 3.8d

still contained noticeable amount of TM in the lithium layer, which indicates that the TM migration is only partially reversible contrary to the case of Figure 3.8b. On the other hand, interestingly, it was found that, when the electrode is further discharged with 250 mAh g^{-1} capacity undergoing the low-voltage plateau region, the presence of TM in the lithium layer is substantially reduced as presented in Figure 3.8e, suggesting that TMs managed to migrate back to the initial TM layer.

Further confirmation on the distinct TM migration behaviors is provided by XRD and Raman spectroscopy in Figure 3.8f and g. Figure 3.8f displays XRD patterns of the LNM244 electrodes discharged at different conditions, *i.e.* discharged at 60 °C (blue), discharged at 25 °C (green) and discharged with a 250 mAh g^{-1} capacity cutoff at 25 °C (orange). While the overall structure retains the layered frameworks, the electrode discharged at 25 °C presents a clear hump next to (003) peak around 18.5° as shown in the inset of the figure. This higher angle peak is known to be a signature of a spinel-like phase formed in layered materials,[36-38] supporting the presence of migrated TMs in the lithium layer after the discharge at 25 °C. On the other hand, further discharge with a 250 mAh g^{-1} capacity cutoff leads to a symmetric (003) peak identical to the one with 60 °C discharge. This is also consistent with the STEM results that LNM 244 transforms back to its ordered layered structure after the same discharge conditions (Figure 3.8b and e). Raman spectroscopy data in Figure 3.8g also support the aforementioned speculations on TM migration. The characteristic peaks at 484 cm^{-1},

548 cm^{-1} and 602 cm^{-1} are attributed to the E_g and A_{1g} modes of R-3m space group ($LiMO_2$ phase) and the A_g mode of C2/m space group (Li_2MnO_3 phase), respectively. [39-42] When the electrode is charged at 60 °C, the broad hump appears at 650 cm^{-1} indicating the appearance of the spinel-like phase.[9, 43] However, the signature of spinel-like phase at 650 cm^{-1} does not disappear on discharge at 25 °C (green), contrary to the case of the 60 °C discharge or the extended capacity cut discharge at 25 °C, consistent with the XRD and HAADF analyses.

Results on the unique TM migration behaviors in Figure 3.8 propose that they are likely to be linked with the observed kinetic limitations in the discharge process.[10, 12, 44] During the lithium intercalation at 25 °C, only limited amount of TM in the lithium layer migrates back to the TM layer, which results in a lack of vacancies for the lithium intercalation. As a result, it is supposed that the discharge capacity becomes lower even after the full extraction of lithium as presented in Figure 1b. And, the further forcible discharge induces the lithium insertion into the tetrahedral sites accompanying the low-voltage plateau. Note that the TM migration back to the original TM layer was significantly promoted in Figure 3.8e when lithium ions are forcibly intercalated into the tetrahedral site, implying the correlation between tetrahedral lithium occupancy and the TM migration back. It is believed that the lithium in the tetrahedral site strongly repulses the TM in the octahedral site in the lithium layer, triggering the migration of the TM to the TM layer, because of the relatively unstable tetrahedral lithium coordinations and the close distance between TM and the tetrahedral lithium. Once TM migrates, lithium

in the unfavorable tetrahedral sites would hop into the empty octahedral site. This model explains the observations that after the discharge with the low-voltage plateau, the subsequent charging takes place *via* lithium de-intercalation from the octahedral sites not from the tetrahedral sites in Figure 3.1d.

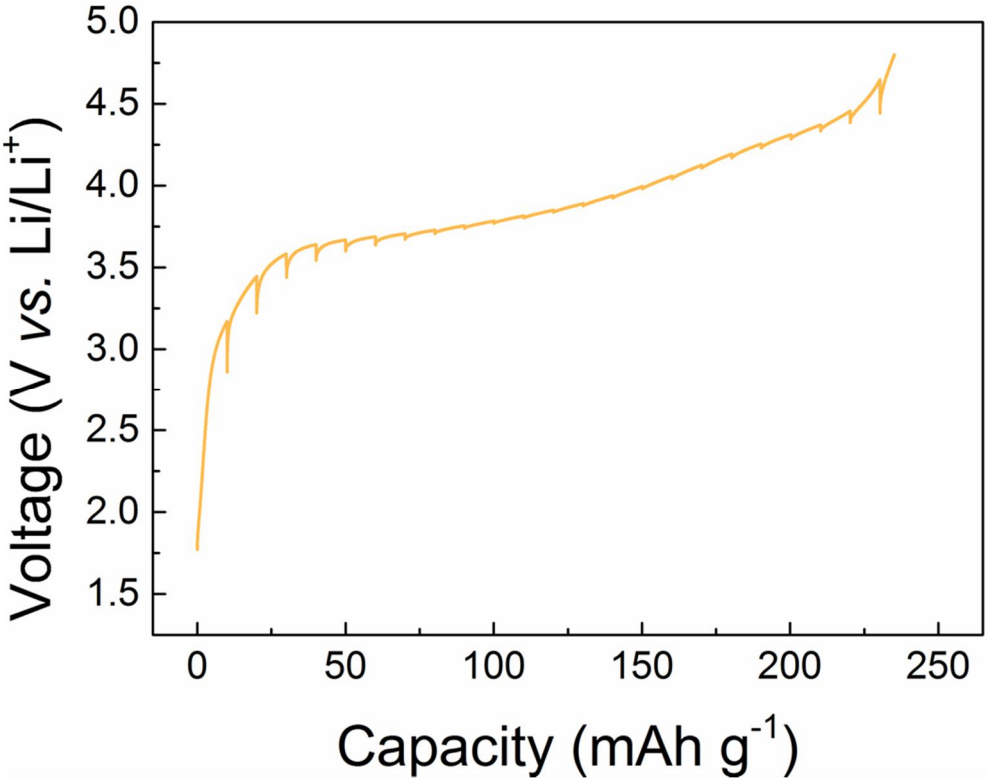

Figure 3.7. GITT on 25 °C charge after 60 °C charge and 25 °C discharge with 250 mAh g^{-1} cutoff.

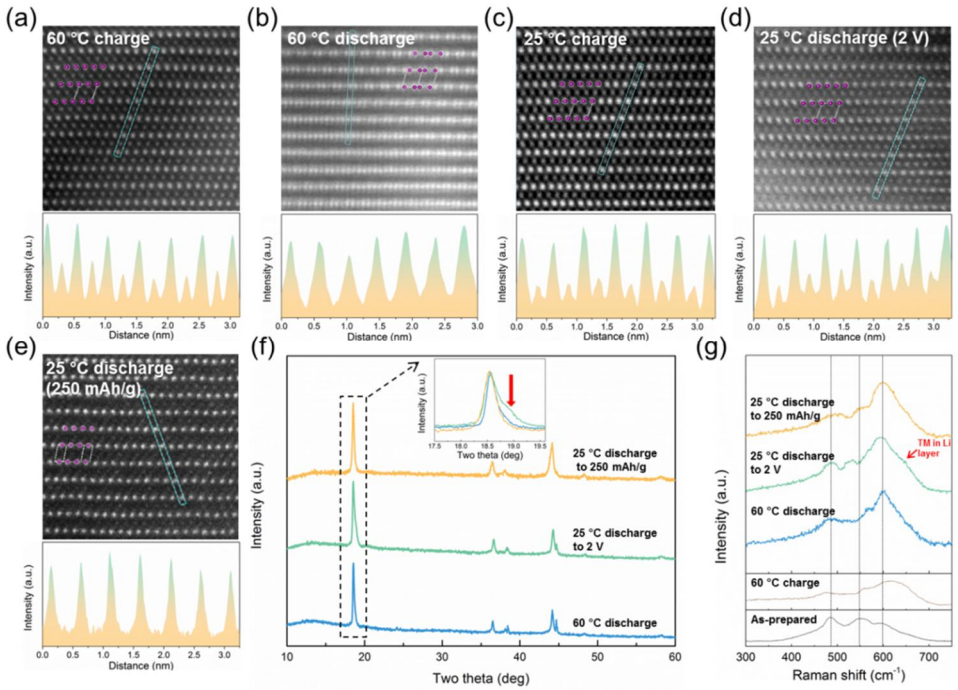

Figure 3.8. Structural characterization of LNM244 discharged at different conditions. STEM-HAADF image and the intensity line profile of boxed region immediately after (a) 60 °C charge, (b) 60 °C discharge, (c) 25 °C charge, (d) 25 °C discharge until 2 V and (e) 25 °C discharge until 250 mAh g^{-1}. Pink spheres denote TMs in C2/m unit cell of Li_2TMO_3. (f) XRD pattern of electrodes with 60 °C discharge (blue), 25 °C discharge to 2 V (green) and 25 °C discharge to 250 mAh g^{-1} (orange). Before discharging, all the electrodes were charged up to 4.8 V at 60 °C. (003) peaks around 18.5° are plotted together in the inset, which shows the hump at the 2 V discharged sample. (g) Raman spectra of pristine (black), 60 °C charge (brown), 60 °C discharge (blue), 25 °C discharge to 2 V (green) and 25 °C

discharge to 250 mAh g^{-1} (orange). Before discharging, all the electrodes were charged up to 4.8 V at 60 °C.

3.3.3. Temperature dependent lithium diffusion behavior

According to our proposed model, the kinetic limitations in the discharge process are attributed to the presence of TMs in the lithium layer that could not migrate back to TM layer due to the insufficient reversibility at low temperature and the corresponding tetrahedral lithium occupancy that accompanies the substantial overpotential. In order to support this, I systematically altered the operating temperature of the electrochemical cell and examined how the charge and discharge behaviors are respectively influenced. Figure 3.9a presents the electrochemical profiles of the cells that have been discharged with a 250 mAh g^{-1} cutoff at respective temperatures from 10 to 60 °C followed by the subsequent charge. It clearly demonstrates that the low-voltage plateau gets significantly longer as the temperature decreases. Based on the capacity from the low-voltage plateau, the amount of lithium occupancy in the tetrahedral sites increases up to as much as ~ 100 mAh g^{-1} of corresponding capacity at 10 °C, which accounts for nearly 40% of the discharge capacity as illustrated in Figure 3.9b. This further confirms that the appearance of the low-voltage plateau is a kinetically induced phenomenon. At such low operating temperatures, the migrated TMs are more likely to be trapped in the lithium layer, triggering the lithium intercalation into the tetrahedral sites. The premature growth of the overpotential in this step leads to the substantial loss of the discharge capacity at > 2V. Nevertheless, when the electrodes are forcibly discharged involving the low-voltage plateau, the subsequent charge profiles are almost unchanged, in contrast to the sensitive

temperature-dependency of the discharge. Moreover, the overall charge capacity is relatively less affected by the temperature as long as the sufficient discharge is performed involving the low-voltage plateau (Figure 3.9c). This asymmetric change in the charge/discharge profile agrees to that the discharge reaction is intrinsically more sluggish, and indicates that the kinetic barriers are substantially relieved after undergoing the forcible discharge, facilitating the charging kinetics. I believe that the facilitated charge process can be also elucidated with the previous TM migration behaviors that indicated the significant reduction of TMs in the lithium layer after the discharge process involving the low-voltage plateau. At the end of the each discharge, the tetrahedral lithium repulses TMs to migrate back to TM layers and moves to the octahedral sites. In the absence of TMs in the lithium layer, the octahedral lithium ions could be extracted rapidly regardless of the temperature. It also suggests that the kinetics of TM migration is sufficiently fast even at low temperatures, once the tetrahedral site occupancies in the structure are prevalently present.

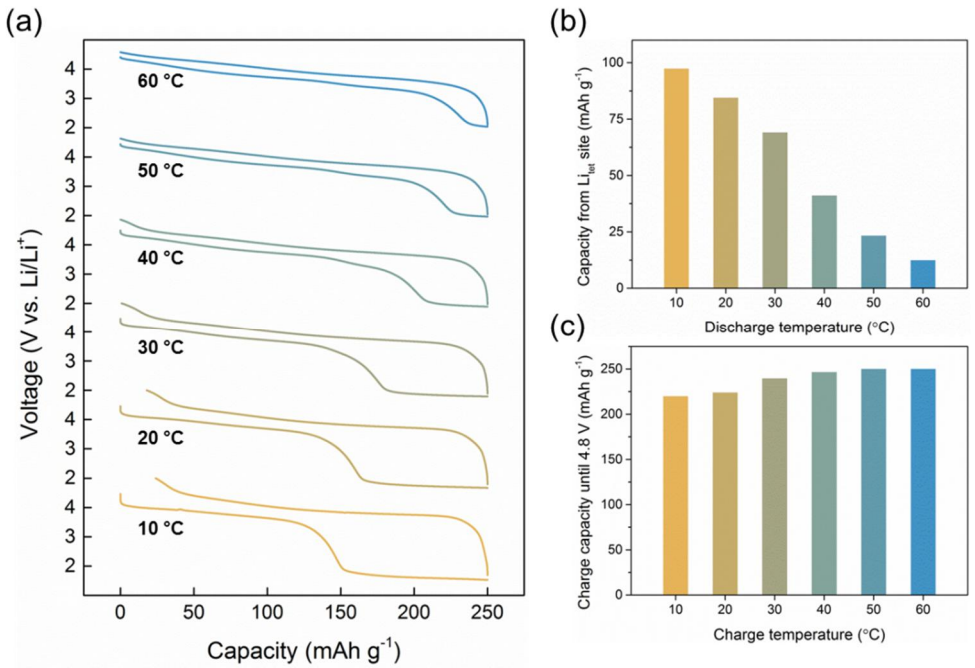

Figure 3.9. Temperature dependent electrochemical profile of LNM244. (a) After 60 °C charge, the cell is discharged and charged at different temperatures from 10 °C to 60 °C. The cell is discharged by capacity cut until 250 mAh g^{-1} and charged by capacity cut until 250 mAh g^{-1} and voltage cut until 5.0 V. (b) Discharge capacity appearing at low voltage plateau calculated from Figure 3.9a. (c) Charge capacity delivered until 4.8 V from Figure 3.9a.

3.3.4. New model for lithium diffusion behavior

Based on our findings, the behavior of TM migration and its correlation with lithium diffusion would be important to understand the dissimilar response of the charge and discharge reactions. However, one may wonder why the observed TM migrations have less impact on the charge process kinetics than the discharge. This would naturally lead to a question regarding the TM migration mechanism/kinetics during charge (from TM to lithium layers) and during discharge (from lithium to TM layers). When I compare the local environments in which TM migration occurs, there may arise differences depending on the migration directions (either toward lithium layer or TM layer) and the number of subsequent possible atomic migration sites (Figure 3.10). On charge, TM migration to lithium layer takes place primarily *via* the path which involves hopping through the intermediate tetrahedral site (black dotted line) in the lithium layer as shown in Figure 3.10a. It is noted that the occupancy of TM in the tetrahedral sites is readily available but only energetically favorable when the three lithium octahedral sites neighboring the tetrahedral sites are completely vacated, which implies that the TM migrations are expected to occur at relatively high de-lithiated states.[45] Importantly, further migrations of TM in the lithium layer may also occur occupying the octahedral sites in the lithium layer, which would be induced by the thermal vibration (Figure 3.10a). The migrations of TMs to the octahedral sites in the lithium layer have been often observed in layered transition metal oxides,[10, 11, 18] and are believed to be more feasible in LLO type of materials, where TM would

suffer less electrostatic repulsion with the lithium (or vacancy after de-lithiation) in TM layer during hopping. Nevertheless, it is expected that the hopping of TM within the lithium layer would occur only preferably in the absence of the lithium in the lithium layer, thus, its effect on the lithium mobility would be rather limited at the end of the charge process.[23, 46] During discharge, on the other hand, TM migrations can be much more complex especially when considering the reversible TM migration back to TM layer. When the TM has traveled far from the original site after the charge (Figure 3.10b), there can be long migration paths for TM to wander back to TM layer from lithium layer. TM should find its way to the initial tetrahedral site located just above the empty TM octahedral site to reversibly move back to TM layer, as it is depicted by the blue arrow. However, any incidental hopping to other sites beside the path depicted with blue arrows would further delay the TM migration back to the lithium layer. These unnecessary and additional migrations of TM inside the lithium layer significantly increase the TM "migration length" toward the specific tetrahedral site, which is the essential site for the reversible TM migration back to the TM layer on discharge. It is also feasible that, when the lithium ions are being inserted, they would electrostatically interact with the TM and repulse TM far away from the original position, thus the migration path of TM can become even longer. The prolonged presence of TM in the lithium layer during discharge would more significantly retard the lithium insertion kinetics. Extended migration length and distracted migration path particularly occurring

during discharge contribute to the asymmetric behavior in TM migration between charge and discharge.

It has been traditionally believed that the guest ion diffusion takes place identically for both insertion and extraction in the intercalation hosts. And, it was because the intercalation host was supposed to be mainly unaltered with the insertion and extraction of the guest ions. The change of the intercalation host, if any, was also regarded to be symmetric with the insertion and the extraction, only following the energetically favorable structures at each guest ion concentrations. However, our findings on the asymmetric TM migrations and the correlated lithium and TM motion cast a doubt in the traditional lithium diffusion model. The non-equivalent host structures, which are distinguished respectively in the insertion and extraction process, offer the different environments for the guest ion diffusion (Figure 3.10c). As demonstrated here, in the layered lithium TM oxides, the extraction of lithium is accompanied by the migration of TM into the lithium layer, which only marginally alters the lithium diffusion kinetics. However, when the spontaneous further migration of TM is allowed in the lithium layer afterward, the lithium re-insertion is significantly retarded due to the difficulty of TM migration back to TM layer. Additional lithiation involving the kinetically induced tetrahedral lithium occupancy facilitate the motion of TM aiding in finding its way to the TM layer, which recovers the original layered structure. In this diffusion model, lithium is not the sole mobile ion in the intercalation host, but its motion is correlated with the motion of TM that constitutes the intercalation host. I confirm that similar

asymmetric kinetic behavior can be observed from other LLO materials (Figure 3.11), which indicates that the proposed new lithium diffusion model can be widely accepted from various LLO materials.

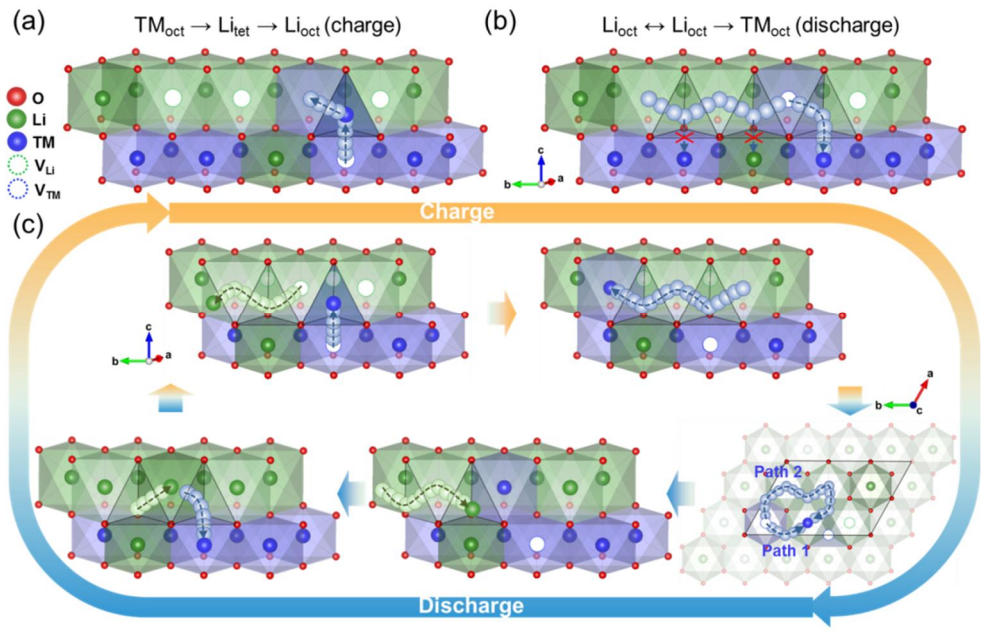

Figure 3.10. Schematic illustration of local environment on TM migration. (a) TM migration from TM layer to lithium layer on charge through tetrahedral site of lithium (Li_{tet}). (b) TM migration between lithium octahedral sites (Li_{oct}) inside the lithium layer on discharge. Migrated TM can also migrate to other Li_{oct} site, which elongates the distance from initial TM_{oct}. (c) Proposed lithium diffusion model for the correlative motion with TM migration.

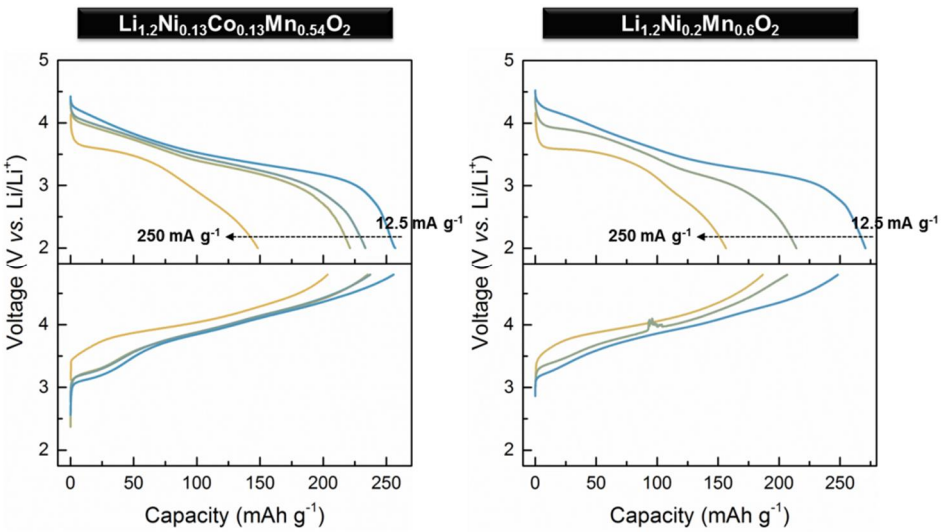

Figure 3.11. Asymmetric kinetic behavior for other LLO material. Electrochemical profiles of discharge and charge at 25 °C from various C-rates after respective pre-cycle at 60 °C for $Li_{1.2}Ni_{0.13}Co_{0.13}Mn_{0.54}O_2$ and $Li_{1.2}Ni_{0.2}Mn_{0.6}O_2$.

3.4 Concluding Remarks

In summary, I reported here for the first time that intercalation and de-intercalation kinetics in layered lithium TM oxides electrodes could be inherently non-equivalent, exhibiting respectively distinct lithium diffusion mechanisms, and proposed a new lithium diffusion and intercalation model. It was presented that the lithium diffusion is much more sluggish during the lithiation than the de-lithiation, which could not be elucidated based on the classical lithium diffusion model within a rigid layered framework. From the series of electrochemical and structural analyses, it was illustrated that it originates from the asymmetric TM migrations during charge and discharge, which offers non-equivalent local environments for lithium diffusion. I proposed that TM migrates to lithium layer during de-intercalation of lithium, which are subsequently followed by the random hoppings of TM in the lithium layer. In the ideal intercalation reaction, those TMs should find their way to TM layer precisely following the reverse path, thus the lithium intercalation is symmetric to the de-intercalation. However, in practice, due to the randomness of TM hoppings and the difficulty of TM in finding the original vacancy in TM layer to migrate back, the presence of TM is far extended in the lithium layer, redundantly retarding the lithium diffusion particularly during lithiation process. The extended and distracted migration of TMs in the lithium layer make the reversible TM migration toward TM layer get sluggish. Moreover, it was found that the formation of energetically unfavorable tetrahedral lithium occupancy expedites the TM migration and aids in recovering the original layered

framework, thus facilitating the lithium diffusion afterwards. Our new lithium diffusion model explicates the non-equivalent intercalation and de-intercalation kinetics in the layered structure and reveals the importance of considering the correlative motion between lithium and TM in the structure in understanding this class of materials. It also suggests that the control of TM migration reversibility during charge/discharge can be an effective way of designing new LLO materials.

3.5. References

[1] M. Armand, J. M. Tarascon, *Nature* **2008**, 451, 652.

[2] M. S. Whittingham, *Chem. Rev.* **2004**, 104, 4271.

[3] K. Kang, Y. S. Meng, J. Bréger, C. P. Grey, G. Ceder, *Science* **2006**, 311, 977.

[4] T. Ohzuku, A. Ueda, *Journal of The Electrochemical Society* **1994**, 141, 2972.

[5] O. Tsutomu, M. Yoshinari, *Chemistry Letters* **2001**, 30, 642.

[6] J. Hong, H. Gwon, S.-K. Jung, K. Ku, K. Kang, *J. Electrochem. Soc.* **2015**, 162, A2447.

[7] S.-K. Jung, K. Kang, *Nat. Energy* **2017**, 2, 912.

[8] M. M. Thackeray, S.-H. Kang, C. S. Johnson, J. T. Vaughey, R. Benedek, S. A. Hackney, *J. Mater. Chem.* **2007**, 17, 3112.

[9] J. Hong, D.-H. Seo, S.-W. Kim, H. Gwon, S.-T. Oh, K. Kang, *J. Mater. Chem.* **2010**, 20, 10179.

[10] M. Sathiya, A. M. Abakumov, D. Foix, G. Rousse, K. Ramesha, M. Saubanère, M. L. Doublet, H. Vezin, C. P. Laisa, A. S. Prakash, D. Gonbeau, G. VanTendeloo, J. M. Tarascon, *Nat. Mater.* **2015**, 14, 230.

[11] B. Xu, C. R. Fell, M. Chi, Y. S. Meng, *Energy Environ. Sci.* **2011**, 4, 2223.

[12] E. McCalla, A. M. Abakumov, M. Saubanère, D. Foix, E. J. Berg, G. Rousse, M.-L. Doublet, D. Gonbeau, P. Novák, G. Van Tendeloo, R. Dominko, J.-M. Tarascon, *Science* **2015**, 350, 1516.

[13] D.-H. Seo, J. Lee, A. Urban, R. Malik, S. Kang, G. Ceder, *Nature Chem.* **2016**, 8, 692.

[14] K. Luo, M. R. Roberts, R. Hao, N. Guerrini, D. M. Pickup, Y.-S. Liu, K. Edström, J. Guo, A. V. Chadwick, L. C. Duda, P. G. Bruce, *Nat Chem* **2016**, 8, 684.

[15] M. Sathiya, G. Rousse, K. Ramesha, C. P. Laisa, H. Vezin, M. T. Sougrati, M. L. Doublet, D. Foix, D. Gonbeau, W. Walker, A. S. Prakash, M. Ben Hassine, L. Dupont, J. M. Tarascon, *Nat. Mater.* **2013**, 12, 827.

[16] M. Saubanere, E. McCalla, J. M. Tarascon, M. L. Doublet, *Energy Environ. Sci.* **2016**, 9, 984.

[17] U. Maitra, R. A. House, J. W. Somerville, N. Tapia-Ruiz, J. G. Lozano, N. Guerrini, R. Hao, K. Luo, L. Jin, M. A. Pérez-Osorio, F. Massel, D. M. Pickup, S. Ramos, X. Lu, D. E. McNally, A. V. Chadwick, F. Giustino, T. Schmitt, L. C. Duda, M. R. Roberts, P. G. Bruce, *Nature Chem.* **2018**, 10, 288.

[18] W. E. Gent, K. Lim, Y. Liang, Q. Li, T. Barnes, S.-J. Ahn, K. H. Stone, M. McIntire, J. Hong, J. H. Song, Y. Li, A. Mehta, S. Ermon, T. Tyliszczak, D. Kilcoyne, D. Vine, J.-H. Park, S.-K. Doo, M. F. Toney, W. Yang, D. Prendergast, W. C. Chueh, *Nat. Commun.* **2017**, 8, 2091.

[19] A. Grimaud, W. T. Hong, Y. Shao-Horn, J. M. Tarascon, *Nat. Mater.* **2016**, 15, 121.

[20] C. Zhan, Z. Yao, J. Lu, L. Ma, V. A. Maroni, L. Li, E. Lee, E. E. Alp, T. Wu, J. Wen, Y. Ren, C. Johnson, M. M. Thackeray, M. K. Y. Chan, C. Wolverton, K. Amine, *Nat. Energy* **2017**, 2, 963.

[21] A. J. Perez, Q. Jacquet, D. Batuk, A. Iadecola, M. Saubanère, G. Rousse, D. Larcher, H. Vezin, M.-L. Doublet, J.-M. Tarascon, *Nat. Energy* **2017**, 2, 954.

[22] C. R. Fell, D. Qian, K. J. Carroll, M. Chi, J. L. Jones, Y. S. Meng, *Chem. Mater.* **2013**, 25, 1621.

[23] J. Reed, G. Ceder, *Chem. Rev.* **2004**, 104, 4513.

[24] D. Mohanty, B. Mazumder, A. Devaraj, A. S. Sefat, A. Huq, L. A. David, E. A. Payzant, J. Li, D. L. Wood, C. Daniel, *Nano Energy* **2017**, 36, 76.

[25] K. Kang, G. Ceder, *Phys. Rev. B* **2006**, 74, 094105.

[26] A. Van der Ven, G. Ceder, *Electrochem. Solid-State Lett.* **2000**, 3, 301.

[27] C. Delmas, J. P. Pérès, A. Rougier, A. Demourgues, F. Weill, A. Chadwick, M. Broussely, F. Perton, P. Biensan, P. Willmann, *J. Power Sources* **1997**, 68, 120.

[28] A. Rougier, P. Gravereau, C. Delmas, *J. Electrochem. Soc.* **1996**, 143, 1168.

[29] T. Ohzuku, A. Ueda, M. Nagayama, *J. Electrochem. Soc.* **1993**, 140, 1862.

[30] V. F. Sears, *Neutron News* **1992**, 3, 26.

[31] C. S. Johnson, J.-S. Kim, A. Jeremy Kropf, A. J. Kahaian, J. T. Vaughey, M. M. Thackeray, *Electrochem. Commun.* **2002**, 4, 492.

[32] R. Benedek, J. Vaughey, M. M. Thackeray, *Chem. Mater.* **2006**, 18, 1296.

[33] S.-H. Kang, S.-H. Park, C. S. Johnson, K. Amine, *J. Electrochem. Soc.* **2007**, 154, A268.

[34] Y. Wang, Z. Yang, Y. Qian, L. Gu, H. Zhou, *Advanced Materials* **2015**,

27, 3915.

[35] C. Genevois, H. Koga, L. Croguennec, M. Ménétrier, C. Delmas, F. Weill, *The Journal of Physical Chemistry C* **2015**, 119, 75.

[36] B. Song, H. Liu, Z. Liu, P. Xiao, M. O. Lai, L. Lu, *Scientific Reports* **2013**, 3, 3094.

[37] X. Feng, Z. Yang, D. Tang, Q. Kong, L. Gu, Z. Wang, L. Chen, *Physical Chemistry Chemical Physics* **2015**, 17, 1257.

[38] Y.-P. Deng, F. Fu, Z.-G. Wu, Z.-W. Yin, T. Zhang, J.-T. Li, L. Huang, S.-G. Sun, *Journal of Materials Chemistry A* **2016**, 4, 257.

[39] C. Julien, *Solid State Ionics* **2000**, 136–137, 887.

[40] C. M. Julien, M. Massot, *Materials Science and Engineering: B* **2003**, 100, 69.

[41] D. Y. W. Yu, K. Yanagida, *J. Electrochem. Soc.* **2011**, 158, A1015.

[42] C. Ghanty, B. Markovsky, E. M. Erickson, M. Talianker, O. Haik, Y. Tal-Yossef, A. Mor, D. Aurbach, J. Lampert, A. Volkov, J.-Y. Shin, A. Garsuch, F. F. Chesneau, C. Erk, *ChemElectroChem* **2015**, 2, 1479.

[43] S. Hy, W.-N. Su, J.-M. Chen, B.-J. Hwang, *J. Phys. Chem. C* **2012**, 116, 25242.

[44] J. Lee, A. Urban, X. Li, D. Su, G. Hautier, G. Ceder, *Science* **2014**, 343, 519.

[45] J.-M. Lim, D. Kim, Y.-G. Lim, M.-S. Park, Y.-J. Kim, M. Cho, K. Cho, *J. Mater. Chem. A* **2015**, 3, 7066.

[46] J. Reed, G. Ceder, A. Van Der Ven *Electrochem. Solid-State Lett.* **2001**, 4, A78.

Chapter 4. Thermal driven memory effect in lithium ion battery

4.1. Research background

As one of the efficient and environmental friendly ways of using energy, the demand for the electric vehicles (EV) is rapidly growing worldwide.[1, 2] For EVs, the lithium ion battery (LIB) is the key technology, which determines mileage, price and changes internal components of vehicles, to succeed in replacing the existing gasoline based vehicles.[3] Basically, the LIB in EVs aims to maximize the mileage and embed fast chargeability by using active materials with high power and energy densities, which are also commonly considered as the most necessary properties from other applications using LIB. However, compared with other applications such as laptop or smart phone, EVs are more likely to be exposed to harsh and extreme conditions during parking or driving, which is susceptible to the external conditions.[4-6] Therefore, among several other properties of battery electrode materials that have not been taken into account seriously, some of them require more critical consideration especially for EV applications.

Temperature is a crucial factor that affects battery performance during both operating and storage.[7-13] The LIB for EVs require feasibility over a wide temperature range, where the temperature range inside the car goes over 60 °C in summer and below 0 °C in winter.[4, 6] There have been studies on the effect of

temperature on cathode materials, mostly about the degradation effect at high temperature. The layered materials in charged state release oxygen and suffer from the phase transformation from around 200 °C,[10, 13] while the formation of resistive surface film during the long term storage at around 60 °C deteriorates cell performances.[7, 11, 12, 14] Moreover, Mn dissolution in $LiMn_2O_4$ is accelerated at high temperature (60 °C), leading to the severe capacity fading.[8, 9] Therefore, given the disadvantageous effect of temperature on cathode materials, a better understanding of the temperature effects on the cathode material would provide an opportunity to develop advanced LIBs for EVs.

Of the various cathode candidate materials, high Ni $LiNi_xCo_yMn_zO_2$ (NCM) materials are considered to be the most promising materials for EVs.[15, 16] In case of the post LIB systems such as lithium-air or lithium-rich layered materials, since they require various changes in the operating systems and still have lots of remaining challenges, they are not likely to be realized in the near future from the practical point of view.[17-19] On the other hand, conventional cathode materials also have limitations to be used in EVs; for example, limited usable Li contents and cost problem of $LiCoO_2$ or low energy density and poor conductivity of $LiFePO_4$.[17, 20, 21] Therefore, recent interests have focused on the high Ni NCM materials, exhibiting high energy density with high electronic conductivity. In NCM based materials, as Ni contents increase, both reversible capacity and conductivity increase, which would satisfy the requirements as cathode materials for EVs.[22] However, despite the importance of understanding the effect of temperature, most

studies report investigations or troubleshooting on the problems in high Ni NCM, such as particle crack or transition metal (TM) migration, while studies on the effect of temperature in these materials have been rarely made.[23-27]

In this work, I investigate the effect on the high temperature storage of $LiNi_{0.8}Co_{0.1}Mn_{0.1}O_2$ (NCM811), which is one of the promising high Ni NCM materials for EVs. From the high temperature storage experiments using NCM811, I have discovered interesting phenomenon, thermal driven memory effect of NCMA811. I find out that it memorizes state of charge (SOC) during the high temperature storage and additional polarization appears during the discharge after storage. LIB has been known to have no memory effect and there is one previous report discovering the memory effect on LIB from LFP,[28] where the phenomenon was explained as the delayed overshooting from the non-uniform Li concentration of LFP particles, and later complemented from other works.[29-32] While the memory effect in LFP is attributed to the inhomogeneous lithium concentration between particles, the origin and phenomenon on the thermal driven memory effect in NCM811 observed here are far different from the case of LFP. In this manuscript, I have explored what happens in NCM811 electrodes after high temperature storage and what leads to the memory effect. After high temperature (60 °C) storage of NCM811 for weeks at various SOCs, I find out that the cell memorizes the SOC during storage and discharge voltage profile is dropped proportional to the SOC. I unambiguously confirm that the voltage drop is the additional polarization induced by the formation of stacking faulted region in the particle during the high

temperature storage. While the voltage drop after storage attributes to the reduction in the reversible capacity retention, I reveal that the capacity retention can be recovered some extent by the control of discharge conditions. Based on our findings, I propose the detail mechanism on the thermal driven memory effect, suggesting the importance of critical consideration on the effect of temperature on active materials.

4.2. Experimental Methods

4.2.1. Electrochemical measurements

$LiNi_{0.8}Co_{0.1}Mn_{0.1}O_2$ coin-type half cells were provided from LG chemistry. The galvanostatic charging/discharging process was performed at 25 °C under C/5 rate in the voltage range of 2.5−4.2 V using a potentio-galvanostat (WonA Tech, WBCS 3000, Korea). High temperature storage cells are stored in 60 °C oven after SOC setting.

4.2.2. Characterization of materials

Scanning transmission electron microscopy (STEM) measurements were performed using a cold-field-emission-type Cs-corrected JEM-ARM200F equipped with an electron energy loss spectroscopy (EELS) detector (965 GIF Quantum ER) at Seoul National University, which is operated at 80 kV. Soft X-ray ptychographic microscopy measurements were performed on NCM811 electrode at the bending magnet beamline (5.3.2.1) at the Advanced Light Source (ALS), Lawrence Berkeley National Laboratory, Berkeley, CA (USA). ^{7}Li MAS NMR spectra were recorded at 2.35 T using a Bruker Avance 300 solid state spectrometer with 30 kHz spinning frequency for NMR spectroscopy. High-resolution powder XRD data of the electrodes for Williamson-Hall plot were obtained from beamline 9B at Pohang Accelerator Laboratory (PAL), Republic of Korea. The data were collected over a 2θ range of 10^o – 130^o with a step size of 0.02^o, and wavelength of λ = 1.51830 Å.

4.3. Results and Discussions

4.3.1. Thermal driven memory effect in NCM811

I observed unpredictable behavior of NMC811 after the high temperature storage that the electrode memorizes SOCs of the cell during storage. After 2 pre-cycle of NCM811, the SOCs of the cell are set as 25, 50 and 75 % during the third discharge reaction at 0.5C rate (Figure 4.1), then the coin cells are transferred to 60 °C oven and stored for 3 weeks. The high temperature stored coin cells are again transferred to 25 °C oven and charge/discharged. Figure 4.2a-c present the electrochemical profile after storage at different SOCs and there are clear voltage drops during the first discharge compared to the second discharge, where the capacity of voltage dropped region is exactly same with the SOC of the cell during the storage. This memory effect, which memorizes the SOC of the cell during the storage and reduces the cell voltage, appears only during the first discharge after storage and disappears from the second discharge cycles. However, repeated SOC 50% setting and storage induce reappearance of memory effect of the cell again, where the voltage drop occurs at the first discharge and disappears from the second discharge reaction after storage repeatedly. (Figure 4.3a, b) Although the voltage drop disappears from the second cycle after storage, repeated SOC setting and storage result in the same memory effect, demonstrating that the memory effect is the repeatable phenomenon with high temperature storage.

Factors affecting the memory effect are further explored to understand the origin of this phenomenon. I firstly controlled the duration of high temperature

storage, which is found to intensify the memory effect. When NCM811 is stored at SOC 50% for 1 to 4 weeks, the degree and region of voltage drop increase with storage time (Figure 4.2b,d,e and 4.3a). At the one week stored sample in Figure 4.2d, in addition to the less clear voltage drop, the voltage drop is started not from the SOC 50% but from more discharged point, which indicates SOC is not sufficiently memorized during the one week storage. After the one more week storage (Figure 4.2e), it exhibits more clear voltage drop starting from near SOC 50% point. Moreover, at the four weeks stored sample, the degree of voltage drop is most severe, whereas the starting point of voltage drop is saturated at SOC 50% point and is not elongated anymore even longer storage duration. Resultant capacity retention also decreases from 98.8% after the one week storage to 95.5% after the four weeks storage due to more severe voltage drop implying that the memory effect is getting intensified with the duration of high temperature storage. In addition, the memory effect is also affected by the C-rate of the cell. When all procedures for the one month storage were identical except for the different C-rate at 1C and 0.1C, it exhibited a larger voltage drop at 1C rate cell, while a relatively smaller voltage drop was observed at 0.1C rate cell (Figure 4.2f,g). The decrease in the capacity retention was also severe at the 1C rate cell as 88.3%, compared to the 0.1C cell as 97.5%. The C-rate dependency of memory effect indicates that the voltage drop is a kinetically induced phenomenon, which will be discussed in detail later.

According to the electrochemical results, there must be close relationship

between the voltage drop and lithium vacancies during the storage, because the voltage drop is proportional to the SOC of high temperature storage. To verify their relations, the stored cell is only partially cycled before SOC 50%, where the voltage drop starts to appear (Figure 4.3c). After the high temperature storage at SOC 50%, only the amount of lithium that remained in the active material during the storage was charged and discharged for 10 cycles. Figure 4.3c shows that electrochemical profiles for 10 cycles are all overlapped without any voltage drop, whereas clear voltage drop appears at the full discharge until 2.5 V after partial 10 cycles. It implies that voltage drop does not appear at all during the intercalation and deintercalation of lithium that remained in the active material during the storage, while the voltage drop arises only when lithium is intercalated more than the lithium that remained in the active material during the storage. Therefore, for the further understanding on voltage dropped region, I observed the electrochemical profile change by increasing the discharge capacity from 100 mAh g^{-1} to 180 mAh g^{-1} by 20 mAh g^{-1} after high temperature storage at SOC 50% and full charge (Figure 4.3d, e). During the first discharge until 100 mAh g^{-1}, it exhibits voltage drop at the end of the discharge right after passing SOC 50% point. During the following discharge until 120 mAh g^{-1}, voltage drop appears also at the end of the discharge but after passing 100 mAh g^{-1}. Same results were obtained after the subsequent discharge profiles, where voltage drop appears only after passing discharge capacity of the previous cycle, which can be clearly identified in Figure 4.3e. These results demonstrate that the voltage drop does not occur through the

deintercalation/intercalation of lithium contained in the material during the storage, while the voltage drop can be found when lithium is intercalated into the lithium vacant sites, which were empty during the storage. Moreover, once lithium is intercalated into the site with reduced working voltage, that site is somewhat recovered and does not contribute to the voltage drop anymore at the subsequent cycles.

I found out that the voltage drop is attributed to the additional polarization, where the SOC during the storage determines the voltage dropped capacity. Galvanostatic intermittent titration technique (GITT) was measured after the storage at SOC 50% and the measurements began both from charge and discharge respectively (Figure 4.4a,b). Figure 4.4a shows that the voltage drop starts to appear after discharge SOC 50% region and additional polarization is applied at the voltage dropped region, which clearly memorizes the SOC during the storage. The additional polarization also arises when GITT is measured starting from the discharge, while the additional polarization does not appear at the second cycle (Figure 4.4b), which is consistent with the results from Figure 4.2b and 4.3d. Identical results are also obtained from EIS measurements (Figure 4.4c,d). After the high temperature storage at SOC 50%, while it shows low total impedance value less than 10 ohm during charge and half discharge, sudden increase in the impedance can be found at the later discharge after SOC50. GITT and EIS results indicate that the voltage drop, which is found from the memory effect, is the kinetically induced phenomena and it is applied only when lithium is intercalated

into the lithium vacant site, which was vacant during the storage. Also, the additional polarization is removed once lithium is intercalated into the polarization inducing vacant site, where it was vacant during the high temperature storage.

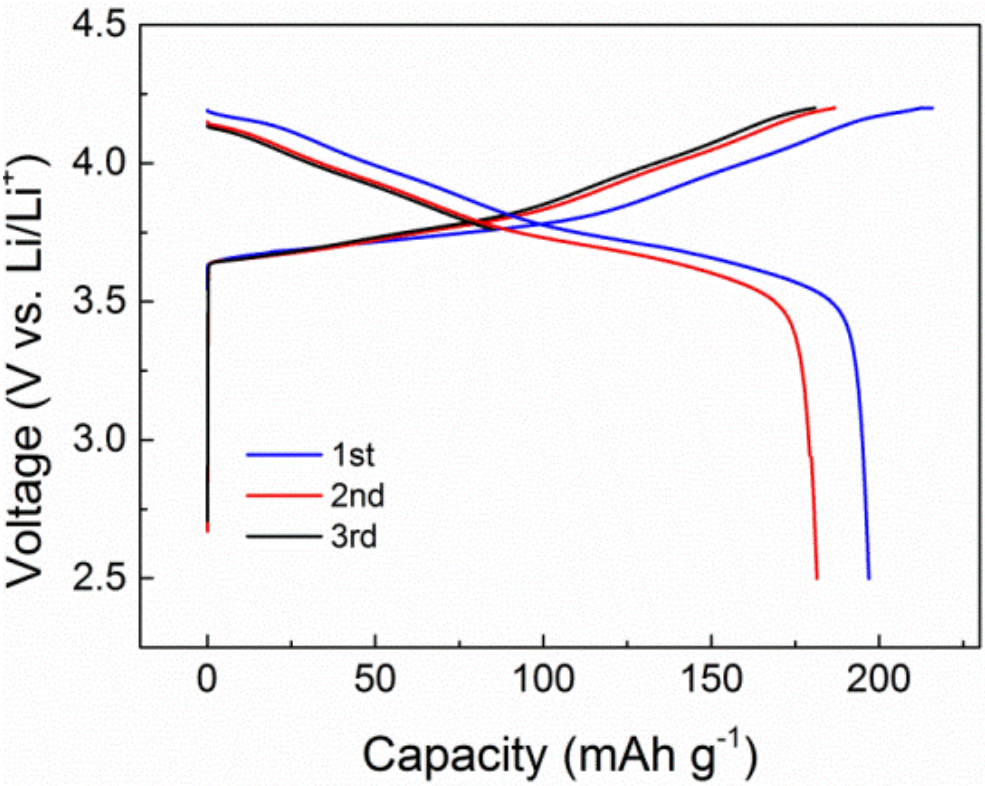

Figure 4.1. Electrochemical profiles for SOC setting. The cell was tested in the voltage range 2.5 – 4.2 V at C/10 during the first cycle and C/5 for the rest of the cycles. SOC of the cell was set at the third discharge cycle.

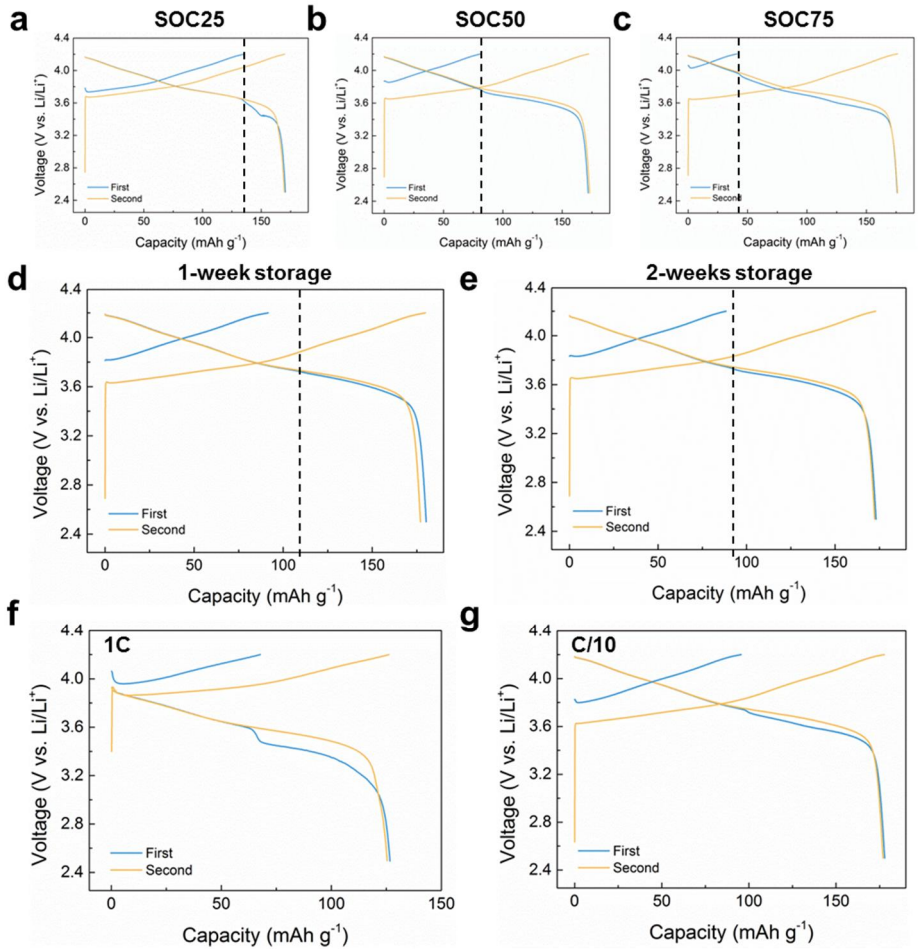

Figure 4.2. Electrochemical profiles on the thermal driven memory effect in NCM811. a-c, 3-weeks storage cells at different SOCs. a, SOC 25%. b, SOC 50%. c, SOC75%. d,e, Effect of storage period on the memory effect; 1-week (d), 2-weeks (e) stored cells at SOC 50%. f,g, Rate dependent behavior of the memory effect, cycled in 1C (f) and C/10 (g) rate after storage at SOC 50%.

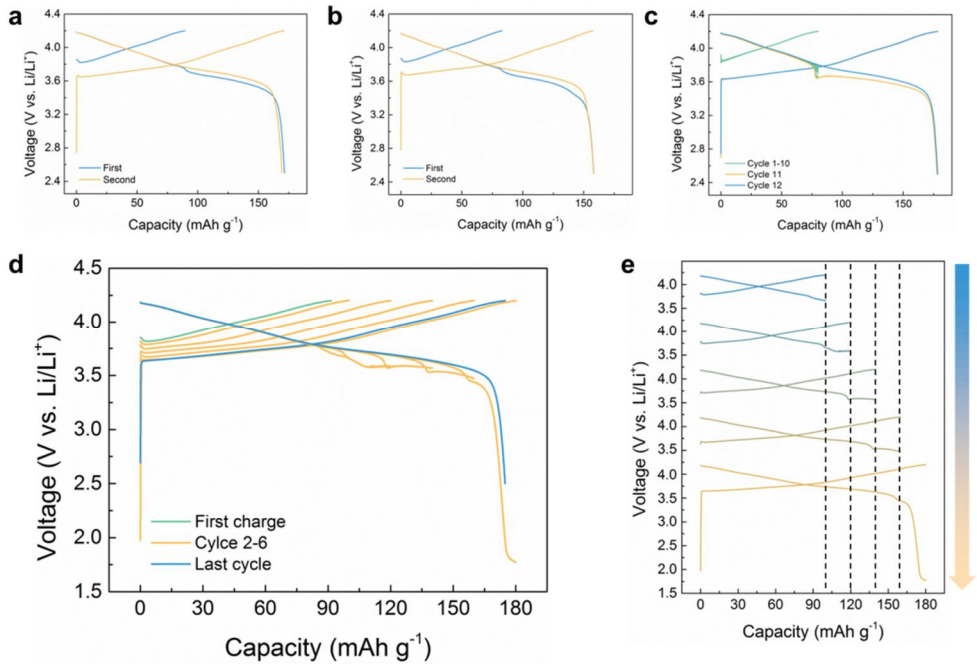

Figure 4.3. Electrochemical profiles on the thermal driven memory effect. a,b, After one month high temperature storage at SOC 50%, clear voltage drop appears after passing SOC 50% during discharge (a). After full discharge (memory release), the cell is set to SOC 50% and stored in high temperature again for one month. The same memory effect behavior reappears after second one month storage (b), demonstrating that the thermal driven memory effect is repeatable phenomenon. c, After high temperature storage at SOC 50%, the cell is cycled until SOC 50% for 10 cycles (green), and then, full discharged at the rest of cycles. While the voltage drop does not appear during the initial 10 cycles discharging until SOC 50%, it appears during the full discharge cycle. d, e, After high temperature storage at SOC 50%, the cell is cycled by increasing discharge capacity from 100 mAh g^{-1} to 180

mAh g^{-1} by 20 mAh g^{-1}. The voltage drop appears only after discharging more capacity than previous discharge capacity

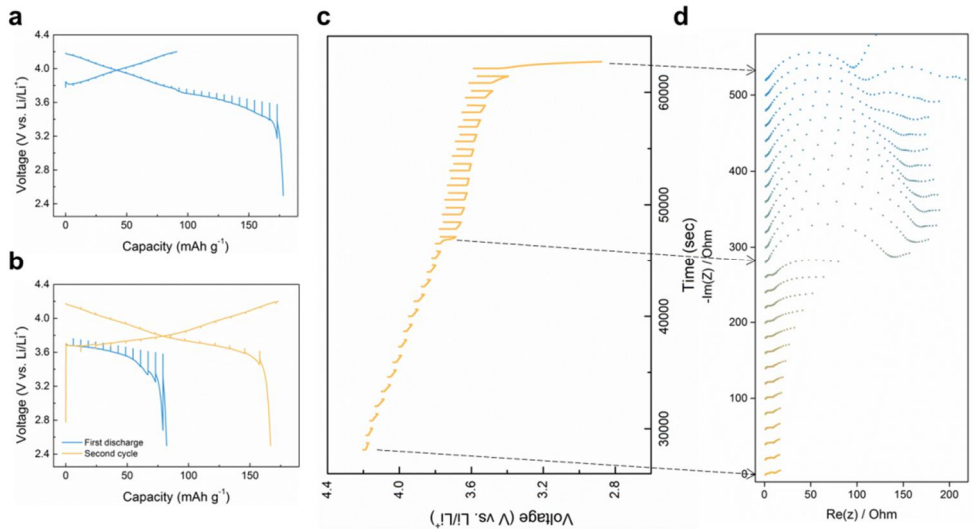

Figure 4.4. Increasing polarization at the voltage dropped region. a, GITT (charge and discharge) data after high temperature storage at SOC 50%. b, GITT (discharge – charge – discharge) data starting from the discharge reaction, indicating that the polarization appears only during the first discharge reaction. c,d, EIS data after high temperature storage. Additional impedance arises from the SOC 50% region.

4.3.2. Recovery of capacity retention

With the existent of memory effect, or the voltage drop from the additional polarization, the decrease in the capacity retention becomes inevitable after high temperature storage, which also reduces the energy density of the cell. Therefore, on the basis of our understandings on the memory effect, I try to enhance the capacity retention after high temperature storage through the recovery discharge process (Figure 4.5). The voltage profile of recovery process is shown in Figure 4.5a and b. After the storage at SOC 50%, the cell is cycled for 4 cycles at 25 °C (blue) and discharged at 60 °C until 100% capacity retention cut as a recovery cycle, plotted in green line. At the following cycles at 25 °C, it exhibits about 2.4 mAh g^{-1} enhanced capacity after recovery cycles. Figure 4.5c also shows that after the recovery cycle at fifth cycle, there is about 1.4% enhancement in capacity retention. When capacity retention data is normalized by capacity retention of undamaged cell (figure 4.5d), it clearly demonstrates that the normalized capacity retention, which was located at 95~96% before the recovery cycle, increases over 97% after the recovery cycle. It implies that the recovery cycle did work in improving capacity retention by sufficient lithium intercalation at high temperature environment. During the high temperature storage, the polarization is generated at the lithium vacant region, leading to the decrease in the capacity retention. Although this polarization can be removed by the lithium intercalation into the lithium vacant sites, the voltage cut cycling (2.5 – 4.2 V) cannot allow lithium intercalation up to 100% capacity retention level and some

amount of polarization remains in the active material, leading to the reduction in the capacity retention in the end. Therefore, it is necessary to further intercalate lithium in order to sufficiently remove the remaining polarization by discharging beyond the voltage cut range. For the sufficient lithium intercalation, the recovery discharge process is applied to remove remaining polarization coming from the memory effect and enhance capacity retention. The additional discharge is carried out at 60 °C until the amount of capacity exhibits 100% capacity retention. The capacity cut up to 100% capacity retention is intended to remove residual polarization through enough lithium intercalation, which cannot be realized from voltage cut discharge. Also, 60 °C is selected as the discharge temperature, because the same discharge process at room temperature induces a voltage plateau below 2 V region, demonstrating that lithium is intercalated not into the lithium octahedral site, but into the lithium tetrahedral site.[33-35] Since only the lithium intercalation into the vacant lithium octahedral sites can remove residual polarization, high temperature condition is necessary to minimize kinetic hindrance and stably induces lithium intercalation into the lithium octahedral sites. For a clearer confirmation on the recovery cycle, repetitive recovery cycles are applied every three cycles for longer stored cell (Figure 4.5e). At the first recovery cycle, there is a 2.8% enhancement in normalized capacity retention, and additional 0.3 and 0.6% enhancement at the following recovery cycles. The gradual and repetitive improvement in the capacity retention again indicates that the reduction in the capacity retention is affected by the memory effect and it can be partially recovered

from the sufficient lithium intercalation at high temperature. Moreover, it also implies that the generation of polarization would be related with the vacant sites during high temperature storage.

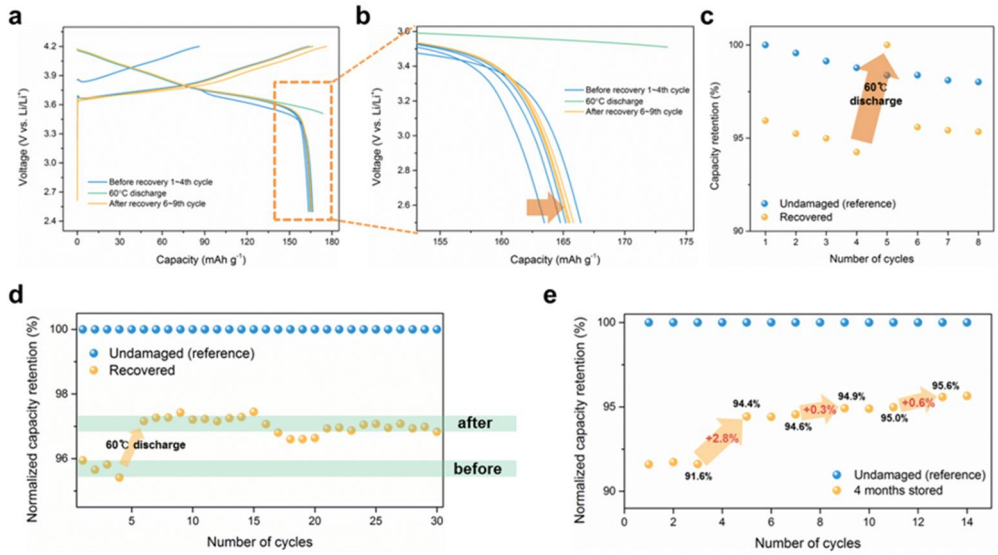

Figure 4.5. Capacity retention recovery process for the high temperature stored cell. a, Electrochemical profiles before recovery (blue), recover (green) and after recovery (orange) cycle. b, Enlarged profile of a. c, Capacity retention of recovery (orange) and undamaged (blue) cell. d, Capacity retention of recovery cell (orange) normalized by capacity retention of undamaged cell (blue). e, Normalized capacity retention of repeated (every 3 cycles) recovery cell.

4.3.3. Structural origin of thermal driven memory effect

In order to clarify the relation between voltage drop and vacant sites during the storage, I observed the lithium diffusion path directly through scanning transmission electron microscopy-high angle annular dark field (STEM-HAADF) images and discovered the generation of stacking faults in the active material after storage.[36, 37] It is well known how structural evolutions in layered materials closely related with electrochemical behaviors such as voltage decay, cycle degradation and voltage hysteresis.[23, 36, 38-40] Therefore, it is very likely that the proportional relation between the quantity of lithium vacancy during the storage and the capacity of voltage dropped region can be associated with the structural evolution at the lithium vacant region during the storage. Figure 4.6 shows STEM-HAADF images and its fast Fourier transform (FFT) image at the SOC 50% before the storage, where partial migration of TM from TM layer to lithium layer can be found in Figure 4.6b. After the high temperature storage, in addition to the increased TM migration, the formation of stacking fault can be clearly observed perpendicular to the ab plane (Figure 4.7a). As it is shown in Figure 4.7b and 4.7c, which are the magnified image of region 1 and 2 in Figure 4.7a, two different atomic arrangements exist in the close region. Figure 4.7b (region 1) indicates layered structure with TM migration, where peaks in the line profiling image stand for TMs in TM layer and lithium layer respectively. However, it shows much more complicated atomic arrangement in Figure 4.7c (region 2). The line profiling of the same range with Figure 4.7b shows the additional peak between TM and lithium

sites indicated by the red asterisks, which are identical to the oxygen sites of the layered structure. It is obviously not available for TM to be located in oxygen site. However, when one more layered unit cell is introduced as in Figure 4.7c, it matches perfectly with the atomic structure of the region 2. It directly implies that two different stackings exist in the structure as a stacking fault. The generation of the stacking fault is well demonstrated in Figure 4.7d, the magnified image of Figure 4.7a orange boxed region. From the red boxes in the left to the right in Figure 4.7d, it is possible to see that the new peak of TM between TM site and the lithium site becomes clear, and eventually being centered. It indicates that the stacking fault in Figure 4.7c has been gradually generated from the normal stacking sequence. The low magnified image in Figure 4.8 reveals that the stacking fault is spread as small domains (red region), where FFT images with sharp streaks also imply the generation of the stacking fault in the particle.[41, 42] While, there is no any signature on the stacking fault from neither HAADF nor FFT images before storage in Figure 4.6.

Further comparison between the regions with and without stacking fault is provided by electron energy loss spectroscopy (EELS) in Figure 4.9. Three regions with stacking faults are marked by orange box in figure 4.9a and each EELS data is compared with the EELS data from the region without stacking fault (blue box in figure 4.9a). As it is shown in Figure 4.9b-d on the Ni-L edge EELS data, all the regions with stacking fault are partially oxidized than the region without stacking fault.[43, 44] It indicates that the region with stacking fault is locally oxidized and

contains less lithium, or more delithiated. According to our discovery on the thermal driven memory effect, lithium intercalation into the delithiated region during the storage induced additional polarization and attributed to the memory effect. Therefore, the region with stacking fault, which is the delithiated region during the storage, should be related with the memory effect. There have been previous works on the observation of stacking faults in the electrode materials and their effects on the electrochemical performances.[36, 45-50] Boulineau et al. found the localized stacking fault in the Li_2MnO_3, which was suggested that the gliding of slabs induced the formation of localized stacking fault.[51] Moreover, it is reported that stacking faults in the electrode materials, which makes the phase transformation of the material easier, or the gliding of TMO_2 slabs in the layered materials are detrimental to the battery cycle properties.[36, 45-48] Likewise, in this study, the polarization appears to be generated when lithium passes the boundary of stacking fault region, inducing the memory effect. Therefore, the stacking fault, which is formed at the delithiated region of the active materials during the high temperature storage, is the main contributor for the memory effect.

The inhomogeneous distribution on the oxidation state of nickel after storage is also observed from the soft X-ray ptychography data.[52-54] Using ptychography, it is possible to obtain the distribution of nickel oxidation state up to 5 nm resolution in the particle, as shown in Figure 4.7e-g, where red and blue colors denote relatively oxidized and reduced state of nickel acquired from Ni L_3 absorption edge respectively. Ptychography data on the particles before storage at

SOC 50% show that the oxidation state of nickel is almost same from all over the particle (Figure 4.7e, Figure 4.10a, b), which also indicates that Li is homogeneously distributed in the particle after SOC setting. However, the oxidation state of nickel becomes less homogeneous after storage at SOC 50%, which could be related with the formation of stacking faulted region during the storage as shown in EELS data (Figure 4.7f and 4.10c-e). When the line profiles of nickel oxidation state are compared along the A-B line from each image, the line profile from the stored sample also shows larger deviation (Figure 4.7g), implying the less homogeneous environment after storage. In addition to the EELS data, ptychography data demonstrates that the nickel oxidation state in the particle becomes inhomogeneous during the high temperature storage and considering the close relationship between lithium and the oxidation state of nickel, it is highly likely that the local environment around lithium could also be changed during the storage.

The variation in the lithium local environments after storage is observed using ^{7}Li NMR spectroscopy. With the sensitiveness on the paramagnetic metal, NMR is an efficient tool to observe the local environmental change around lithium.[44, 55-58] Shown in Figure 4.7h, two different peaks can be found as marked in A and B after storage at SOC 50%. While only one main peak A exists at 380 ppm before storage, it is possible to find two peaks after storage; higher chemical shift peak A and appearance of lower chemical shift peak B. Considering the high amount of nickel and its role as a redox center, most of peak shift is attributed to

the changes in the oxidation of nickel ion and only paramagnetic $Ni^{2+/3+}$ induces large peak shift, while diamagnetic Ni^{4+} does not induce any frequency shift.[44] Considering the SOC 50% state and the oxidation state of nickel, large peak shift in peak A could be attributed to the paramagnetic Ni^{3+}. After storage, however, peak A shifts toward higher frequency, which indicates that lithium is surrounded by nickel in a partially reduced state compared to the nickel oxidation state before storage. In addition, new peak appearance at peak B with low peak shift is attributed to the lithium surrounded dominantly by diamagnetic Ni^{4+}, which implies that oxidized nickel encircles some of lithium. Therefore, separated NMR peak after storage demonstrates that some of nickel is locally reduced and oxidized during the storage and it is consistent with the STEM-EELS and ptychography data. Observations of more oxidized and stacking faulted region in STEM, larger deviation of oxidation state in ptychography data and peak separation in NMR all show that partially delithiated region is agglomerated with the formation of stacking fault, which induces memory effect after high temperature storage.

The driving force for the formation of delithiated region is further explored from the strain analyses. High temperature storage of the cell leads to the decrease in the strain of the particle, obtained from high resolution powder diffraction (HRPD) data using Williamson-Hall plot for electrodes with pristine state, SOC 50% before storage and after storage (Figure 4.11).[59-61] In case of the bare electrode, strain of the particle stays in 0.187%, while the SOC setting at SOC 50% attributes to the considerable increase in the strain to 0.334%. However, the

decrease in the strain was found from the 4-weeks stored cell to 0.282%, which coincides with about 35% of recovery from the elevated strain after SOC setting. It should be noted that lithation/delithiation attribute to the increase in the strain of the particle, affected by the formation of vacancies, TM migration and lattice parameter differences.[60-65] TM migration and changes in lattice parameter occur in the delithiated region locally, hence, the local variation of lithium concentration generates strain of the particle.[60, 66-68] Therefore, in case of NCM811 in this study, while electrochemical reactions for SOC setting contribute to the increase in the strain, high temperature storage of the cell for the sufficient period of time result in the rearrangement between lithium and TM, leading to the reduction in the strain.

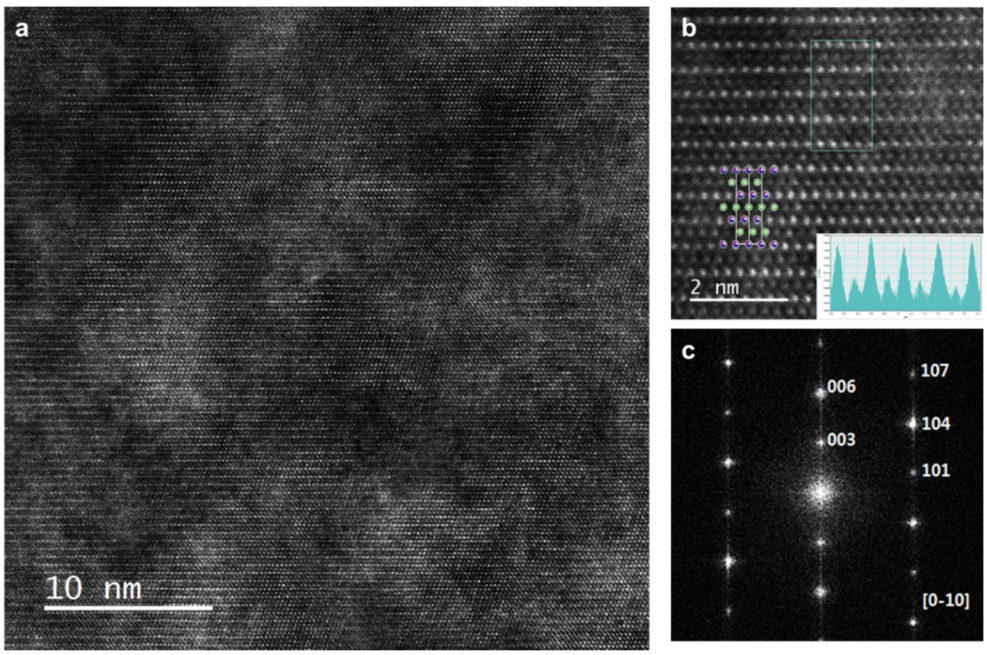

Figure 4.6. a, STEM-HAADF image before storage at SOC 50%. b, Enlarged image of a. Inset shows the intensity line profile of the box in b. c, FFT image of a.

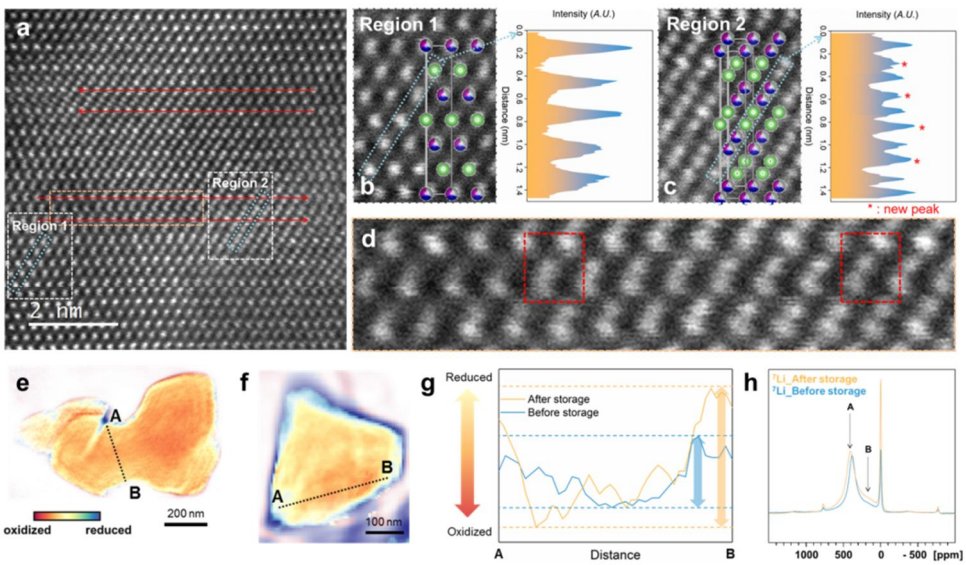

Figure 4.7. Structural evolution and local environment variation after high temperature storage. a, STEM-HAADF image of stored cell at SOC 50% along [100] direction. b, Enlarged image of A region in a and its intensity line profile. c, Enlarged image of B region in a and its intensity line profile. d, Enlarged image of orange box region in a, demonstrating the formation of stacking faulted domain. e,f, Ptychography image before storage (e) and after storage (f) obtained from Ni L_3 absorption edge. The red and blue colors denote relatively oxidized and reduced oxidation state of Ni. g, Line profile of nickel oxidation state along AB line from e and f. h, ^{7}Li NMR spectra of the NCM811 samples at SOC 50% before storage (blue) and after storage (orange).

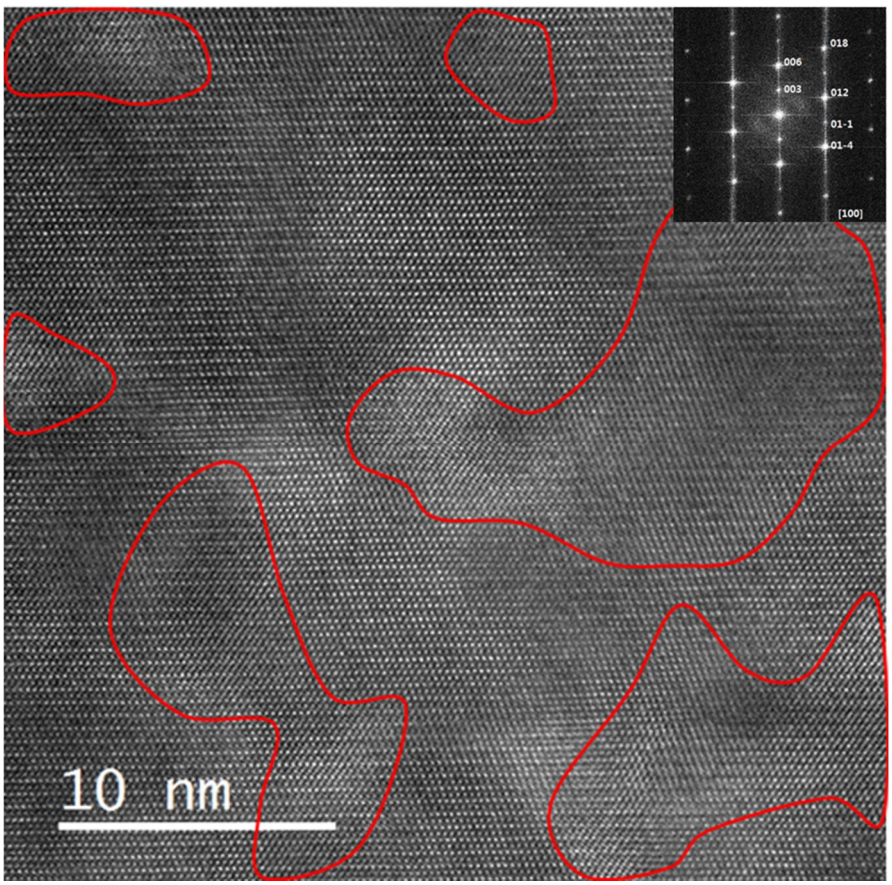

Figure 4.8. STEM-HAADF image after high temperature storage. Inset shows FFT image with clear streaks. Red region denotes stacking faulted region.

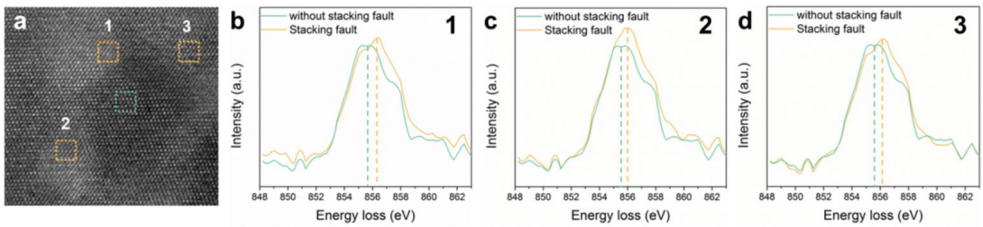

Figure 4.9. a, STEM-HAADF image of stored cell for EELS observation. b-d, Comparison of the Ni L3-edge EELS spectra between stacking faulted region (orange) and non-faulted region (blue) obtained from a.

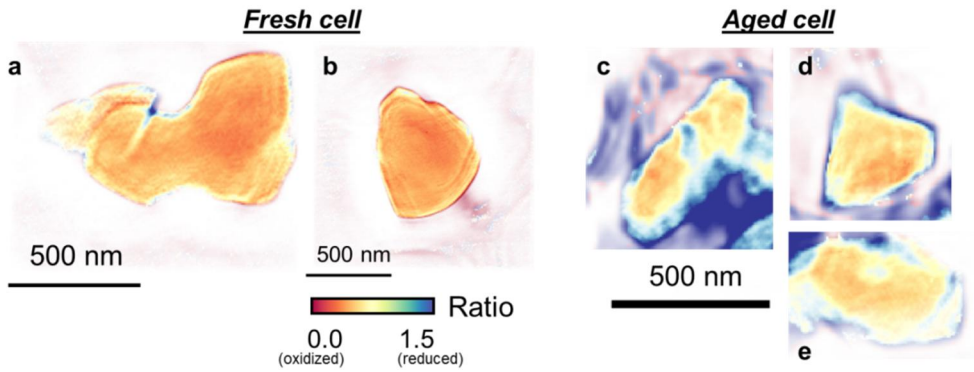

Figure 4.10. Ptychography image before storage (a,b) and after storage (c-e).

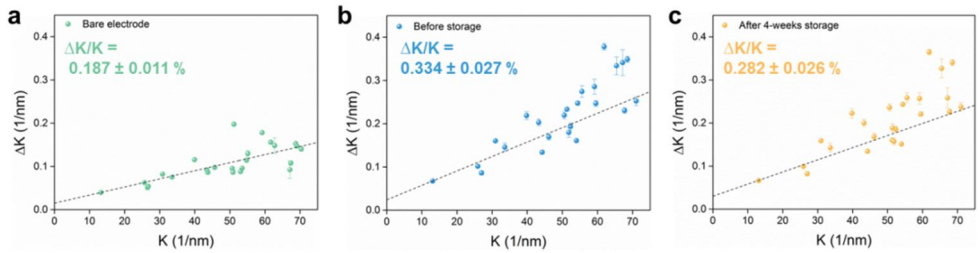

Figure 4.11. Williamson-Hall plot for bare electrode (a), before storage at SOC 50% (b) and after 4-weeks storage at SOC 50% (c)

4.3.4 Model for thermal driven memory effect

On the basis of our experimental results, I propose the model for this phenomenon on the thermal driven memory effect. The schematic diagram of the atomic arrangement before and after high temperature storage is shown in Figure 4.12, respectively. After setting SOC 50% and before storage, lithium is homogeneously delithiated, hence, local environment of lithium and oxidation state of nickel are all in the same state (Figure 4.7). At this state, the strain is formed due to the lattice mismatches between lithiated/delithiated region, resulting in the increase of particle strain.[60-65] On the other hand, high temperature storage causes the formation of locally delithiated domain, leading to the non-uniform local environment of lithium and distribution of nickel oxidation state (Figure 4.7b). The agglomeration, or the locally delithiated domain formation, reduces the lithiated/delithiated interface area, which attributes to the decrease in the strain of particle, just as Ostwald ripening occurs to reduce interfacial area of particles.[69, 70] Once the delithiated domain is formed, the lithium intercalation into the delithiated domain contributes to the additional polarization, which is triggered by two factors; stacking fault and TM migration. Since the lithium intercalation into the delithiated domain passes through the stacking fault boundary, the additional polarization can be generated at the boundary region.[36, 48, 71] In addition, as delithiation accompanies with TM migration, more migrated TM would exist in the delithiated domain, which will act as lithium diffusion barrier and increase polarization.[46, 72-74] Therefore, the delithiated domain is formed in proportion to the amount of lithium

that is delithiated during high temperature storage, and thus, the capacity in which the voltage drop is generated is also increased in proportion to the SOC.

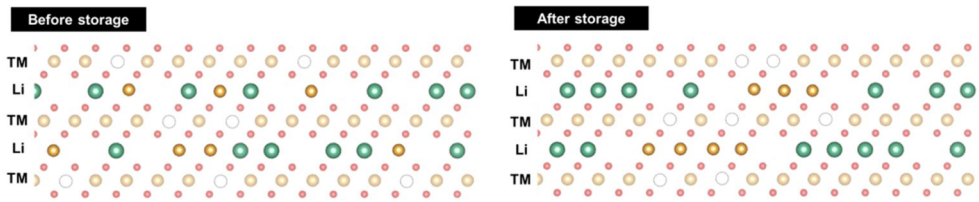

Figure 4.12. Schematic diagram of the model for thermal driven memory effect. Before storage at SOC 50%, lithium (green circle) is homogeneously delithiated with TM (yellow circle) migration into the lithium layers. Strain is generated between every lithiated and delithiated interfaces. After storage, locally delithiated domain is formed to reduce strain of the particles.

4.4. Concluding Remarks

In summary, I have discovered the thermal driven memory effect of NCM811 and suggested the mechanism on the phenomenon. I investigate the effect of high temperature storage at various SOCs, which generates additional polarization proportional to the delithiated lithium during storage. During the high temperature storage, the delithiated domain is formed through the agglomeration between delithiated regions to minimize the strain produced from the lithiated/delithiated boundaries, resulting in the inhomogeneous local environment of lithium and nickel oxidation state in the particle by presenting locally higher nickel oxidation state with stacking fault. As a result, I demonstrate that the additional polarization is generated since the lithium intercalation into the delithiated domain requires reversible TM migration and passing through the stacking fault boundary, leading to the SOC dependent polarization. Our results suggest that though LIB can avoid the memory effect from repeatable charge/discharge as in the case for Ni-Cd battery, certain conditions such as high temperature storage would induce memory effect in LIB beyond general beliefs. Also, it also suggests that the particle might become inhomogeneous at higher temperatures due to the strain effect, in contrast to the common belief that increasing temperature contributes to the increasing entropy and making particle more homogeneous. Thus, more careful consideration and investigation on the effect of heating and storage should be achieved for electrode materials in LIB.

4.5. References

[1] M. Armand, J. M. Tarascon, *Nature* **2008**, 451, 652.

[2] B. Dunn, H. Kamath, J.-M. Tarascon, *Science* **2011**, 334, 928.

[3] M. M. Thackeray, C. Wolverton, E. D. Isaacs, *Energy Environ. Sci.* **2012**, 5, 7854.

[4] L. Lu, X. Han, J. Li, J. Hua, M. Ouyang, *J. Power Sources* **2013**, 226, 272.

[5] K. Tae-Hee, P. Jeong-Seok, C. S. Kyun, C. Seungdon, R. J. Heon, S. Hyun-Kon, *Adv. Energy Mater.* **2012**, 2, 860.

[6] A. Barré, B. Deguilhem, S. Grolleau, M. Gérard, F. Suard, D. Riu, *J. Power Sources* **2013**, 241, 680.

[7] J. Vetter, P. Novák, M. R. Wagner, C. Veit, K. C. Möller, J. O. Besenhard, M. Winter, M. Wohlfahrt-Mehrens, C. Vogler, A. Hammouche, *J. Power Sources* **2005**, 147, 269.

[8] G. Amatucci, A. Du Pasquier, A. Blyr, T. Zheng, J. M. Tarascon, *Electrochim. Acta* **1999**, 45, 255.

[9] Y. Matsuo, R. Kostecki, F. McLarnon, *J. Electrochem. Soc.* **2001**, 148, A687.

[10] M. Guilmard, L. Croguennec, D. Denux, C. Delmas, *Chem. Mater.* **2003**, 15, 4476.

[11] M. Wohlfahrt-Mehrens, C. Vogler, J. Garche, *J. Power Sources* **2004**, 127, 58.

[12] M. Broussely, P. Biensan, F. Bonhomme, P. Blanchard, S. Herreyre, K.

Nechev, R. J. Staniewicz, *J. Power Sources* **2005**, 146, 90.

[13] N. Kyung-Wan, B. Seong-Min, H. Enyuan, Y. Xiqian, Z. Youngning, W. Xiaojian, W. Lijun, Z. Yimei, C. Kyung-Yoon, Y. Xiao-Qing, *Adv. Funct. Mater.* **2013**, 23, 1047.

[14] Q. Li, G. Li, C. Fu, D. Luo, J. Fan, J. Zheng, D. Xie, L. Li, *Electrochim. Acta* **2015**, 154, 249.

[15] L. Wen, O. Pilgun, L. Xien, L. Min-Joon, C. Woongrae, C. Sujong, K. Youngsik, C. Jaephil, *Angew. Chem. Int. Ed.* **2015**, 54, 4440.

[16] F. Schipper, E. M. Erickson, C. Erk, J.-Y. Shin, F. F. Chesneau, D. Aurbach, *J. Electrochem. Soc.* **2017**, 164, A6220.

[17] J. Hong, H. Gwon, S.-K. Jung, K. Ku, K. Kang, *J. Electrochem. Soc.* **2015**, 162, A2447.

[18] J. W. Choi, D. Aurbach, *Nat. Rev. Mater.* **2016**, 1, 16013.

[19] H.-D. Lim, B. Lee, Y. Bae, H. Park, Y. Ko, H. Kim, J. Kim, K. Kang, *Chem. Soc. Rev.* **2017**, 46, 2873.

[20] M. S. Whittingham, *Chem. Rev.* **2004**, 104, 4271.

[21] V. Etacheri, R. Marom, R. Elazari, G. Salitra, D. Aurbach, *Energy Environ. Sci.* **2011**, 4, 3243.

[22] H.-J. Noh, S. Youn, C. S. Yoon, Y.-K. Sun, *J. Power Sources* **2013**, 233, 121.

[23] J. Sung-Kyun, G. Hyeokjo, H. Jihyun, P. Kyu-Young, S. Dong-Hwa, K. Haegyeom, H. Jangsuk, Y. Wooyoung, K. Kisuk, *Adv. Energy Mater.* **2014**, 4,

1300787.

[24] A. O. Kondrakov, A. Schmidt, J. Xu, H. Geßwein, R. Mönig, P. Hartmann, H. Sommer, T. Brezesinski, J. Janek, *J. Phys. Chem. C* **2017**, 121, 3286.

[25] J.-M. Lim, T. Hwang, D. Kim, M.-S. Park, K. Cho, M. Cho, *Sci. Rep.* **2017**, 7, 39669.

[26] Y. Cho, P. Oh, J. Cho, *Nano Lett.* **2013**, 13, 1145.

[27] M. D. J., P. Christian, W. J. G., A. D. P., B. Javier, *Adv. Energy Mater.* **2013**, 3, 1098.

[28] T. Sasaki, Y. Ukyo, P. Novák, *Nat. Mater.* **2013**, 12, 569.

[29] K.-Y. Park, J. Hong, W.-M. Seong, J.-J. Kim, K. Ku, B. Lee, K. Kang, *Energy Environ. Sci.* **2017**, 10, 2352.

[30] M. Hess, T. Sasaki, C. Villevieille, P. Novák, *Nat. Commun.* **2015**, 6, 8169.

[31] W. Zhang, H.-C. Yu, L. Wu, H. Liu, A. Abdellahi, B. Qiu, J. Bai, B. Orvananos, F. C. Strobridge, X. Zhou, Z. Liu, G. Ceder, Y. Zhu, K. Thornton, C. P. Grey, F. Wang, *Science Advances* **2018**, 4.

[32] J. Lim, Y. Li, D. H. Alsem, H. So, S. C. Lee, P. Bai, D. A. Cogswell, X. Liu, N. Jin, Y.-s. Yu, N. J. Salmon, D. A. Shapiro, M. Z. Bazant, T. Tyliszczak, W. C. Chueh, *Science* **2016**, 353, 566.

[33] C. S. Johnson, J.-S. Kim, A. Jeremy Kropf, A. J. Kahaian, J. T. Vaughey, M. M. Thackeray, *Electrochem. Commun.* **2002**, 4, 492.

[34] R. Benedek, J. Vaughey, M. M. Thackeray, *Chem. Mater.* **2006**, 18, 1296.

[35] S.-H. Kang, S.-H. Park, C. S. Johnson, K. Amine, *J. Electrochem. Soc.* **2007**, 154, A268.

[36] E. McCalla, A. M. Abakumov, M. Saubanère, D. Foix, E. J. Berg, G. Rousse, M.-L. Doublet, D. Gonbeau, P. Novák, G. Van Tendeloo, R. Dominko, J.-M. Tarascon, *Science* **2015**, 350, 1516.

[37] W. Yongqing, Y. Zhenzhong, Q. Yumin, G. Lin, Z. Haoshen, *Adv. Mater. (Weinheim, Ger.)* **2015**, 27, 3915.

[38] M. Sathiya, A. M. Abakumov, D. Foix, G. Rousse, K. Ramesha, M. Saubanère, M. L. Doublet, H. Vezin, C. P. Laisa, A. S. Prakash, D. Gonbeau, G. VanTendeloo, J. M. Tarascon, *Nat. Mater.* **2015**, 14, 230.

[39] K. Kyojin, H. Jihyun, K. Hyungsub, P. Hyeokjun, S. W. Mo, J. Sung-Kyun, Y. Gabin, P. Kyu-Young, K. Haegyeom, K. Kisuk, *Adv. Energy Mater.*, 0, 1800606.

[40] F. Dogan, B. R. Long, J. R. Croy, K. G. Gallagher, H. Iddir, J. T. Russell, M. Balasubramanian, B. Key, *J. Am. Chem. Soc.* **2015**, 137, 2328.

[41] T. Besara, D. A. Rhodes, K. W. Chen, S. Das, Q. R. Zhang, J. Sun, B. Zeng, Y. Xin, L. Balicas, R. E. Baumbach, E. Manousakis, D. J. Singh, T. Siegrist, *Phys. Rev. B* **2016**, 93, 245152.

[42] L. Kabalah-Amitai, B. Mayzel, Y. Kauffmann, A. N. Fitch, L. Bloch, P. U. P. A. Gilbert, B. Pokroy, *Science* **2013**, 340, 454.

[43] F. Lin, I. M. Markus, D. Nordlund, T.-C. Weng, M. D. Asta, H. L. Xin, M. M. Doeff, *Nat. Commun.* **2014**, 5, 3529.

[44] H. Liu, M. Bugnet, M. Z. Tessaro, K. J. Harris, M. J. R. Dunham, M. Jiang, G. R. Goward, G. A. Botton, *Phys. Chem. Chem. Phys.* **2016**, 18, 29064.

[45] L.-X. Yuan, Z.-H. Wang, W.-X. Zhang, X.-L. Hu, J.-T. Chen, Y.-H. Huang, J. B. Goodenough, *Energy Environ. Sci.* **2011**, 4, 269.

[46] H. Yu, Y.-G. So, A. Kuwabara, E. Tochigi, N. Shibata, T. Kudo, H. Zhou, Y. Ikuhara, *Nano Lett.* **2016**, 16, 2907.

[47] J. B. Cook, C. Kim, L. Xu, J. Cabana, *J. Electrochem. Soc.* **2013**, 160, A46.

[48] J.-M. Kim, H.-T. Chung, *J. Power Sources* **2003**, 115, 125.

[49] A. Boulineau, L. Croguennec, C. Delmas, F. Weill, *Solid State Ionics* **2010**, 180, 1652.

[50] K. A. Jarvis, Z. Deng, L. F. Allard, A. Manthiram, P. J. Ferreira, *Chem. Mater.* **2011**, 23, 3614.

[51] A. Boulineau, L. Croguennec, C. Delmas, F. Weill, *Chem. Mater.* **2009**, 21, 4216.

[52] D. A. Shapiro, Y.-S. Yu, T. Tyliszczak, J. Cabana, R. Celestre, W. Chao, K. Kaznatcheev, A. L. D. Kilcoyne, F. Maia, S. Marchesini, Y. S. Meng, T. Warwick, L. L. Yang, H. A. Padmore, *Nat. Photonics* **2014**, 8, 765.

[53] Y.-S. Yu, M. Farmand, C. Kim, Y. Liu, C. P. Grey, F. C. Strobridge, T. Tyliszczak, R. Celestre, P. Denes, J. Joseph, H. Krishnan, F. R. N. C. Maia, A. L. D. Kilcoyne, S. Marchesini, T. P. C. Leite, T. Warwick, H. Padmore, J. Cabana, D. A. Shapiro, *Nat. Commun.* **2018**, 9, 921.

[54] Y.-S. Yu, C. Kim, D. A. Shapiro, M. Farmand, D. Qian, T. Tyliszczak, A. L. D. Kilcoyne, R. Celestre, S. Marchesini, J. Joseph, P. Denes, T. Warwick, F. C. Strobridge, C. P. Grey, H. Padmore, Y. S. Meng, R. Kostecki, J. Cabana, *Nano Lett.* **2015**, 15, 4282.

[55] W.-S. Yoon, S. Iannopollo, C. P. Grey, D. Carlier, J. Gorman, J. Reed, G. Ceder, *Electrochem. Solid-State Lett.* **2004**, 7, A167.

[56] O. Pecher, J. Carretero-González, K. J. Griffith, C. P. Grey, *Chem. Mater.* **2017**, 29, 213.

[57] C. P. Grey, N. Dupré, *Chem. Rev.* **2004**, 104, 4493.

[58] D. Zeng, J. Cabana, J. Bréger, W.-S. Yoon, C. P. Grey, *Chem. Mater.* **2007**, 19, 6277.

[59] G. K. Williamson, W. H. Hall, *Acta Metallurgica* **1953**, 1, 22.

[60] C. R. Fell, D. Qian, K. J. Carroll, M. Chi, J. L. Jones, Y. S. Meng, *Chem. Mater.* **2013**, 25, 1621.

[61] G. W. E., L. Yiyang, A. Sungjin, L. Jongwoo, L. Yijin, W. A. M., G. C. Balaji, M. D. N., D. Ryan, W. J. Nelson, P. Jin-Hwan, D. Seok-Kwang, C. W. C., *Adv. Mater. (Weinheim, Ger.)* **2016**, 28, 6631.

[62] M. Gu, I. Belharouak, J. Zheng, H. Wu, J. Xiao, A. Genc, K. Amine, S. Thevuthasan, D. R. Baer, J.-G. Zhang, N. D. Browning, J. Liu, C. Wang, *ACS Nano* **2012**, 7, 760.

[63] H. Tavassol, E. M. C. Jones, N. R. Sottos, A. A. Gewirth, *Nat. Mater.* **2016**, 15, 1182.

[64] A. Clémençon, A. T. Appapillai, S. Kumar, Y. Shao-Horn, *Electrochim. Acta* **2007**, 52, 4572.

[65] H. Wang, Y.-I. Jang, B. Huang, D. R. Sadoway, Y.-M. Chiang, *J. Power Sources* **1999**, 81-82, 594.

[66] W. E. Gent, K. Lim, Y. Liang, Q. Li, T. Barnes, S.-J. Ahn, K. H. Stone, M. McIntire, J. Hong, J. H. Song, Y. Li, A. Mehta, S. Ermon, T. Tyliszczak, D. Kilcoyne, D. Vine, J.-H. Park, S.-K. Doo, M. F. Toney, W. Yang, D. Prendergast, W. C. Chueh, *Nat. Commun.* **2017**, 8, 2091.

[67] J. Reed, G. Ceder, *Chem. Rev.* **2004**, 104, 4513.

[68] I. Takahashi, K. Fukuda, T. Kawaguchi, H. Komatsu, M. Oishi, H. Murayama, M. Hatano, T. Terai, H. Arai, Y. Uchimoto, E. Matsubara, *J. Phys. Chem. C* **2016**, 120, 27109.

[69] P. W. Voorhees, *Journal of Statistical Physics* **1985**, 38, 231.

[70] G. Madras, B. J. McCoy, *Chem. Eng. Sci.* **2004**, 59, 2753.

[71] B. Lung-Hao Hu, F.-Y. Wu, C.-T. Lin, A. N. Khlobystov, L.-J. Li, *Nat. Commun.* **2013**, 4, 1687.

[72] H. Yu, Y. Qian, M. Otani, D. Tang, S. Guo, Y. Zhu, H. Zhou, *Energy Environ. Sci.* **2014**, 7, 1068.

[73] K. Kang, Y. S. Meng, J. Bréger, C. P. Grey, G. Ceder, *Science* **2006**, 311, 977.

[74] J. Lee, A. Urban, X. Li, D. Su, G. Hautier, G. Ceder, *Science* **2014**, 343, 519.

Chapter 5. Conclusion

The structure of layered materials for LIB was thought to be a rigid model from the classical viewpoints, where lithium ion is the only mobile ion, which limits the understandings on the electrochemical properties of layered materials. In this research, by studying structural evolutions of layered materials that appear under the various electrochemical reactions, new models for the reaction mechanisms and design strategies for the advanced layered materials are suggested. In chapter 2, I show that the activation of Mn redox with electrochemical cycles leads to the structural evolution, attributing to the voltage decay, and propose a new strategy to suppress the voltage decay in lithium-rich layered oxide electrodes by introducing a Ni^{3+} redox buffer that can subdue the redox activity of manganese and its migration in the layered structure. The suppression of the voltage decay is correlated to a decrease in the Mn^{3+} content resulting from the Mn^{4+} reduction during the discharge reaction, which could be systematically tailored by the presence of the Ni^{3+} redox buffer, enabling extended nickel redox activity from Ni^{3+}/Ni^{4+} to Ni^{2+}/Ni^{4+} after the partial loss of the oxygen anionic redox. It suggests that to suppress the voltage decay of layered lithium-rich transition metal oxides, it is critical to deal with the cation migration that induces the formation of the disordered spinel-like domain. In addition, tailoring of the oxidation states of nickel and manganese not only in the pristine states but also during electrochemical cycling can offer an effective way to prevent the voltage decay in lithium-rich layered oxides without the use of 4d or 5d elements.

In chapter 3, I highlight that intercalation and de-intercalation kinetics in layered lithium TM oxides electrodes could be inherently non-equivalent, exhibiting respectively distinct lithium diffusion mechanisms, and propose a new lithium diffusion and intercalation model. The lithium diffusion is much more sluggish during the lithiation than the de-lithiation, which could not be elucidated based on the classical lithium diffusion model within a rigid layered framework. From the series of electrochemical and structural analyses, I illustrated that it originates from the asymmetric TM migrations during charge and discharge, which offers non-equivalent local environments for lithium diffusion. Due to the randomness of TM hoppings and the difficulty of TM in finding the original vacancy in TM layer to migrate back, the presence of TM is far extended in the lithium layer, redundantly retarding the lithium diffusion particularly during lithiation process. The extended and distracted migration of TMs in the lithium layer makes the reversible TM migration toward TM layer get sluggish. The new lithium diffusion model explicates the non-equivalent intercalation and de-intercalation kinetics in the layered structure and reveals the importance of considering the correlative motion between lithium and TM in the structure in understanding this class of materials.

In chapter 4, I discover the thermal driven memory effect of NCM811 and suggested the mechanism on the phenomenon. I investigate the effect of high temperature storage at various SOCs, which generates additional polarization proportional to the delithiated lithium during storage. During the high temperature storage, the delithiated domain is formed through the agglomeration between

delithiated regions to minimize the strain produced from the lithiated/delithiated boundaries, resulting in the inhomogeneous local environment of lithium and nickel oxidation state in the particle by presenting locally higher nickel oxidation state with stacking fault. As a result, I demonstrate that the additional polarization is generated since the lithium intercalation into the delithiated domain requires reversible TM migration and passing through the stacking fault boundary, leading to the SOC dependent polarization. Also, it implies that the particle might become inhomogeneous at higher temperatures due to the strain effect, in contrast to the common belief that increasing temperature contributes to the increasing entropy and making particle more homogeneous. Thus, more careful consideration and investigation on the effect of heating and storage should be achieved for electrode materials in LIB.

In the thesis, I investigated the relations between structural evolutions and electrochemical performances of layered materials. At the moment that layered materials with advanced electrochemical properties are required, I believe that this thesis on the new diffusion model and reaction behavior for layered materials will provide clearer guidance in the design and understanding of layered materials. I hope lithium-rich layered oxides and high nickel layered materials could be practically used soon based on the understandings of the thesis.

Chapter 6. Abstract in Korean

국 문 초 록

고성능의 휴대 기기들과 전기자동차의 개발은 더 높은 에너지 밀도를 갖는 리튬 이온 배터리에 대한 수요를 증가시키고 있다. 일반적으로 양극의 단위 무게당 용량이 음극보다 작기 때문에, 보통 두 배 이상의 양극이 실제 배터리 안에 포함된다. 따라서 높은 단위당 용량을 갖는 양극 소재를 개발하는 것은 리튬 이온 배터리의 에너지 밀도를 높이는 하나의 주요한 전략으로 받아들여지고 있다. 현재 상업적으로 가장 많이 사용되고 있는 양극 소재는 $LiCoO_2$나 $LiNi_xCo_yMn_zO_2$ (NCM)와 같은 층상구조 물질로, 대체로 높은 에너지 밀도와 이차원의 확산 경로를 가지고 있다. 그러나 고에너지밀도의 리튬 이온 배터리에 대한 급격한 수요를 충족시키기 위해서는 현재 사용되고 있는 양극 보다 더 높은 용량을 갖는 양극에 대한 개발이 매우 중요하다.

층상구조 물질의 전기화학 특성에 영향을 주는 다양한 요소 중, 층상구조 물질의 구조는 가장 밀접하게 관련되어 있는 것으로 알려져 있다. 기존에 이해하고 있는 바에 따르면, 리튬의 삽입 및 탈리는 층상구조의 틀을 유지한 채 발생되는 것으로 알려져 있었다. 따라서 비록 리튬층에 존재하는 전이금속이 리튬 층의 공간을 줄이고 전이금속과의 반발력을 증가시켜 리튬 확산을 방해하는 작용을 하더라도, 리튬 층의 전이금속은 비유동적인 것으로 이해하고 있었다. 이와 같이 고정된 구조 모델에서는, 리튬이 삽입되는 구조 안에서 움직일 수 있는 유일한 이온이기 때문에, 초기 합성시의 상 자체가 전기화학 특성을 결정짓는 가장 중요한 요소로 받아들여졌다. 그러나 최근의 보고들에서는 전기화학 반응이 진행되는 동안 전이금속의 이동이나 산소의 발생 등 다양한 구조 변

화가 일어난다는 것을 밝히고 있다. 따라서, 전기화학 반응 중 발생되는 층상구조 물질의 구조변화에 대해 이해하고, 이러한 구조변화가 전기화학 특성에 어떠한 영향을 미치는지 이해하는 것은 매우 중요하다.

본 논문에서는, 층상구조 물질이 여러 번의 충방전부터 간단한 저장 등과 같은 다양한 전기화학 반응의 조건 하에서 발생되는 구조변화와 이러한 구조변화가 전기화학 반응에 미치는 영향에 대해 밝힌다. 리튬 과량 층상구조 산화물에서 여러 번의 충방전이 진행됨에 따라 발생되는 전압 강하는 Mn의 산화환원 반응 참여로 인한 층상구조에서 스피넬 상으로의 구조 변화에 의한 것이다. 따라서 전압 강하 문제는 간단한 Ni 산화환원 완충제를 도입하여 해결할 수 있게 된다. 게다가 리튬 과량 층상구조 산화물에서 단 한번의 충방전에도 리튬의 확산에 영향을 주는 비대칭적인 전이금속의 이동이 구조 내에서 발생되기 때문에, 이를 바탕으로 전이금속의 이동을 함께 고려한 새로운 리튬 확산 모델을 제안한다. 또한, 고니켈 NCM의 구조 변화가 전기화학 반응이 일어나지 않는 고온 저장 상태에서도 발생되는 것을 관찰하고, 결과적으로 이러한 구조 변화가 전극 물질의 매우 독특한 메모리 효과를 유발하는 것을 밝힌다. 구조 변화와 전기화학 특성간의 밀접한 관계에 대한 발견은 다양한 전기화학 조건에서 발생되는 구조 변화에 대한 이해가 리튬 이온 배터리의 층상구조 물질의 전기화학 특성을 개선 시키기 위하여 매우 중요한 요소임을 암시한다.

주요어: 배터리, 양극, 층상구조 산화물, 리튬 과량 물질, 리튬 이차 전지.

학 번: 2013-20580